THE UNIVERSITY OF QUEENSLAND

AUSTRALIA

SKIN CANCER DETECTION USING LASER IMAGING

Alireza Mowla

B.Sc.(Electrical Engineering),M.Sc.(Electrical Engineering)

A thesis submitted for the degree of Doctor of Philosophy at
The University of Queensland in 2016

SCHOOL OF INFORMATION TECHNOLOGY AND ELECTRICAL ENGINEERING

Abstract

Endeavors to develop a non-invasive and reliable device to detect different types of skin cancer in its early stages have been undertaken over the past few years. Although some advances have been made towards such developments, there remains great scope for the development of a non-expensive, compact, reliable, safe, easy to use, fast, sensitive, and non-invasive device. This project will apply the innovative laser feedback interferometry (LFI) technique to skin cancer detection via laser imaging using near-infrared vertical cavity surface emitting lasers (VCSELs). In this project, the science behind light–tissue interactions has been explored and skin imaging modalities have been elaborately studied. As a result, LFI has been exploited in various configurations to image different modalities such as Doppler flowmetry and confocal reflectance. In addition to single modality imaging, dual-modality imaging has also been proposed and conducted experimentally, to image Doppler flowmetry and confocal reflectance at the same time, using an integrated LFI system. It is shown that dual-modality imaging can yield images with higher contrast which provide more information about morphological and functional characteristics of a target under test.

In addition to two-dimensional LFI imaging, three-dimensional imaging systems have also been studied and employed in the laboratory. A tomographic image identifies tissue volume with altered optical properties due to cancerous or other malignant tissue processes. We applied the three-dimensional imaging system to different types of keratinocyte skin cancer phantoms and results show high level of sensitivity in providing tomographic images. Using high numerical aperture lenses, making images at resolutions down to micrometer scales is possible, which is promising for microscopy of biological structures.

Furthermore, parallel LFI imaging using an array of 24 VCSELs was also studied theoretically and experimentally as a part of this work. A VCSEL array was used in a parallel read-out LFI imaging system to develop a fast and high resolution device, which eliminates the need to scan mechanically in one dimension.

Investigating the complex interactions of the laser beam and tissue requires a powerful and robust simulation technique. Monte Carlo was used as a simulation technique to model the light–tissue interactions occurring in the optical systems in this work. Firstly, we tested and validated the Monte Carlo main engine which was developed in the group, by studying morphological aspects of the simulated and experimental signals in a laser Doppler velocimetry system, and deep insight into the nature of the LFI Doppler spectrum and further conclusions were drawn. Secondly, the Monte Carlo engine was used in

modeling and analyzing of optical systems, in this work.

We developed tissue phantom making techniques which were used to examine the experimental ideas in place of biological samples which are difficult to obtain and work with. Therefore, tissue phantom techniques were studied extensively and realistic models were made. We used agar gel and silicone based tissue phantoms to make multi-layer structures resembling skin tissue. We included deformities in these structures representative of cancerous tissue and controlled the optical properties of the agar samples by adding different doses of titanium dioxide and Indian ink as the main scatterer and absorber, respectively.

Development in different areas of this research paves the way for building a non-invasive, safe, low-cost, compact, and sensitive laser imaging device, which may play an important role in early skin cancer detection. We believe results of this work indicate that LFI can be used for this purpose and the knowledge acquired during the course of this work will help us to apply this system to real biological tissues.

Declaration by author

This thesis is composed of my original work, and contains no material previously published or written by another person except where due reference has been made in the text. I have clearly stated the contribution by others to jointly-authored works that I have included in my thesis.

I have clearly stated the contribution of others to my thesis as a whole, including statistical assistance, survey design, data analysis, significant technical procedures, professional editorial advice, and any other original research work used or reported in my thesis. The content of my thesis is the result of work I have carried out since the commencement of my research higher degree candidature and does not include a substantial part of work that has been submitted to qualify for the award of any other degree or diploma in any university or other tertiary institution. I have clearly stated which parts of my thesis, if any, have been submitted to qualify for another award.

I acknowledge that an electronic copy of my thesis must be lodged with the University Library and, subject to the policy and procedures of The University of Queensland, the thesis be made available for research and study in accordance with the Copyright Act 1968 unless a period of embargo has been approved by the Dean of the Graduate School.

I acknowledge that copyright of all material contained in my thesis resides with the copyright holder(s) of that material. Where appropriate I have obtained copyright permission from the copyright holder to reproduce material in this thesis.

Publications during candidature

Peer-reviewed Papers:

1. **Mowla, Alireza** and Nikolić, Milan and Taimre, Thomas and Tucker, John R and Lim, Yah Leng and Bertling, Karl and Rakić, Aleksandar D, "Effect of the optical system on the Doppler spectrum in laser-feedback interferometry," Appl. Opt. **54**, 18–26 (2015).

2. **Mowla, Alireza** and Taimre, Thomas and Lim, Yah Leng and Bertling, Karl and Wilson, Stephen J. and Prow, Tarl W. and Rakić, Aleksandar D, "A Compact Laser Imaging System for Concurrent Reflectance Confocal Microscopy and Laser Doppler Flowmetry," IEEE Photon. J. **8**, 3900709 (2016).

3. **Mowla, Alireza** and Taimre, Thomas and Lim, Yah Leng and Bertling, Karl and Wilson, Stephen J. and Prow, Tarl W. and Soyer, H. Peter and Rakić, Aleksandar D, "Concurrent Reflectance Confocal Microscopy and Laser Doppler Flowmetry to Improve Skin Cancer imaging: a Monte Carlo Model and Experimental Validation," Sensors **16**, 1411 (2016).

4. Tucker, John R and **Mowla, Alireza** and Herbert, Jeremy and Fuentes, Miguel A and Freakley, Craig S and Bertling, Karl and Lim, Yah Leng and Matharu, Ranveer S and Perchoux, Julien and Taimre, Thomas and Wilson, Stephen J. and Rakić, Aleksandar D, "Self-mixing sensing system based on uncooled vertical-cavity surface-emitting laser array: linking multichannel operation and enhanced performance," Opt. Lett. **39**, 394–397 (2014).

Conference Proceedings and Presentations:

5. **Mowla, Alireza** and Nikolić, Milan and Lim, Yah Leng and Bertling, Karl and Taimre, Thomas and Rakić, Aleksandar D, "Effect of the optical numerical aperture on the Doppler spectrum in laser Doppler velocimetry," IEEE, COMMAD, 72–74 (2014).

6. **Mowla, Alireza** and Taimre, Thomas and Lim, Yah Leng and Rakić, Aleksandar D, "Monte Carlo Model of Laser Doppler Perfusion Imaging in Skin Cancer Detection," Optical Society of America, CLEO-PR, Busan, Korea, 26H3_2 (2015).

7. **Mowla, Alireza** and Taimre, Thomas and Lim, Yah L and Bertling, Karl and Wilson, Stephen J and Prow, Tarl W and Soyer, H Peter and Rakić, Aleksandar D, "Diffuse reflectance imaging for non-melanoma skin cancer detection using laser feedback

interferometry," International Society for Optics and Photonics, SPIE Photonics Europe, Brussels, Belgium 98870T1–98870T11 (2016).

Publications included in this thesis

(A) **Mowla, Alireza** and Nikolić, Milan and Lim, Yah Leng and Bertling, Karl and Taimre, Thomas and Rakić, Aleksandar D, "Effect of the optical numerical aperture on the Doppler spectrum in laser Doppler velocimetry," IEEE, COMMAD, 72–74 (2014) – incorporated in Chapter 4.

Contributor	Statement of contribution
A. Mowla (Candidate)	Wrote the paper (70%), Performed simulations (70%), Performed experiments (70%), Concepts and theory (80%)
M. Nikolić	Wrote the paper (10%), Performed simulations (20%), Performed experiments (20%)
Y. L. Lim	Designed experiments
K. Bertling	Performed experiments (10%)
T. Taimre	Wrote the paper (10%), Performed simulations (10%), Concepts and theory (10%)
A. D. Rakić	Supervised the paper, Wrote the paper (10%), Concepts and theory (10%)

(B) **Mowla, Alireza** and Nikolić, Milan and Taimre, Thomas and Tucker, John R. and Lim, Yah Leng and Bertling, Karl and Rakić, Aleksandar D, "Effect of the optical system on the Doppler spectrum in laser-feedback interferometry," Appl. Opt. **54**, 18–26 (2015) – incorporated in Chapter 4.

Contributor	Statement of contribution
A. Mowla (Candidate)	Wrote the paper (60%), Performed simulations (60%), Performed experiments (60%), Concepts and theory (70%), Designed experiments (70%)
M. Nikolić	Wrote the paper (10%), Performed simulations (20%), Concepts and theory (10%), Performed experiments (20%)
T. Taimre	Wrote the paper (15%), Performed simulations (20%), Developed numerical concepts
J. R. Tucker	Wrote the paper (5%)
Y. L. Lim	Designed experiments (30%), Performed experiments (10%)
K. Bertling	Performed experiments (10%)
A. D. Rakić	Supervised the paper, Wrote the paper (10%), Concepts and theory (20%)

(C) **Mowla, Alireza** and Taimre, Thomas and Lim, Yah Leng and Rakić, Aleksandar D, "Monte Carlo Model of Laser Doppler Perfusion Imaging in Skin Cancer Detection," Optical Society of America, CLEO-PR, Busan, Korea, 26H3_2 (2015) – incorporated in Chapter 4.

Contributor	Statement of contribution
A. Mowla (Candidate)	Wrote the paper (80%), Performed simulations, Concepts and theory (80%)
T. Taimre	Wrote the paper (10%), Concepts and theory (5%)
Y. L. Lim	Wrote the paper (10%)
A. D. Rakić	Supervised the paper, Concepts and theory (15%)

(D) **Mowla, Alireza** and Taimre, Thomas and Lim, Yah Leng and Bertling, Karl and Wilson, Stephen J. and Prow, Tarl W. and Rakić, Aleksandar D, "A Compact Laser Imaging System for Concurrent Reflectance Confocal Microscopy and Laser Doppler Flowmetry," IEEE Photon. J. **8**, 3900709 (2016) – incorporated in Chapter 5.

Contributor	Statement of contribution
A. Mowla (Candidate)	Wrote the paper (80%), Performed experiments (90%), Concepts and theory (80%), Designed experiments (80%)
T. Taimre	Wrote the paper (10%)
Y. L. Lim	Designed experiments (20%)
K. Bertling	Performed experiments (10%)
S. J. Wilson	Provided medical revisions (50%)
T. W. Prow	Provided medical revisions (50%)
A. D. Rakić	Supervised the paper, Wrote the paper (10%), Concepts and theory (20%)

(E) Mowla, Alireza and Taimre, Thomas and Lim, Yah Leng and Bertling, Karl and Wilson, Stephen J. and Prow, Tarl W. and Soyer, H. Peter and Rakić, Aleksandar D, "Concurrent Reflectance Confocal Microscopy and Laser Doppler Flowmetry to Improve Skin Cancer imaging: a Monte Carlo Model and Experimental Validation," Sensors **16**, 1411 (2016) – incorporated in Chapter 4.

Contributor	Statement of contribution
A. Mowla (Candidate)	Wrote the paper (70%), Performed simulations, Performed experiments (80%), Concepts and theory (80%), Designed experiments
T. Taimre	Wrote the paper (10%), Concepts and theory (5%)
Y. L. Lim	Wrote the paper (10%)
K. Bertling	Performed experiments (20%)
S. J. Wilson	Provided medical revisions (30%)
T. W. Prow	Provided medical revisions (30%)
H. P. Soyer	Provided medical revisions (40%)
A. D. Rakić	Supervised the paper, Wrote the paper (10%), Concepts and theory (15%)

(F) Mowla, Alireza and Taimre, Thomas and Lim, Yah L and Bertling, Karl and Wilson, Stephen J and Prow, Tarl W and Soyer, H Peter and Rakić, Aleksandar D, "Diffuse reflectance imaging for non-melanoma skin cancer detection using laser feedback interferometry," International Society for Optics and Photonics, SPIE Photonics Europe, Brussels, Belgium 98870T–98870T (2016) – incorporated in Chapter 6.

Contributor	Statement of contribution
A. Mowla (Candidate)	Wrote the paper (80%), Performed simulations, Performed experiments (80%), Concepts and theory (80%), Designed experiments
T. Taimre	Wrote the paper (10%),
Y. L. Lim	Performed experiments (10%)
K. Bertling	Performed experiments (10%)
S. J. Wilson	Provided medical revisions (30%)
T. W. Prow	Provided medical revisions (30%)
H. P. Soyer	Provided medical revisions (40%)
A. D. Rakić	Supervised the paper, Wrote the paper (10%), Concepts and theory (20%)

(G) Tucker, John R and **Mowla, Alireza** and Herbert, Jeremy and Fuentes, Miguel A. and Freakley, Craig S. and Bertling, Karl and Lim, Yah Leng and Matharu, Ranveer S and Perchoux, Julien and Taimre, Thomas and Wilson, Stephen J. and Rakić, Aleksandar D, "Self-mixing sensing system based on uncooled vertical-cavity surface-emitting laser array: linking multichannel operation and enhanced performance," Opt. Lett. **39**, 394–397 (2014) – incorporated in Chapter 7.

Contributor	Statement of contribution
J. R. Tucker	Wrote the paper (50%), Performed experiments (50%), Concepts and theory (40%)
A. Mowla (Candidate)	Performed experiments (50%), Concepts and theory (40%)
J. Herbert	Wrote the paper (5%)
M. A. Fuentes	Built laser drivers
C. S. Freakley	Designed software
K. Bertling	Wrote the paper (10%)
Y. L. Lim	Designed experiments
R. S. Matharu	Wrote the paper (5%)
J. Perchoux	Wrote the paper (5%)
T. Taimre	Wrote the paper (15%), Concepts and theory (10%)
S. J. Wilson	Wrote the paper (5%)
A. D. Rakić	Supervised the paper, Wrote the paper (5%), Concepts and theory (10%)

Contributions by others to the thesis

In isolation, none of the work presented in this thesis would have been possible. However, I will acknowledge in particular:

- A. D. Rakić contributed to the development of the theories and conceptualization of the ideas and also in designing the experiments as well.
- T. Taimre contributed to the development of numerical and mathematical concepts and theories, both he and Milan Nikolić contributed to the development of Monte Carlo simulation.
- Y. L. Lim, K. Bertling were instrumental in designing and performing experiments.
- S. J. Wilson, T. W. Prow, and H. P. Sayer provided medical advices during this work.

Statement of parts of the thesis submitted to qualify for the award of another degree

- None.

Acknowledgements

I would like to express my deepest gratitude to my principal advisor Aleks, who trusted me and provided me with the opportunity to do my PhD. He is not only a great mentor, but a good person, who supported me during different stages of this work. Thank you very much Aleks. I would also like to thank Thomas for teaching me mathematical concepts, Yah Leng for teaching me optical alignment, Karl for helping me in the lab, Gary and Han for helpful discussions, Jeremy for experimental tips, and also other team members Antony, Tina, Joel, Milan, Bob, and Ben. I would also like to thank Stephen Wilson for being the chair of the committee for me and for his helpful advices as well. I would also like to acknowledge Australian government and the University of Queensland financial supports during the course of this work.

I would also like to thank my lovely wife full-heartedly for putting up with me and being so kind to me. Without her love, I was not able to overcome difficulties at many times during this time. I love you. I would also like to thank my dear parents for being so great and supporting me in my life.

In addition to the people who I mentioned, I learned from other people as well. Meeting all these people and interacting with them provided me with an insight that I believe would shed light on the path which is remained in my life.

Keywords

Laser imaging, skin cancer detection, laser sensing, dual-modality imaging, three-dimensional imaging, Monte Carlo modeling, tissue phantom.

Australian and New Zealand Standard Research Classifications (ANZSRC)

- ANZSRC code: 090606, Photonics and Electro-Optical Engineering (excl. Communications), 100%

Fields of Research (FoR) Classification

- FoR code: 0906, Electrical and Electronic Engineering, 100%

Contents

Abstract ii

Acknowledgements xi

Contents xiii

List of Figures xvii

List of Tables xxiv

List of Abbreviations used in the thesis xxv

1 Introduction 1

1.1 Research Question 1

1.1.1 Traditional Methods of Detection 1

1.1.2 New Technologies for Detection 2

1.1.3 Laser Feedback Interferometry as an Emerging Technology 3

1.2 Aims and Objectives 3

1.3 Contributions 4

1.4 Overview of Dissertation 5

2 Literature Review 7

2.1 Non-invasive Optical Techniques in Skin Cancer Detection 7

2.1.1 Dermoscopy 7

2.1.2 Multispectral Digital Dermoscopy, Melafind 8

2.1.3 Reflectance Confocal Microscopy 9

2.1.4 Optical Coherence Tomography 10

2.1.5 Laser Doppler Flowmetry 11

3 Methodologies **13**
3.1 Monte Carlo simulation . . . 13
3.1.1 Test and Validation . . . 14
3.1.2 Hyperboloid Gaussian Beam . . . 14
3.1.3 Optical System . . . 15
3.1.4 Backscattering Distribution . . . 16
3.1.5 Multi-layer Skin Model . . . 17
3.2 Vertical Cavity Surface Emitting Laser . . . 18
3.3 Laser Feedback Interferometry . . . 19
3.4 Agar Skin Tissue Phantom . . . 22
3.4.1 Materials . . . 22
3.4.2 Making Agar Layers . . . 23
3.4.3 Optical Properties of Agar . . . 24
3.4.4 Titanium Dioxide as Scatterer . . . 25
3.4.5 India Ink as an Absorber . . . 26
3.4.6 Homogeneous Phantom . . . 27
3.4.7 Cancerous Skin Tissue Phantom . . . 28
3.4.8 Micro Tubes . . . 29
3.4.9 Milk and Intralipid . . . 29
3.4.10 More Stable Phantoms . . . 30

4 4. Modeling for Skin Cancer Detection **33**
4.1 Paper A . . . 35
Paper A . . . 35
4.1.1 Abstract . . . 35
4.1.2 Introduction . . . 35
4.1.3 Model . . . 36
4.1.4 Enhanced Backscattering Measurement . . . 37
4.1.5 Results and Discussion . . . 39
4.1.6 Conclusion . . . 39
4.2 Paper B . . . 41
Paper B . . . 41
4.2.1 Abstract . . . 41
4.2.2 Introduction . . . 41
4.2.3 Theory and methodology . . . 42
4.2.4 Results . . . 47

4.2.5 Discussion . . . 55
4.2.6 Conclusion . . . 57
4.3 Paper C . . . 59
Paper C . . . 59
4.3.1 Abstract . . . 59
4.3.2 Introduction . . . 59
4.3.3 Methodology . . . 60
4.3.4 Results and Discussion . . . 62
4.3.5 Conclusion . . . 63

5 5. Concurrent Laser Doppler Flowmetry and Confocal Reflectance Imaging 65
5.1 Paper D . . . 67
Paper D . . . 67
5.1.1 Abstract . . . 67
5.1.2 Introduction . . . 67
5.1.3 Experimental Details . . . 69
5.1.4 Signal Processing . . . 73
5.1.5 Results and Discussion . . . 73
5.1.6 Conclusions . . . 76
5.2 Paper E . . . 78
Paper E . . . 78
5.2.1 Abstract . . . 78
5.2.2 Introduction . . . 78
5.2.3 Methodology . . . 81
5.2.4 Simulation Setup and Results . . . 86
5.2.5 Experimental Validation . . . 89
5.2.6 Discussion . . . 94
5.2.7 Conclusion . . . 98

6 6. Laser Feedback Tomography and Tumorous Skin Phantoms 99
6.1 Paper F . . . 101
Paper F . . . 101
6.1.1 Abstract . . . 101
6.1.2 Introduction . . . 101
6.1.3 Laser Feedback Interferometry . . . 103
6.1.4 Skin Phantom . . . 105

6.1.5 Experiments . . . 108
6.1.6 Experimental Results . . . 109
6.1.7 Monte Carlo Results . . . 110
6.1.8 Conclusion . . . 113
6.2 Confocal Laser Feedback Tomography in Skin Cancer Detection . . . 114
6.2.1 Abstract . . . 114
6.2.2 Introduction . . . 115
6.2.3 Confocal laser feedback tomography . . . 117
6.2.4 Experiments . . . 118
6.2.5 Simulations . . . 123
6.2.6 Conclusion . . . 125

7 7. Parallel Laser Imaging 127
7.1 Optical Laser Head . . . 128
7.2 Thermal Effects on the Operation of VCSEL Array . . . 129
7.3 Characterization of VCSELs in the Array . . . 129
7.4 Driver, Control Software, and Translation Stages . . . 130
7.5 Finding Optimum Operational Currents for VCSELs . . . 132
7.6 Parallel Imaging . . . 132
7.7 Paper G . . . 135
Paper G . . . 135

8 Conclusions 143
8.1 Summary of Findings . . . 144
8.2 Future Work . . . 145

Bibliography 147

List of Figures

3.1 A typical hyperboloid shape. 15
3.2 Numerical optical system including Thorlabs, Inc., C330TME-B and C240TME-B model lenses. 16
3.3 (a) Structure of a 5-layer skin model with epidermis, dermis and subcutaneous layers and one blood vessel. (b) Trace of one photon emitting from the lens into the skin layers. The photon penetrates four layers and undergoes lots of scattering, being absorbed in the third layer. 17
3.4 (a) Trace of one photon which is reflected upon hitting the surface of the skin. (b) Trace of a single photon entering four layers and exiting the skin. . 18
3.5 (a) Trace of a hundred photons. Many enter the skin and blood vessel and after hitting the scatterers, if returned to the lens, will be detected and will contain information about the blood perfusion and skins optical properties as well. (b) The same configuration but with a high refractive index of the blood vessel, so that the photons are reflected from the blood vessel's wall (to show the effect that controlling optical properties can have on the path of photons). 19
3.6 Typical layout of a VCSEL [68]. 19
3.7 Self-mixing interferometry schematic [9]. 20
3.8 (a) Agar powder for research use and (b) hot plate to heat up the mixture. . 23
3.9 The 0.01 gr precision scale used to weigh agar powder. 24
3.10 (a) Using nuts as spacers to make thicker agar gel layers and (b) Using aluminum sticking tapes as spacers to make thiner agar gel layers. 25
3.11 Titanium dioxide particles in agar gel. 26
3.12 Container of titanium dioxide used in this work. 26
3.13 (a) India ink and (b) micropipette used in this project. 27
3.14 (a) Drill and whisk as mechanical stirrer and (b) magnetic stirrer hotplate and a container containing a magnetic bar in it. 28

3.15 (a) Multi-layer agar cancerous skin tissue phantom (the two first layers of epidermis and dermis including a 4 mm whole for the cancerous model to be added) and (b) top view of the mounted cancerous skin tissue phantom. 29
3.16 (a) Circular and rectangular capillary tubes used to model blood vessels and (b) syringe pump to push liquid (blood phantom) through these channels. 30
3.17 (a) Homogenized and (b) Intralipid 20 % used as blood phantom in the experiments. 31
3.18 (a) Two part PDMS (silicon-based gel) and (b) 100 micron thick layer containing TiO_2. 31

4.1 Block diagram of rotating disk laser Doppler velocimetry apparatus based on laser feedback interferometry. 36
4.2 Block diagram of enhanced backscattering measurement apparatus. 37
4.3 Image from CCD camera (a) to measure enhanced backscattering for a C240TME-B lens, including the horizontal (b) and vertical (c) intensity distribution. 37
4.4 Normalized enhanced backscattering peak intensities for four different lenses C330TME-B, C230TME-B, C240TME-B, and C260TME-B, versus their focal lengths. 38
4.5 Simulated Doppler spectra varying beam NA. The beam NAs of the narrowest to widest signals are 0.06, 0.12, 0.22, and 0.32, corresponding to C260TME-B, C240TME-B, C230TME-B, and C330TME-B lenses, respectively. 38
4.6 (a) SNR and (b) FWHM of the Doppler spectra versus beam NA. 39
4.7 Block diagram of laser Doppler velocimetry apparatus. 45
4.8 Block diagram of enhanced backscattering measurement apparatus. 46
4.9 Flowchart of the MC photon transport simulation. 46
4.10 (a) Experimental and (b) simulated Doppler spectra varying angular velocity of the disk. The peaks from left to right correspond to angular velocities 0.22, 0.44, 0.74, 1.30, 1.56, 2.20, 2.93, 3.77, 4.38, 5.12, and 5.65 rad/s. . . 48
4.11 Experimental (red solid triangles) and simulated (blue broken line) results for (a) FWHM and (b) SNR vs. angular velocity of the disk. 48
4.12 (a) Experimental and (b) simulated Doppler spectra varying the beam spot position on the vertical disk axis with constant angular velocity. The peaks from left to right correspond to beam spot positions of 1, 5, 10, 15, 20, 25, 30, 35, 40, 45, and 49 mm. 49

4.13 Experimental (red solid triangles) and simulated (blue broken line) results for (a) FWHM and (b) SNR vs. the beam spot position on the vertical axis with constant angular velocity. 50

4.14 (a) Experimental and (b) simulated Doppler spectra for varying angle of incidence. Lines, in both sub-figures, correspond to angles 3°, 6°, 11°, 16°, 21°, 26°, 31°, and 36° from left to right. 50

4.15 Experimental (red solid triangles) and simulated (blue broken line) results for (a) Doppler frequency, (b) FWHM, and (c) SNR vs. angle of incidence. . 51

4.16 (a) Simulated Doppler spectra, varying fractional change of velocity across the beam spot in the case where the spot is close to the disk center. The beam spot distances from the center of the disk for widest to narrowest spectra are 5, 10, 20, 40, and 70 µm. (b) FWHM (diamonds) and SNR (circles) simulation results vs. beam spot distance from disk center, varying fractional change of velocity across the beam spot in the case where the spot is close to the disk center. 44 µm lines show the boundaries between close and distant regimes. 53

4.17 Simulated Doppler spectra varying beam NA. The beam NAs used for the narrowest to widest spectra are 0.04, 0.05, 0.06, 0.08, and 0.12. 54

4.18 FWHM (diamonds) and SNR (circles) simulation results vs. beam NA. . . . 54

4.19 The schematic view of the six-layer skin tissue with the cylindrical tumorous area in the second layer. 61

4.20 Perfusion maps of three types of skin lesions with RBCs concentrations of (a) two (b) four and (c) six times higher than normal and velocities of 1.5 times higher than normal. 62

5.1 Laser feedback interferometry imaging set up as an integrated reflectance confocal microscopy and laser Doppler flowmetry imaging system. 70

5.2 Two inlet rhombic microfluidic channel. Flow is pushed through from inlet *a* when a stop valve is placed on *b*. Red shaded square shows the scan area and signal to background ratio is calculated along the blue broken line. 70

5.3 Cross-sectional view of microfluidic channel. The channel has a depth of 500 µm with 188 µm thick walls made of Zeonor. A focused laser beam is projected into the channel to measure confocal reflectance and Doppler signals due to diluted milk flow at the velocity of $\vec{V}$ (gray arrows). The focused beam has a sensing volume as defined by the gray ellipse. The insets show i) LFI signal containing LDF spectrum and RCM signal obtained from the LFI sensor. ii) depicts the LDF spectrum and iii) the RCM signal, which are both derived from i). 71

5.4 Frequency and time domain signals from three typical states of the target as (a) signal from a typical flow area, (b) signal from a point outside the flow area, and (c) signal in absence of the target (noise). Red broken lines are the Savitzky–Golay filtered power spectrum and green broken lines are the Savitzky–Golay filtered power spectrum in the absence of target which shows the noise floors. 74

5.5 Normalized scan results and images of (a) Doppler flowmetry, (b) confocal reflectance, (c) addition (of the images in a and b), (d) multiplication(of the images in a and b), (e) Doppler flowmetry (image a) with a limited range, and (f) multiplication (image d) with a limited range. 75

5.6 Average signals on the lateral scans of the microfluidic channel over the rectangular area (along the blue broken line in Fig. 5.2). Blue, green, and red broken lines show average Doppler, confocal reflectance, and multiplication signals, respectively. 76

5.7 LFI with an RCM implementation based on a VCSEL as both the emitter and the detector. The VCSEL aperture with a diameter of a few microns acts as the spatial RCM pinhole in this structure, and the LFI signal is generated due to the self-mixing effect inside the VCSEL cavity. 83

5.8 Block diagram of numerical model including a confocal LDF system raster scanning a six-layer skin tissue model to make the confocal reflectance and Doppler images of an embedded tumour model. 84

5.9 Monte Carlo simulated images of typical (**a**) KSC1 and (**b**) KSC2. Parts (i) and (ii) of the images depict blood Doppler and confocal reflectance images of 5 mm diameter tumours, respectively. Part (iii) shows the multiplication image, which is formed by multiplying Parts (i) and (ii), pixel-by-pixel. 88

5.10 Improvement in the signal to background ratio as a result of multiplying Doppler flowmetry and confocal reflectance images. Red broken, blue dotted and black solid lines in (**a**) and (**b**) of this image correspond to the Doppler flowmetry, confocal reflectance and multiplication signals acquired along center-crossing horizontal axes in (a) and (b) of Figure 5.9, which correspond to typical KSC1 and KSC2 simulated models, respectively. . . . 89

5.11 Experimental confocal LFI apparatus in the dual-modality imaging application, scanning a microfluidic channel containing diluted Intralipid flow. 90

5.12 (**a**) Top view of the microfluidic channel (the red broken line shows the center-crossing axis alone which SBR was calculated) and experimental normalized (**b**) Doppler flowmetry, (**c**) confocal reflectance and (**d**) multiplication images. 92

5.13 Red broken, blue dotted and black solid lines show average Doppler flowmetry, confocal reflectance and multiplication signals, acquired along the center-crossing axis of the microfluidic channel (shown with the red broken line in Figure 5.12a), respectively. 93

5.14 (**a**) Frequency and (**b**) time domain confocal LFI signals, obtained from the voltage of the VCSEL terminals. Red and black broken lines in (**a**) show the filtered Doppler spectrum and noise floor (in the absence of target), and the first large spike in (**a**) is the first harmonic of the signal (as the beam is modulated at 1 kHz); its magnitude with respect to noise floor is a measure of the confocal reflectance signal. The orange broken line in (**b**) shows the modulating signal at 1 kHz, and two grey broken lines show the average high and low time domain signals corresponding to the unblocked and blocked modes of the beam (by means of the optical chopper), respectively, indicating confocal reflectance. Doppler fluctuation can be seen on the high level of the time domain signal when the beam is not blocked. . . . 94

5.15 Simulated total reflectance from a typical tumourous skin model in our model (blue line) compared to the diffusion theory formula (red broken line), versus the ratio of the reduced scattering coefficient to absorption coefficient. 96

6.1 Three mirror model of laser in the presence of external target. 103

6.2 Agar skin tissue phantom; (a) a high absorptive 500 μm layer on a 150 μm thick cover slip resembling the epidermis, (b) a high scattering 1000 μm layer enclosing a 4 mm diameter cylindrical lower scattering tumorous model as the equivalent of dermis, (c) 3.15 mm pure agar layer resembling the subcutaneous tissue and a plastic wrap, (d) top view of the skin phantom. 106
6.3 Experimental set up; laser feedback interferometry system raster scanning a three-layer skin tissue phantom including a KSC area. 109
6.4 Laser feedback interferometry diffuse reflectance imaging experimental results; sub-figures of (a) to (h) illustrate the scan results at the focal depths of 280, 415, 550, 685, 840, 955, 1090, and 1225 μm from the surface of the first agar layer, respectively. (i)s show raw self-mixing image, (ii)s show the two dimensional median filtered image, and (iii)s show the two dimensional Gaussian filtered image. 111
6.5 Monte Carlo simulation results for the three-layer tumorous skin model equivalent to the agar gel sample; sub-figures of (a) to (l) illustrate the simulated results at the focal plane depths of 185, 320, 455, 590, 725, 860, 995, 1130, 1265, 1400, 1535, and 1670 μm from the surface of the first skin layer model, respectively. 112
6.6 Confocal laser feedback tomography apparatus with VCSEL's aperture acts as a confocal pinhole to eliminate out of focus beam. VCSEL current is modulated at a low level around the operating current to create two levels of LFI signals. Beam is focused on a silicone-based three-layer KSC tissue phantom. 118
6.7 Average signal levels (red dotted line), dynamic range of the signal at optical sections (green dashed line), and compensated dynamic range (blue solid line) versus the scan depth from the top of the cover slip (all normalized to the maximum levels), for three types of KSC tissue phantoms: (a) infBCC, (b) nodBCC, and (c) SCC. 121
6.8 Images provided at different depths of SCC phantom, starting at just above the top surface of the epidermis layer and ending at the depth of 400 µm in subcutaneous tissue. Stronger contrast can be seen at depths where cancerous model is incorporated, enclosed in the dermis layer. 122
6.9 Isosurfaces for (a) infBCC at CRL of about 0.7, (b) nodBCC at CRL of about 0.5, and (c) SCC at CRL of about 0.3. (i), (ii), and (iii) represent the angle, top, and side views, respectively. Axes of the plots are the coordinates of the scanned volume in µm. 123

6.10 A constant reflection level (red plane) at 0.3 cutting one of the optical sections of SCC phantom (regions below the constant reflection level will be enclosed in the isosurface view). 124
6.11 Numerical isosurfaces for (a) infBCC, (b) nodBCC, and (c) SCC, when (i), (ii), and (iii) represent the angle, top, and side views, respectively. Axes of the plots are the coordinates of the scanned volume in µm. 125

7.1 Parallel readout components (a) mounted 24 channel VCSEL array including two thermistors at the ends (b) 24 channel driver including receivers and amplifiers of the channels. 128
7.2 (a) Light-current curves for 7 exemplar channels of the VCSEL array and (b) beam profile of 12 exemplar channels of the VCSEL array. 130
7.3 Translation stages and optical head on an optical table. 131
7.4 Three rounds (R1 to R3) of measurements to find the optimum operational currents (which are the currents measured at R3 or green bars). 132
7.5 (a) Flow channel and (b) Doppler flowmetry parallel imaging result of the flow channel containing diluted milk. 133
7.6 Experimental setup for measuring velocity on a rotating disk. The disk is tilted around the vertical axis by 5° to produce a small velocity component in the direction of the laser beam. 137
7.7 SNR of central laser (Channel 12) versus injection current with different levels of current in neighbouring lasers. The current in the neighbouring lasers are all biased at the same current while the current of the central laser is varied.(circles - Single Channel, squares - Multichannel 2 mA, up triangles - Multichannel 5 mA, down triangles - Multichannel 8 mA, diamonds - Multichannel 10 mA). 139
7.8 Close up photo of the array and thermal images for the different separation distances used for the experiments in Fig. 4. a) Photo, b) 660 µm spacing, c) 440 µm spacing, d) 220 µm spacing. Channel 1 is located at the left hand side of the images. 140
7.9 SNR of central laser (Channel 12) versus injection current with simultaneous operation of six neighbouring lasers biased at 10 mA. There is an equal separation distance between lasers with the separation distance varying for different experiments. (circles - 660 µm spacing, squares- 440 µm spacing, triangles - 220 µm spacing). 141

List of Tables

4.1 Effect of system parameters on Doppler frequency, FWHM, and SNR. Major and minor effects are shown by ✓and ✗, respectively. 57

5.1 Six-layer skin tissue model, data from [110]. 86

Abbreviations

LFI: Laser feedback interferometry
RCM: Reflectance confocal microscopy
VCSEL: Vertical cavity surface emitting laser
LDV: Laser Doppler velocimetry
NA: Numerical aperture
MC: Monte Carlo
SNR: Signal to noise ratio
FWHM: Full width at half maximum
BS: Beam splitter
CCD: Coupled Charged device
NMSC: Non-melanoma skin cancer
LDPI: Laser Doppler perfusion imaging
RBC: Red blood cell
KSC: Keratinocyte skin cancer
BCC: Basal cell carcinoma
SCC: Squamous cell carcinoma
SBR: Signal to background ratio
PCB: Printed circuit board
PDMS: Polydimethylsiloxane

Chapter 1

Introduction

1.1 Research Question

The most common type of cancer in human beings is skin cancer, and the incision rate of keratinocyte cancers (basal cell carcinoma, squamous cell carcinoma), the most prevalent types of skin cancer, have seen a significant increase over the past decade [1]. Australia has the highest incidence of basal cell and squamous cell carcinoma cancers in the world, with about 2% of the population estimated to develop such cancers each year [1]. In Australia during 2011, 543 people died from non-melanoma and 1544 died due to melanoma skin cancers. Finding skin cancer in its early, treatable stages is critical for favorable prognosis, thereby decreasing the public health burden [2]. At the moment, there are a number of competing technologies for the early detection of skin cancer. Each with their own merits and drawbacks. There remains a clear need for a non-expensive, compact, reliable, safe, easy to use, fast, sensitive, and non-invasive skin imaging technology to aid in the early detection of skin cancer.

1.1.1 Traditional Methods of Detection

Clinicians have the simple choice of using the oft-recommended ABCDE rule to guide naked-eye examinations of pigmented lesions: A = lesion asymmetry, B = border irregularity, C = color variability, D = diameter typically the size of a pencil eraser (1/4 inch or 6 mm), E = evolving or any change in size, shape, color, elevation, or another trait, or any new symptom such as bleeding, itching, or crusting. However, less than 17% of the changing lesions are melanoma [3].

Skin cancer is most often detected by incidental or deliberate skin self-examination.

Studies of skin self-examination overwhelmingly focus on melanoma. Melanoma self-detection rates range from 40% to 55%. In Australia, 44% of all melanomas and 73% of first melanoma recurrences are detected by patients or their partners [3]. Clinical skin examination leads to earlier diagnosis of skin cancer in general and reduced melanoma thickness at diagnosis compared with skin self-examination. A population-based case control study conducted in Queensland found that having a whole-body clinical skin examination within the past 3 years reduced the risk of being diagnosed with a thick melanoma by 14% [3].

Traditional methods of detection without the use of new technologies are not particularly accurate, and early detection using traditional methods is challenging. Moreover, a final diagnosis needs examination of biopsies which is invasive. Consequently there is a pressing need for new non-invasive technologies and techniques to improve chances of early detection of skin cancer.

1.1.2 New Technologies for Detection

The use of dermoscopy has opened a new visual method of investigating pigmented skin lesions, thus increasing the effectiveness of clinical diagnostic tools to differentiate melanoma from other pigmented skin lesions [4].

Another existing technology is reflectance confocal microscopy (RCM), a non-invasive imaging technique, which uses a near-infrared laser beam to penetrate the upper skin layers, where it backscatters upon contact with skin structures [5]. The high refractive index of melanin and melanosomes causes more light to be reflected back to the confocal microscope, which causes these areas to appear brighter. As such, RCM is suitable for examining melanocytic lesions [3].

Total cutaneous photography provides a temporal comparison of lesions, which allows clinicians and patients to recognize new and subtly changing lesions so it can be used for early detection of skin cancer [6]. Teledermatology is a subspecialty in the medical field of dermatology and probably one of the most common applications of telemedicine and “E-health”. At the moment, a dermoscopy device that attaches to an i-Phone and is specifically designed for mobile teledermatology is commercially available [3].

MelaFind is a hand-held imager that analyzes lesions using multi-spectral imaging and extracts information from the images. Unlike other technologies, MelaFind provides a biopsy recommendation for the lesion based on the analysis that it performs and there is no need for a dermatologist [7].

Although numerous techniques have been suggested and used for the purpose, the

field is far away from being mature and there is still a need for a compact, non-expensive, safe, easy to use, sensitive, versatile, and reliable tool.

1.1.3 Laser Feedback Interferometry as an Emerging Technology

Laser feedback interferometry (LFI) has proved its potential in sensing and biomedical applications like flowmetry, velocimetry, blood perfusion imaging, confocal reflectance imaging, and refractive index measurements in the infrared frequency range [8–10]. Variation in optical properties (refractive index) of skin structure [11] and blood perfusion [12, 13] due to cancerous cells, make LFI a possible technique for skin cancer detection in its early stages. In the infrared frequency range, the absorption coefficient of the skin tissue is relatively low and the photons can penetrate a couple of millimeters into the skin. Using 850 nm infrared VCSEL in LFI helps to have better a penetration depth compared to visible lasers. In this project we investigate the potential for detection of melanoma and non-melanoma skin cancers using this technique.

1.2 Aims and Objectives

Human skin is the largest organ of the body that protects us against water loss and pathogens. Skin has a very complex multilayer structure and there are a huge number of diseases that threaten the skin. Fortunately, most of the deformities of the skin, especially the ones related to the outer layer, can be easily seen and diagnosed.

However, some of the diseases can not be seen in the early stages and are developed in the lower skin layers. The main aim of this work is to develop a technique to assess the health of the skin in the inner layers beneath the surface. In particular, an optical imaging technique to image the skin lesion, suspicious of cancer, in early stages is desired. In order to proceed with this goal, not only we need to have a good understanding of the optical methods and systems, but also a deep insight into the pathological aspects of the cancerous tissue is needed. Therefore, in this project I studied the hallmarks of cancer, which are the common types of functional and morphological changes that cancer causes to the affected tissue [14]. I particularly focused on the changes that can be optically detected. The main bio-markers of cancer that we used as indicators in this project were, cancerous blood flow [12, 13, 15] and optical properties abnormality [11]. Blood perfusion is one of the indicators of the skin condition. Laser Doppler flowmetry is one of the established methods of measuring blood perfusion which is an interferometric

technique [16]. In addition, due to histological and ultrastructural changes, optical properties of tumorous tissues will change [17]. Therefore, optical properties of the tissue that can be detected and imaged by biomedical optical imaging techniques, were also used as another bio-marker in this project.

To realize the idea, we used LFI using VCSELs in laser Doppler flowmetry and confocal reflectance microscopy configurations for blood perfusion and reflectance imaging, respectively. VCSEL array was also used in a parallel read-out system to increase the speed and resolution of the imaging.

The other primary aim of this project was to develop tissue phantoms in order to be used in imaging experiments and evaluate the system, as access to biological tissues is hard and time consuming. I developed tissue phantoms based on agar gel and silicone based phantoms. I used homogenized milk and Intralipid as blood phantoms in this thesis.

Developing a powerful numerical engine for investigating light–tissue interaction, in particular how laser light interacts with a numerical skin cancer model, was the other aim of this work. Monte Carlo is the gold-standard simulation technique which has been extensively used in the area of optics-tissue interactions [18]. We developed an object-oriented Monte Carlo tool and we used it to model optical systems, during this thesis.

The major aims of this work can be listed as:

1. Developing a non-invasive technique for skin tissue imaging with capability of being used in skin cancer detection.

2. Study the bio-markers of diseased skin tissues that can be used in biomedical optical imaging systems.

3. Propose new techniques to improve imaging effectiveness.

4. Develop technologies to make stable and versatile tissue phantoms.

5. Develop a simulation engine that can be used in numerical modeling of the systems.

1.3 Contributions

The original contributions of this thesis are as follows:

- Paper G, for the first time showed the improvement in the signal to noise ratio in the concurrent operation of a 24-channel VCSEL array in a parallel imaging system.

- Paper B presents a deep insight into the effects of optical system on the morphology of the Doppler spectrum in an LFI system configured in a laser Doppler velocimetry form.
- Paper D, for the first time combined laser Doppler flowmetry and confocal reflectance microscopy in an integrated optical system, improving the capability of the imaging system.
- Paper E shows the role that the combination technique, which is suggested in paper D, can play in improving skin cancer detection, using a range of Monte Carlo simulation and experimental validation.
- Results in section 6.2 for the first time presents tomographic images of a cancerous skin tissue phantom provided by means of an LFI system.
- Paper F shows the use of agar cancerous skin tissue phantom in an LFI reflectance imaging system.
- Paper C examined the feasibility of Doppler perfusion imaging by means of LFI through Monte Carlo simulations.
- Developing agar and silicone based tissue phantoms.
- Developing Monte Carlo simulation and use it in different configurations during the thesis.

1.4 Overview of Dissertation

This thesis begins with an introduction which is followed by a literature review in ch. 2. There will be an overview of the methodologies used throughout this project, in ch. 3. In ch. 4, using a range of Monte Carlo simulations, the effects of optical system and laser beam shape on the Doppler spectrum are investigated and then the use of different modalities such as Doppler flowmetry and confocal reflectance in skin cancer detection is studied by numerically modeling the optical system and the cancerous skin tissue. Chapter 5 discusses dual-modality imaging which can improve the effectiveness of the imaging systems. Then it is followed by ch. 6 which contains the experimental and simulated results of a laser feedback tomography system which uses optical sectioning to present three dimensional images of a sample. Subsequently, in ch. 7 the idea of parallel imaging is introduced using a 24 channel VCSEL array, which is followed by conclusion section

of the thesis in ch. 8. Following the conclusion, appendix 3.1 discusses the Monte Carlo simulation and appendix 3.4 gives the technical methods and considerations which were used during the thesis to make tissue phantoms.

Chapter 2

Literature Review

Traditional methods of skin cancer detection were discussed in ch. 1. Traditionally, the final decision as to whether a suspected tissue sample is cancerous, in most cases, is based on the histology microscopic results after a skin biopsy of suspicious lesions. This procedure is invasive, painful, leaves a scar, and time consuming. Therefore there is a need for a non-invasive, accurate, compact, and inexpensive device to be used in skin cancer detection. Optical techniques are one of the main options as they are non-invasive, able to penetrate tissue, safe, high resolution, compact, and in most cases inexpensive. Since a few decades ago, numerous optical techniques have been suggested to be implemented for this purpose. In this chapter, I will introduce some of these techniques, with a focus on the ones which are believed to be the best alternatives to current histology tests, as well as novel and promising approaches.

2.1 Non-invasive Optical Techniques in Skin Cancer Detection

2.1.1 Dermoscopy

Dermoscopy is the examination of a skin lesion by means of a dermascope and it is one of the simplest non-invasive techniques which can be used in skin tumor detection. Dermoscopy is based on optical magnification of the morphological characteristics of the skin lesion which is impossible to see with naked eye and it is specially effective for examining pigmented skin lesions [19–24]. The term dermoscopy was first introduced in 1991 [25] and diagnosis of skin tumors using a dermascope has its roots in a diagnostic technique which was called pattern analysis and was introduced in 1987 [26]. Before dermoscopy,

detection of skin cancer was mostly based on visual examination and also ABCDE rules. Dermoscopy cannot provide images in the cellular scale but it is a tool to connect macroscopic clinical dermatology with the other principal approach in dermatology that depends on microscopic histopathology [20]. Most of the common dermascopes have magnifications of $\times 10$, although some of them can have magnification factors of up to $\times 100$ [19].

Detection using a dermascope is based on the morphological features of skin tumor tissues. Different procedures have been proposed in order to use dermascopes as a detection tool. For instance, a two-step method was proposed in [20]; the first step is differentiate between melanocytic and non-melanocytic lesions, and in the second step four different algorithms are applied to differentiate melanoma from other benign melanocytic lesions [20]. Furthermore, Menzies *et al.* used dermoscopy to examine pigmented basal cell carcinomas and they established a diagnostic technique that for a lesion to be diagnosed as pigmented basal cell carcinoma it should have one or more of these 6 features: large gray-blue ovoid nests, multiple gray-blue globules, maple leaf-like areas, spoke wheel areas, ulceration, and arborizing tree-like telangiectasia [27]. In that research, based on independent test sets, sensitivity of 97% was measured for the diagnosis of pigmented basal cell carcinoma and specificity of 93% and 92% were measured for the diagnosis of invasive melanomas and benign pigmented skin lesions [27]. However, the morphological features of pigmented basal cell carcinoma are not limited to the classical features presented in Menzies *et al.* work and other diagnostic criteria have been suggested in other research. This is because of the various combinations of histopathologic traits that pigmented basal cell carcinoma can possess [23].

2.1.2 Multispectral Digital Dermoscopy, Melafind

A multispectral imaging system provides images at specific wavelength across the electromagnetic spectrum. This can be achieved through using filters or photodetectors which are sensitive to a specific wavelength. Multispectral imaging when bound together with a digital dermascope is able to record images of skin lesions at different wavelengths in a range from visible to near-infrared spectrum. These images can be then processed using computerized processing techniques and pattern analysis algorithms to trace common features of specific types of skin cancer such as melanoma.

Because using a dermascope still needs high level of training, some researchers tried to invent fully automatic diagnostic tools that eliminate the need for dermatologist [28,29]. For instance, a commercial multispectral imager called Melafind was developed and used effectively to differentiate between melanoma and other melanocytic nevi [28]. This device

saves images in a computer and performs multi-step computer analysis based on mathematical algorithms to evaluate a lesion. First it demarcates areas at higher contract or level of pigment content. Then it computes features of the lesion based on different paradigms such as ABCDE rules. Finally, it combines different values of computed featured to come up with a score which is a measure for the diagnosis [28]. High level of sensitivity and specificity have been reported for differentiation of melanoma from melanocytic nevi using Melafind [28]. Diagnostic accuracy of Melafind has been studied in some other research showing promising results as well [30].

2.1.3 Reflectance Confocal Microscopy

Reflectance confocal microscopy (RCM) is probably the most accepted non-invasive technique to be used in skin cancer detection, at the moment, and it is widely used in clinical trials for this purpose [31–35]. In RCM, out of focus light is eliminated by situating a spatial pinhole at the focal point of the beam. This pinhole blocks the reflected light coming from out of focus areas. This technique increases the resolution and contrast of the image and provides the ability to obtain *in vivo* images from inside living organism, in reflection mode [36]. RCM can achieve submicrometer lateral resolution but the penetration depth is limited to several hundreds of micrometers [37]. Although the idea was first proposed in 1957 [38], it was only after the invention of lasers and computer systems that it found its way in biomedical community as a non-invasive imaging technique [39]. Researchers started to use RCM to make *in vivo* images of skin tissue using skin's melanin as a contrast agent [40]. RCM can be performed in normal reflectance or fluorescence modes to provide images of various micro-structures of skin tissue. Fluorescent mode is achieved by administering fluorescence dye to skin tissue [41].

After the early days of applying RCM to image skin tissue structures, researchers then focused on applications such as detecting benign and malignant melanocyte and keratinocyte tumors and statistical studies on the effectiveness of RCM in skin cancer detection [5]. Fluorescent confocal laser scanning microscopy was evaluated clinically by a systematic examination of normal and diseased skin tissues [42], examining some features of non-melanoma skin cancers (basal cell carcinoma and actinic keratosis) such as increased vascularity and nuclear pleomorphism [42]. Rishpon *et al.* studied squamous cell carcinoma and actinic keratosis using RCM and were able to detect a number of cancerous features in the morphology of the tissues such as polygonal nucleated cells, atypical honeycomb pattern of the spinous-granular layer of the dermis, round nucleated cells, and round blood vessels in superficial dermis [34]. In addition to non-melanocytic lesions,

RCM was also used to evaluate melanocytic lesions in work such as [35]. In this research four different features that can be used to differentiate melanocytic from non-melanocytic lesions where presented as: cobblestone pattern of epidermal layers, pagetoid spread, mesh appearance of the dermoepidermal junction, and the presence of dermal nests. Moreover, a two-step algorithm was developed to diagnose skin tumors [35]. Scope *et al.* used aluminium chloride to increase the contract of the images and by varying the depth of optical sectioning, three consistent patterns of tumorous margins were identified as: epidermal margins, peripheral dermal margins, and deep dermal margins [33]. In that research, basal cell carcinomas were identified at peripheral or deep dermal margins and honeycomb patterns of squamous cell carcinomas were also identified at the epidermal margins [33]. In addition, a study was run to assess the effectiveness of using RCM in diagnosing nodular melanomas, a type of skin tumor which can simulate all kinds of melanocytic and non-melanocytic lesions [32]. It was shown that RCM can be considered as an effective tool in diagnosing nodular lesion and it shows high sensitivity and specificity for the diagnosis of melanoma [32].

2.1.4 Optical Coherence Tomography

Optical coherence tomography has been one of the most successful translational optical imaging techniques that has a high level of clinical acceptance in some areas such as ophthalmology, cardiology, and dermatology [37]. Optical coherence tomography is a low-coherence interferometry technique which is able to provide sub-micrometer resolution images of biological tissues non-invasively [37, 43, 44]. Light sources with low time-coherence and broad-bandwidth such as superluminescent diodes can be used in this systems [45]. There are two arms in these systems; one is a reference arm and the other is a sample arm. Pulses that reflect back from the reference mirror and sample interfere with each other and a part of the reflected sample signal which comes from the right depth within the sample, gives rise to an interferometric pattern (within coherence gate). In fact the time-of-flight of the signal coming back from the sample reveals information about the longitudinal location of the reflection sites [43]. Lateral scans in addition to longitudinal scans, provide slice images which can make tomographic images when all are put together.

It has also been suggested as an *in vivo* technique in skin cancer detection [46–49]. Based on the fact that in basal cell carcinoma the normal appearance of tumorous tissue is altered, polarization-sensitive optical coherence tomography was used to distinguish

between healthy and tumorous skin and it was shown that a gradual translation from normal to a lobular cancerous form happens at the borders [46]. In the studies that have been done using optical coherence tomography, it is expected to detect changes in normal skin architecture and any kind of disorder in the shape of epidermis and upper dermis by means of this technique. For instance Gambichler *et al.* have been able to observe features in the images provided from basal cell carcinoma such as large plug-like signal-intense structures, honeycomb-like signal-free structures, and prominent signal free cavities in the upper dermis, which are correlated with histology examination [48]. However, one of the deficiencies in diagnosis based on this technique is a lack of specificity. For example, there are statistically insignificant differences between skin cancers of types such as nodular, multifocal superficial, and infiltrative basal cell carcinomas [48]. Despite this, specificity is high in differentiating between normal and cancerous skin tissues [49]. One of the approaches to improve diagnosis thorough optical coherence tomography is by combining different modalities in the imaging process such as optical Doppler tomography [50] which is able to image blood flow in addition to the structure of a biological sample. Currently, lots of research groups are carrying research in this area [37]. Optical coherence tomography remains one of the most promising modalities to be used as a skin cancer detection device.

2.1.5 Laser Doppler Flowmetry

In laser Doppler flowmetry light scattered from a moving particle undergoes a frequency shift, due to the Doppler effect, that is proportional to the component of its velocity in a direction determined by the direction of illumination and frequency of the beats produced by the scattered light and a reference beam [51]. Alternatively, it is possible to observe the beats produced by scattered light from two illuminating beams incident at different angles. Laser Doppler interferometry can be used for measurements of the velocity of moving material, as well as for measurements, at a given point, of the instantaneous flow velocity of a moving fluid to which suitable tracer particles have been added. The frequency of the beat signal is given by the relation [51]:

$$\Delta f = \frac{1}{2\pi}(\mathbf{k}_s - \mathbf{k}_i) \cdot \mathbf{v}\,, \tag{2.1}$$

where Δf is the Doppler shift in the frequency of the light, $\mathbf{k}_s$ and $\mathbf{k}_i$ are the wave vectors of the scattered and incident waves, respectively, and $\mathbf{v}$ is the velocity vector of the target.

From early times of laser invention, researchers thought of using laser Doppler to measure blood flow, both in the larger blood vessels [52] or skin blood perfusion (microvascularization capillary networks) [16, 53]. Laser Doppler signal is usually an indicator of flux, velocity, and concentration of the moving red blood cells [54]. On the other hand we know that abnormal blood perfusion is one of the indicators of skin cancerous tissues [14] as vasculogenic tumor cells cause neovascularization that plays an important role in the growth of tumor [55, 56]. Therefore, laser Doppler flowmetry has been proposed as a tool to be used in detection of benign and malignant skin tumors [12, 13, 57]. Stücker *et al.* investigated the possibility of differentiating between benign and malignant skin tumors by assessing the level of microvascularization using laser Doppler perfusion imaging, and concluding that blood perfusion level has a direct relationship with the malignancy of the skin cancer [12, 13, 58]. However, this technique suffers from some limitations such as lack of specificity that needs to be addressed.

Chapter 3

Methodologies

This chapter discusses the methodology which was used to accomplish this thesis. There were two main approaches in achieving the goals of this work. The first approach was through numerical simulation. Investigating the interactions of photons, optical systems, and soft tissue phantoms can be carried out using numerical techniques. Among the accepted numerical techniques, Monte Carlo is widely known as the gold standard for modeling these systems. Therefore, we developed a Monte Carlo engine to model our optical systems, examine our hypothesis, predict the results, and optimize the apparatus. To execute a Monte Carlo model, we need to model the optical setup, targets which are quasi-transparent to light, define the optical properties of the parts in the model, define a large population of photons, determine characteristics for each one of the photons, study the interactions, collect the detected photons, look for the history of the detected photons and changes in their characteristics, and finally make the plots and data that show the results. Section 3.1 highlights the specifics of the Monte Carlo programming conducted in this thesis.

The second approach was experimental that can be categorized into three sub-branches of the employed laser, laser imaging technique (laser feedback interferometry), and tissue phantoms (agar and silicone based tissue phantom). The first two categories will be discussed in sections 3.2 and 3.3. A detailed explanation of tissue phantom making techniques is included in section 3.4.

3.1 Monte Carlo simulation

Monte Carlo (MC) methods are a broad class of simulation techniques, which have been successfully applied to problems in physics, engineering, finance, biology, medicine, and

statistics [59, 60]. The use of MC is especially common and applicable in the area of photon transport simulation in which one can replace the radiative transfer equation by more flexible MC methods [18]. We used the standard MC practice of treating the laser beam as being comprised of a large number of photons, each behaving as a stand-alone particle. We developed software which accurately reproduces the experimental results through MC simulation and thereby equipped us with a powerful tool to predict and analyze the behavior of complicated systems. We used object-oriented MATLAB programming. Object oriented programming helped us to deal with complex geometrical structures easily.

3.1.1 Test and Validation

To verify the effectiveness of the MC simulation model in the case of the laser Doppler velocimetry, a comprehensive set of experiments has been performed sweeping different parameters in the rotating disk velocimetry system and comparing the Doppler signal obtained by LFI and the results of MC simulations. This system included the photons illuminated from a 850 nm VCSEL with a linewidth of a few MHz and a divergence angle of 7.5 degrees collimated with a C240 lens to a 1.9 mm diameter beam and focused on a rough Aluminum disk on the vertical axis passing from the center. Photons will be absorbed or reflected from the surface with a Lambertian distribution and a Gaussian coherent backscattering distribution, each carrying its own Doppler shift. The simulation reproduces the trends in Doppler signal characteristics including SNR, full width at half maximum (FWHM), and central Doppler frequency. The simulated Doppler spectrum of the detected photons are consistent with the experimental results and therefore the basic simulation model is validated for further use. The results of this investigation were published in paper B.

3.1.2 Hyperboloid Gaussian Beam

In order to obtain the most realistic numerical results, it is critical to define the distribution of the photons in a way to shape the beam in a realistic way and determine the angles and directions of the photons to resemble the beam in a realistic way. In the main numerical engine, we defined the laser beam as a Gaussian beam with a hyperbolic nature [61]. This arrangement of photons and their orientations at the beam spot on the focal plane, rules the specifications of photon-target collisions and play an important role in forming the signal. In most of the cases, laser beams occur in the form of Gaussian beams, which

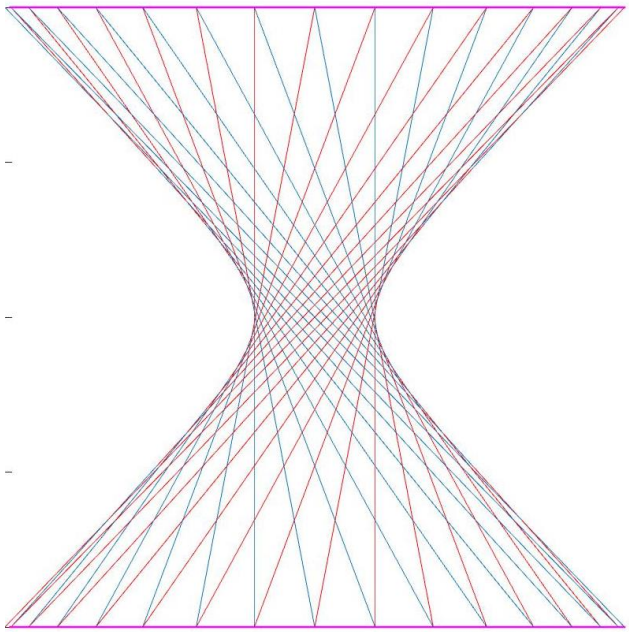

FIGURE 3.1: A typical hyperboloid shape.

means that the transverse profile of the optical intensity of the beam has a Gaussian distribution [62]. Therefore we defined the initial photon population on the objective lens surface with a Gaussian spatial probability distribution, assuming we know the collimated beam diameter incident upon the lens. After defining the initial position of the photons, photons were launched toward the sample in a hyperboloid shape [61]. The initial direction of each photon was assigned by considering its position relative to the center of the lens, as well as the numerical aperture and focal length of the lens, such that the spatial distribution of photons at the focal plane of the lens was still Gaussian and photons move in a hyperboloid shape. Figure 3.1 shows a typical hyperboloid.

3.1.3 Optical System

We defined numerical lenses in the MC model based on the physical characteristics of commercially available Thorlabs, Inc., C330TME-B and C240TME-B lenses. Numerical aperture and effective focal length for C330TME-B are 0.68 and 3.1 mm, and the figures for C240TME-B are 0.5 and 8 mm, respectively. Geometrical features of these lenses were extracted from datasheet and aspheric coefficients of the lenses were used to define the surfaces and to determine the light refraction angle on the surfaces. Optical system was used to focus the beam on the target and also for collecting the back reflected beam and detecting a population of the photons that make their way back into the laser cavity.

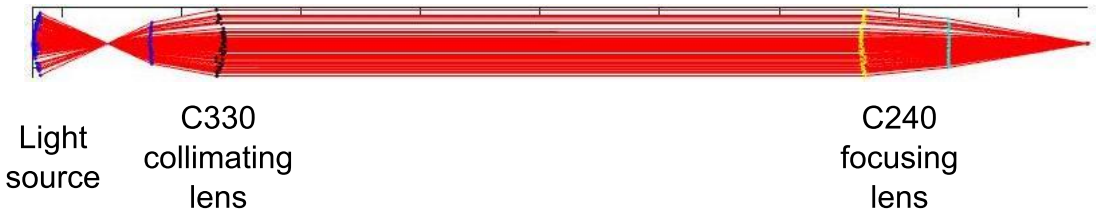

FIGURE 3.2: Numerical optical system including Thorlabs, Inc., C330TME-B and C240TME-B model lenses.

In addition, ray tracing technique was used to find the path of photons through the optical system. Figure 3.2 shows an exemplar ray tracing of 100 photons through a optical system consisting of C330TME-B and C240TME-B lens models. In this figure, a light source is situated on the left, then there is a C330TME-B collimating lens and also a C240TME-B focusing lens.

3.1.4 Backscattering Distribution

It is necessary for the MC simulation to know about the back-scattering behavior of the photons hitting targets. Considering accurate pattern of back-scattering is critical to acquire the best numerical results. We can categorized the targets that we had in this work into two main groups of large solid surfaces and small particles (scatterers). Large solid surfaces can also be divided into smooth (mirror-like) and rough surfaces. Back-scattering pattern of smooth surfaces is governed by specular reflection law, where the angle of incidence is equal to the angle of reflection. On the other hand, back-scattering pattern of ideal rough surfaces is governed by Lambertian law. Rough surface is considered with respect to the wavelength of the incident beam and if the depth of roughness is larger than the beam wavelength, surface is considered to be rough. Reflection from an ideal rough surface is called diffuse reflection and as it is mentioned before, this reflection has a Lambertian reflectance property. If we plot the probability density function of the photons scattered from an ideal diffusive surface, it has a $\cos(\alpha)$ form, while α is the angle between the back scattered photon and normal to the surface.

However, in most cases, backscattering pattern from rough surfaces is not an ideal Lambertian reflection. In theses cases, enhanced backscattering have been reported both experimentally [63] and theoretically [64]. The probability density function of the backscattering pattern of a rough surface showing enhanced backscattering behavior is a strong Gaussian form on top of the normal Lambertian shape with an orientation along

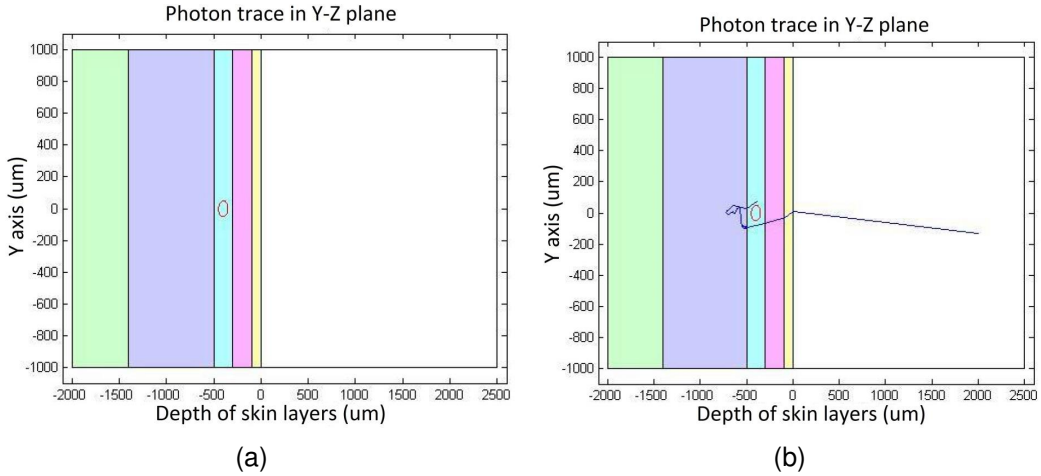

FIGURE 3.3: (a) Structure of a 5-layer skin model with epidermis, dermis and subcutaneous layers and one blood vessel. (b) Trace of one photon emitting from the lens into the skin layers. The photon penetrates four layers and undergoes lots of scattering, being absorbed in the third layer.

the beam axes. It means that a large number of photons will be reflected back exactly along the lasing axes of the incident beam. We conducted an experiment to measure the shape of the backscattering profile of the beam incident upon a rough aluminum disk, as discussed in paper B, and shown in Fig. 4.7.

Moreover, in cases of backscattering of photons from small static scatterers, we considered Henyey–Greenstein phase function [65] with an anisotropy factor of 0.85, and in cases of dynamic scatterers such as red blood cells, we considered a Gegenbauer kernel phase function [66]. Phase functions are mathematical functions which resemble the angular dependence of light scattering by small particles.

3.1.5 Multi-layer Skin Model

One of the main numerical models that we developed in this work was a multi-layer skin model. We first studied the biology (structure and optical properties) of human skin. Then we model the geometry of skin and defined spacial optical properties that governed the interaction od photons. Then photons were launched toward the structure in a Gaussian beam with a hyperbolic nature. Some of the photons would make their ways into the tissue model and interact with the scatterers and absorbers in the media. As a results of these interactions, photons accumulated information about skin layers within themselves. A portion of the photons made their way back from the skin tissue model (exited from skin model) and pass through the optical system and was detected by the system. Then,

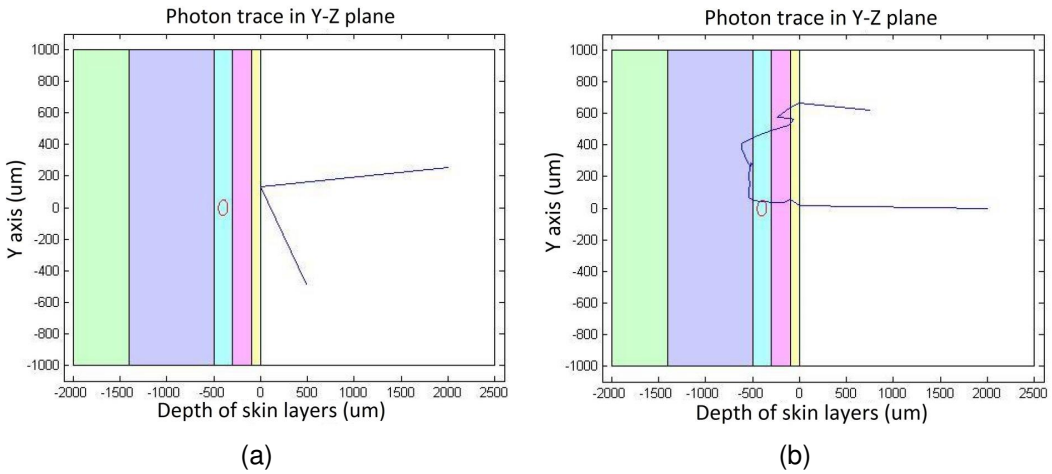

(a) (b)

FIGURE 3.4: (a) Trace of one photon which is reflected upon hitting the surface of the skin. (b) Trace of a single photon entering four layers and exiting the skin.

different aspects of the photons were analyzed and numerical signals were formed. Plots of the photon traces emitting from the laser and interacting with a 5-layer skin model are shown through Figs. 3.3 – 3.5. Third layer of the model contains a blood vessel. Further explanation is included in the captions of the figures.

3.2 Vertical Cavity Surface Emitting Laser

Vertical cavity surface emitting lasers (VCSELs) are a relatively recent type of semiconductor laser. VCSELs were first presented in the late 1970's. Subsequently, within the first years of commercial availability, VCSELs became the technology of choice for local area networks, effectively displacing edge-emitter lasers [67]. The typical layout of a VCSEL is shown in Fig. 3.6.

The resonant cavity containing the active layers is surrounded by electrically conductive layer stacks that form the laser mirrors which provide optical feedback. VCSELs designed for emission wavelengths in the 850 to 980 nm spectral range require $\sim$8 µm of epitaxially grown material, whereas the active region is composed of just a few quantum wells with $\sim$10 nm thickness. Metal organic chemical vapor deposition or molecular beam epitaxy are preferred for crystal growth. In the most simple device layouts, electric current is injected from ohmic contacts on the top epitaxial side and the backside of the substrate. Several methods have been successfully employed to achieve current confinement to a predefined active area. Among those are simple mesa etching of the top mirror, ion implantation to create highly resistive semiconductor regions, or selective lateral oxidation

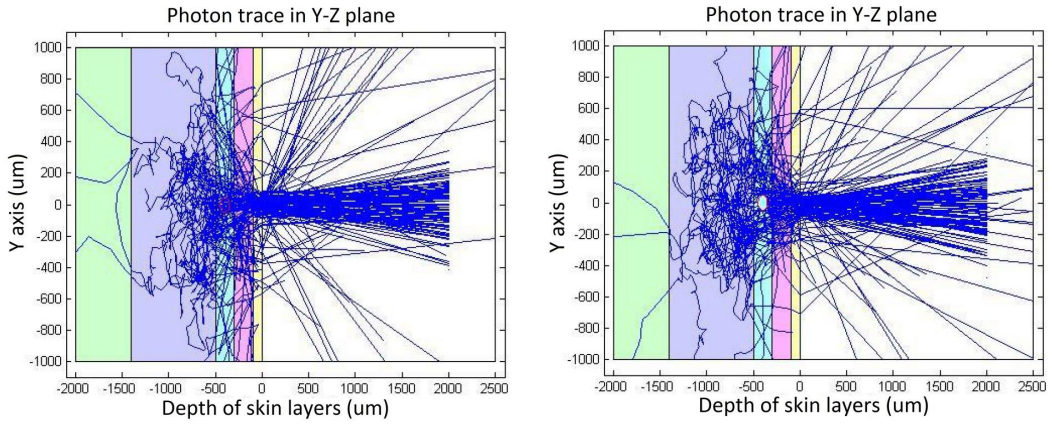

(a) (b)

FIGURE 3.5: (a) Trace of a hundred photons. Many enter the skin and blood vessel and after hitting the scatterers, if returned to the lens, will be detected and will contain information about the blood perfusion and skins optical properties as well. (b) The same configuration but with a high refractive index of the blood vessel, so that the photons are reflected from the blood vessel's wall (to show the effect that controlling optical properties can have on the path of photons).

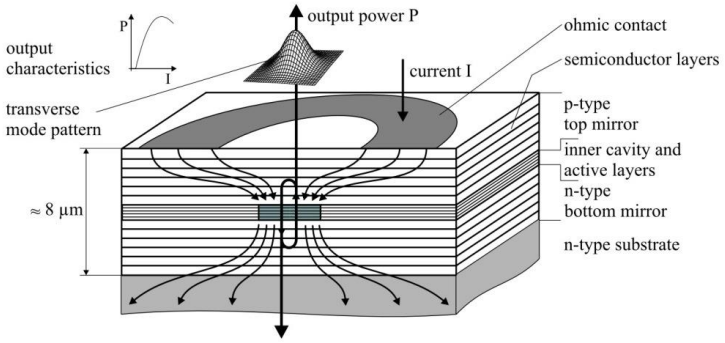

FIGURE 3.6: Typical layout of a VCSEL [68].

of a ∼10 nm thick semiconductor layer [69]. Because of its suitable properties, we use 850 nm single and multiple channel VCSELs in this project as the device to create the laser beam for use in the LFI systems.

3.3 Laser Feedback Interferometry

The self-mixing effect is observed when a laser illuminates an external target such that part of the light backscattered by the target reenters the laser diode's cavity, as illustrated in Fig. 3.7. The backscattered light interferes with the standing wave pattern inside the laser cavity, thus changing the emitted optical lasing frequency and power. In particular,

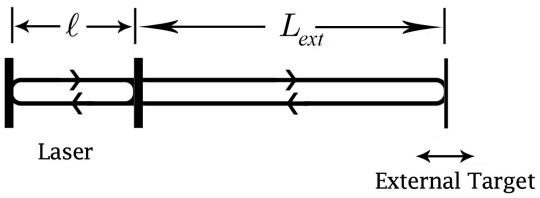

FIGURE 3.7: Self-mixing interferometry schematic [9].

the frequency of the free running laser shifts in order to maintain a modified phase condition for the new situation. Changes in external cavity or target equivalent to the movement of the external target by half of the emitted wavelength thus result in a full cycle in emitted optical power. The target's displacement then follows by counting the number of cycles in the emitted optical power [10, 70–73]. The fluctuations in optical power over time as a result of target motion can be measured by the laser diode's internal monitor photo detector or the laser diode junction voltage. The shift in the frequency of the free running laser has to satisfy the following modified phase equation (at timescales far slower than that of the internal laser dynamics) [74]:

$$0 = 2\pi\tau_{\text{ext}}(\nu - \nu_0) + C\sin(2\pi\nu\tau_{\text{ext}} + \arctan\alpha)\,, \tag{3.1}$$

where τ_{ext} is the external round-trip time, ν is the frequency of the laser with optical feedback, ν_0 is the frequency of the free running laser in the absence of the external target, C is the feedback parameter which depends on the level of optical feedback [75], and α is the linewidth enhancement factor [76]. The equation for the feedback parameter C is as follows [74]:

$$C = \frac{\tau_{\text{ext}}}{\tau_\ell}\,\kappa_{\text{ext}}\,\sqrt{1+\alpha^2}\,, \tag{3.2}$$

where τ_ℓ is the intra-cavity round-trip time, and κ_{ext} is the coupling coefficient which is a function of reflectivity of the target and exit laser mirror as follows [74]:

$$\kappa_{\text{ext}} = \varepsilon\,\sqrt{\frac{R_{\text{ext}}}{R_s}}\,(1-R_s)\,, \tag{3.3}$$

where ε is the fraction of the reflected beam which coherently coupled back into the lasing mode [75], and R_{ext} and R_s are the reflectivities of the target and exit laser mirror, respectively. By defining the external round-trip phase in the presence of the target as $\phi = 2\pi\nu\tau_{\text{ext}}$ and external round-trip phase in the absence of the target as $\phi_0 = 2\pi\nu_0\tau_{\text{ext}}$,

Eq. (3.1) can be written in the following form [74]:

$$0 = \phi - \phi_0 + C\sin(\phi + \arctan\alpha)\,. \tag{3.4}$$

Solving Eq. (3.4) for ϕ is not trivial as there is no closed-form solution for it. After solving this equation numerically, perturbation in the threshold gain of the laser due to the optical feedback can be formulated as [74]:

$$\Delta g_{\rm th} = -\frac{\kappa_{\rm ext}}{L}\cos(\phi)\,, \tag{3.5}$$

where L is the target distance from the laser. The variations in $g_{\rm th}$ can then cause an observable fluctuation in the laser optical power which is caused by the changes in the external round-trip phase in the presence of a target, as:

$$\Delta P = \beta\cos(\phi)\,, \tag{3.6}$$

where β is the amplitude of self-mixing signal which is dependent on the laser and system parameters (such as the amount of light being coupled back into the laser cavity, the distance to the target, and the photon lifetime in the laser cavity). The characteristics of the external target can then be sensed by monitoring the changes in the optical output power of the laser or changes in the terminal voltage of the laser [77]. LFI can also be used to measure the particle size and speed of flow [78]. The particle sizing has been demonstrated for the polystyrene and fat particles in the water in the range of 0.02 to 0.20 µm [78]. LFI flowmetry can be performed for flow or micro-fluidic [79] channels with different diameters and flow rates. Further potential applications of this technique include blood flow measurement in medicine [80] and parallel readout of flow channels [81]. Self-mixing velocimetry has been developed using a semiconductor laser diode [82]. LFI is also used in angular velocity measurements [83] and refractive index measurements [84]. Therefore, due to the non-expensive, compact, reliable, safe, easy to align, sensitive, and non-invasive characteristics of the technique, we employed LFI as the main sensing method to be used in this thesis.

3.4 Agar Skin Tissue Phantom

In the past few decades, there has been an increasing interest in using optical techniques in biomedical applications, whether for diagnostic or treatment purposes. The main reason for this growing interest is the non-invasive essence of these techniques, as well as their suitability for providing high resolution images. However, there are lots of problems in characterizing these optical techniques using real biological tissues. Therefore, most research groups in these areas are interested in using tissue phantoms to evaluate their systems and test their hypotheses. Among a wide range of techniques, I used agar based phantoms to make skin tissue models and milk or Intralipid as a blood phantom.

Agar is a hydrophilic gel, made of a kind of algae. Agar based phantoms are easy to make (using conventional lab equipment), low-cost, biologically compatible (safe to manipulate), and homogeneous. One drawback is that the phantom is not stable and shrinks in size (loses water) if not sealed or enclosed properly.

Although the main scientific usage of it is to provide solid substrate to culture microorganism, it can also be used to make tissue phantoms. For this purpose we need to mix it with scatterers and absorbers to control its optical properties. The main scatterer and absorber agents that I used were titanium dioxide as scatterer and India ink as absorber. We can make agar gels in thin layers and stack them on each other to make phantoms of multilayer tissues, such as skin. In the rest of this appendix, I will explain the process of making an agar tissue phantom and technical considerations to get the most realistic results, and also present our preliminary results on silicone based tissue phantoms.

3.4.1 Materials

Agar powder used in most of the experiments in this thesis was obtained from Sigma-Aldrich. The container of the agar is shown in Fig. 3.8 (a). Agar power can also be obtained from grocery stores but it is less pure. Agar gel was prepared by dissolving agar powder in water. It is better to use deionized or distilled water, whereas tap water can also be used. After adding agar powder to water, we need to heat up the mixture to initiate the polymerization process. It should be heated to boiling point to get the best result and a bit of stirring is also recommended. In most cases, we used a hot plate [Fig. 3.8 (b)] for heating purposes, while a microwave oven was also used in a few instances. The mixture should look clear when the agar powder is completely dissolved in the water, and it is the time to pour it in a curing container.

The weight proportion of the agar power and water should be chosen based on the

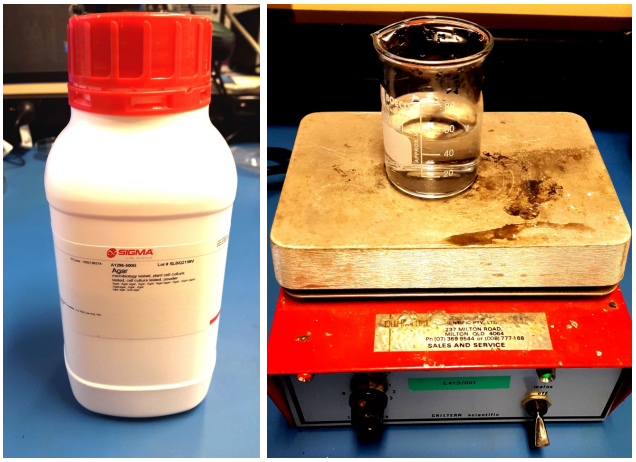

(a) (b)

FIGURE 3.8: (a) Agar powder for research use and (b) hot plate to heat up the mixture.

kind of gel which we require. For most of the experiments in this thesis 1 to 1.5 percent weight to weight proportions of agar to water were used. Higher percentage of agar will result in a firmer gel, but the percentage should not be too high, as the gel will become too thick. We used a 0.01 gram precision scale to weigh the agar powder. Figure 3.9 shows the scale that we used to weigh the agar powder.

3.4.2 Making Agar Layers

We need to make gels in different shapes to make different kinds of tissue phantoms. In the case of skin tissue phantom, we should make layers of agar resembling different layers of skin, such as epidermis, dermis, and subcutaneous layers. One way to make layers of agar gel is to use two microscope slides and spacers between them. The thickness of the spacers determines the thickness of the agar layers. Figures 3.10 (a) and (b) show how thick and thin spacers can be used between microscope slides, respectively. Nuts and pieces of aluminum sticking tapes were used to create thick and thin agar gel layers, respectively. Throughout this work, layers of agar with thicknesses in the range of 0.33 to 3.15 mm have been made and utilized. After pouring the gel in the Petri dish, it should be left for about 20 minutes in the room temperature to set, and then in a fridge for about one more day to get its final firm state.

FIGURE 3.9: The 0.01 gr precision scale used to weigh agar powder.

3.4.3 Optical Properties of Agar

We estimated the optical properties of agar gel using Beer–Lambert law. Based on this law, the total attenuation of optical power traveling in a transparent material such as agar gel, depends on its optical properties, and can be described as:

$$\mu_t = -\frac{1}{L} \ln \frac{P}{P_0} \,, \tag{3.7}$$

where μ_t is the total attenuation of the light, L is the agar sample thickness, P is the power of the transmitted light, and P_0 is the power of the non-attenuated light. The total attenuation can also be formulated as:

$$\mu_t = \mu_{a_{\mathrm{sam}}} + \mu_{s_{\mathrm{sam}}} \,, \tag{3.8}$$

where $\mu_{a_{\mathrm{sam}}}$ and $\mu_{s_{\mathrm{sam}}}$ are the absorption and scattering coefficients of the sample, respectively. More details about this technique can be found in the sec. 3 of paper F.

We used a 3.15 mm thick agar gel layer for this purpose. A collimated laser beam from an 850 nm VCSEL was illuminated through the layer and optical power was measured before and after the layer. P_0 and P were 710 and 576 µW, respectively, and ambient light noise level in the experiment was 0.5 µW, when the concentration of agar in water is about 1% w/w. Total attenuation is calculated to be 66.35 m^{-1} for this layer. In order to divide total attenuation coefficient into scattering and absorption coefficients, we need

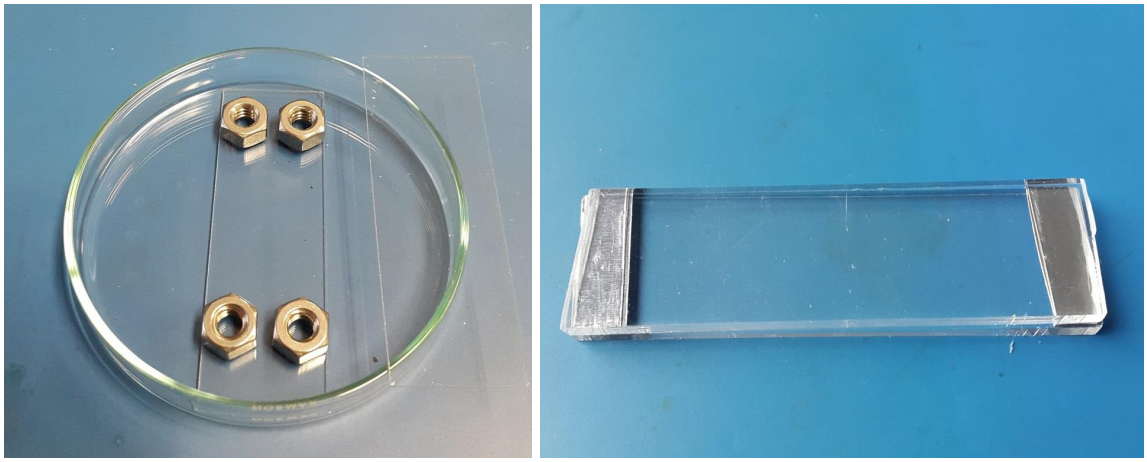

(a) (b)

FIGURE 3.10: (a) Using nuts as spacers to make thicker agar gel layers and (b) Using aluminum sticking tapes as spacers to make thiner agar gel layers.

to know one of these coefficients. Therefore we assumed the absorption of this gel is equal to water absorption at 850 nm (0.5 m^{-1}), which resulted in a scattering coefficient of 65.85 m^{-1} for this layer. Note that these numbers can be mentioned for pure agar powder (instead of agar gel). This means if the agar gel is a 1% weight to weight (w/w) gel, the figures for pure agar powder are obtained by multiplying the numbers by 100. In this way, we will apply these results to other layers, made of different percentages of the same kind of agar.

3.4.4 Titanium Dioxide as Scatterer

Both scattering and absorption coefficients of agar gel (or any other kinds of base tissue phantom material) are much lower than the corresponding optical properties of a typical biological tissue. Therefore, we need to add additional materials to the base gel to control its optical properties. One of the most common scattering materials is titanium dioxide (TiO_2), as it is low-cost, easy to obtain, and the size of the particles are in the range of a few hundreds of nm, which make it a good substitute for biological scatterers. TiO_2 resides in suspension in an agar gel mixture and will be fixed when the gel is set. Figures 3.11 and 3.12 show a microscopic image of TiO_2 particles in agar gel and the container of the TiO_2 we used during this thesis.

Using Beer–Lambert law, explained in sec. 3.4.3, I measured the scattering coefficient of TiO_2 powder which was about 380000 m^{-1}. We need to mix desired w/w proportions of TiO_2 powder in agar gel to achieve desired scattering coefficients.

FIGURE 3.11: Titanium dioxide particles in agar gel.

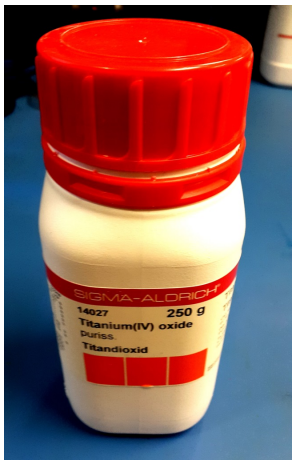

FIGURE 3.12: Container of titanium dioxide used in this work.

3.4.5 India Ink as an Absorber

India ink is mainly composed of carbon particles that have a relative flat absorption spectrum over the visible and near infrared frequency ranges [85]. It has been used as an absorber in tissue phantoms and its optical properties are well studied [86]. Because of its ease of use, availability, and absorption properties that mimics that of biological tissues closely, it is one of the most common absorber agent which has been used in making tissue phantoms to be used in optical imaging applications. Therefore, I mostly chose India ink in making agar tissue phantoms during this work. I measured the absorption coefficient of India ink in the lab using the Beer–Lambert law technique, which is explained in 3.4.3, and it was approximately $290000\mathrm{m}^{-1}$. Considering such a large absorption properties, often a tiny amount of India ink is enough in tissue phantoms to produce the absorption coefficients in the range of real biological tissues. In order to

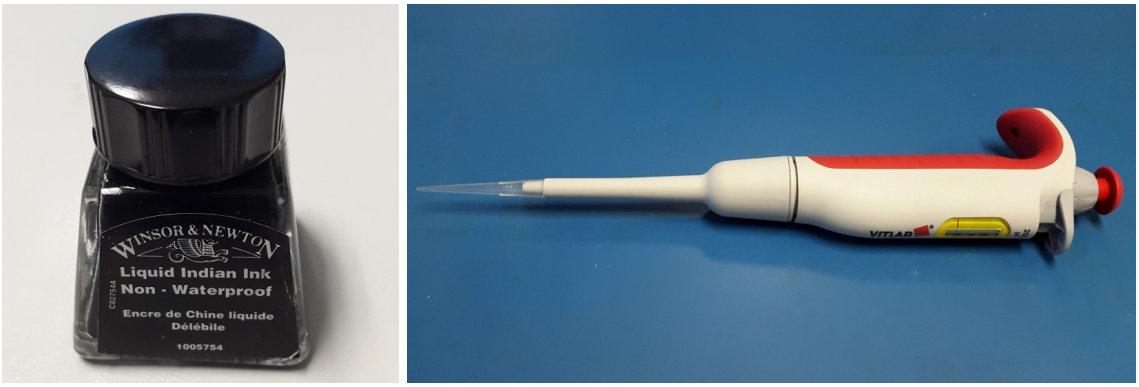

(a) (b)

FIGURE 3.13: (a) India ink and (b) micropipette used in this project.

measure the volume of India ink, I used a micropipette which had a precision level down to about 5 µL. Figure 3.13 (a) and (b) show the container of India ink and the micropipette that I used during my experiments, respectively.

3.4.6 Homogeneous Phantom

One of the challenges in making an agar or any other kind of tissue phantom is to add scatterer and absorber particles to the base gel in a homogeneous way. This means to have a spatially homogeneous scattering and absorption coefficient, we should make sure that scatterer and absorber particles are equally spread into the gel volume. Although it is easy to homogeneously mix some kind of particles, specially the ones which are in a liquid phase or emulsion suspension such as India ink pigments, in case of particles such as TiO_2 powder it can be quite difficult [85]. Because TiO_2 consist of clumpy powder that precipitate quickly when the base gel is not set, as it is a metallic oxide and heavier that the liquid base gel. During this work, I acquired two strategies to make homogeneous agar gels, containing TiO_2. First was to use a cordless drill and a whisk as a mechanical stirrer, as shown in fig. 3.14 (a). I found that 20 to 30 minutes of stirring of agar gel containing TiO_2, when it is kept hot at temperatures of about 80 degrees Celsius, resulted in a high level of homogeneity. Second strategy was to use a magnetic stirrer hotplate. Magnetic stirrer hotplate is a temperature-controlled hotplate that has a rotating magnetic disk under the plate at the same time. Magnetic bar should be placed in the liquid containing TiO_2 and it should be left to stir it for at least one hour. When the mixture is ready, it should be pour in a Petri dish that contain the microscope slides and spacers (if we want to make layers) before TiO_2 particles start to precipitate out of the suspension.

(a) (b)

FIGURE 3.14: (a) Drill and whisk as mechanical stirrer and (b) magnetic stirrer hotplate and a container containing a magnetic bar in it.

3.4.7 Cancerous Skin Tissue Phantom

One of the phantoms that I made and used in my experiments was a 3-layer agar cancerous skin tissue phantom. Three layers in this phantom represent the three main layers of human skin. epidermis, dermis and subcutis layers. Thickness of these layers varies greatly in different locations of the human skin, but approximate thickness of 100, 400, and 1000 µm can be considered for epidermis, dermis, and subcutis, respectively. As it is difficult to make 100 µm agar gel layers, I made layers with thicknesses of about 330, 330, and 1100 µm as epidermis, dermis, and subcutis layers in the 3-layer agar gel skin tissue phantom. Optical properties of human skin tissue has been studied extensively in visible and near infrared spectra [87, 88]. We need to add proper amounts of India ink and TiO_2 to the layers to create optical properties similar to those of human skin tissue measured in the literature. These amounts were chosen based on the optical properties which was measured in sections 3.4.5 and 3.4.4. In most cases, non-melanoma skin cancer cases a drop in optical properties of the afflicted tissue. For example, the scattering and absorption coefficients of nodular basal cell carcinoma and squamous cell carcinoma reduce by factors of about 0.6, with respect to the normal surrounding dermis tissue, at the wavelength of 850 nm [11]. Therefore, we included a 4 mm cylindrical area in the second layer (dermis), with reduced optical properties by factors of 0.6 for both absorption and scattering coefficient, as a model of cancerous tissue in our agar cancerous skin tissue phantom. Figure 3.15 (a) shows how layers are stock on each other and Fig. 3.15 (b) shows the top view of the mounted tissue phantom. To stop agar from evaporation a 150 µm cover slip was placed on the top of the layers and the whole tissue phantom was wrapped in a piece of plastic from below. A biopsy punch was used to make a whole in

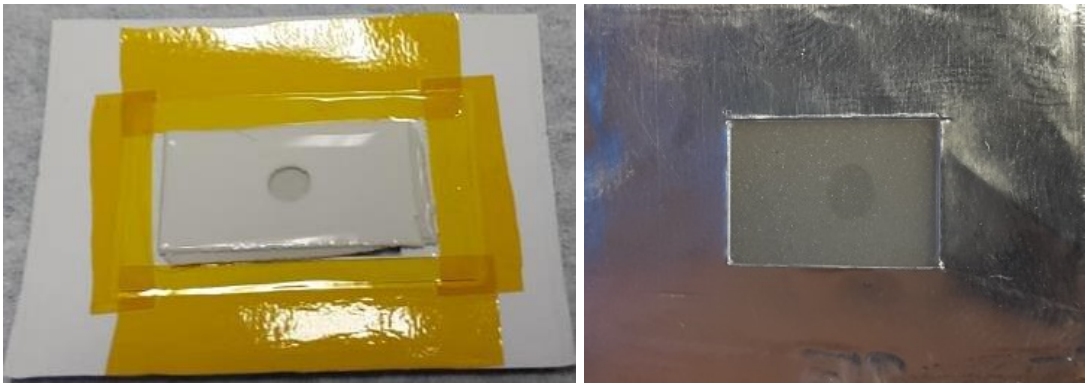

(a) (b)

FIGURE 3.15: (a) Multi-layer agar cancerous skin tissue phantom (the two first layers of epidermis and dermis including a 4 mm whole for the cancerous model to be added) and (b) top view of the mounted cancerous skin tissue phantom.

the second layer and detached the cancerous cylindrical area to be placed in the whole.

3.4.8 Micro Tubes

One of the limitations of agar tissue phantoms is that it is hard to make hollow channels inside them. Therefore, I used capillary tubes and embedded them in the agar gel based phantoms to model blood vessels. Two types of capillary tubes were used during this project. First, circular capillary tubes. It has a outer and inner diameters of about 1.6 and 1.2 mm, respectively. The length of this tube is 5 cm. Second type was a rectangular capillary tube. The walls of this tube is 300 µm thick. The dimensions of the interior channel are 0.3 and 3 mm. Figure 3.16 (a) shows circular and rectangular capillary tubes, used in this project. I embedded these kinds of tubes inside agar tissue phantoms at different depths and in different structures. I used a syringe pump to flow liquids through these channels. Figure 3.16 (b) shows the syringe pump which was used in this project. Pump rates between 20 to 2000 µL per minute were used to do different experiments in this project.

3.4.9 Milk and Intralipid

I used two types of blood phantom and push them through capillary tubes included in different tissue phantoms in this project. These blood phantoms were homogenized milk and Intralipid 20 $\%$ which were diluted with ionized water with different ratios to provide the desired optical properties. Homogenized milk has been used frequently as a blood

(a) (b)

FIGURE 3.16: (a) Circular and rectangular capillary tubes used to model blood vessels and (b) syringe pump to push liquid (blood phantom) through these channels.

phantom in modeling biological tissues as its fat particles mimic red blood cells in size and optical properties [85]. Homogenized milk has high scattering and low absorption coefficients in the near-infrared range which are close to those of blood. Intralipid optical properties is also well-studied in the literature and it has also been used frequently as blood phantom [89]. Figures 3.17 (a) and (b) show images of the container of the homogenized milk and Intralipid which were used in this project.

3.4.10 More Stable Phantoms

One of the problems with agar gel tissue phantoms is that they are not stable over time. If left in open air, they will lose water and shrink in size. Furthermore, if store outside fridge, they are highly susceptible to fungal growth. Moreover, under tension, the gel matrix will break easily, therefore it is hard to create thin layers or hollow channels in them. As a stable alternative, we developed the technology to make silicon-based tissue phantoms. We used two part polydimethylsiloxane (PDMS), which is the most common silicon-based organic polymer. Figures 3.18 (a) shows the two parts of the PDMS that we used to make these phantoms. One part of curing agent should be added to ten parts of the main silicon part and the mixture should be left at least for two days to set. The same strategies to mix Particles in a homogeneous way should be applied. One problem with PDMS is the air bubbles which are trapped in the mixture while stirring. Air bubbles will stay in the mixture because it is viscous. To get rid of the air bubbles, we used a vacuum chamber. About two hours of vacuuming showed good results. The other technical consideration was to use perspex in order to make layers, as PDMS detached easily from this kind of material while it is hard to separate it from glass when it is set. Figures 3.18 (b) shows a 100 µm PDMS layer containing TiO_2 and India ink, resembling an epidermis layer.

(a) (b)

FIGURE 3.17: (a) Homogenized and (b) Intralipid 20 % used as blood phantom in the experiments.

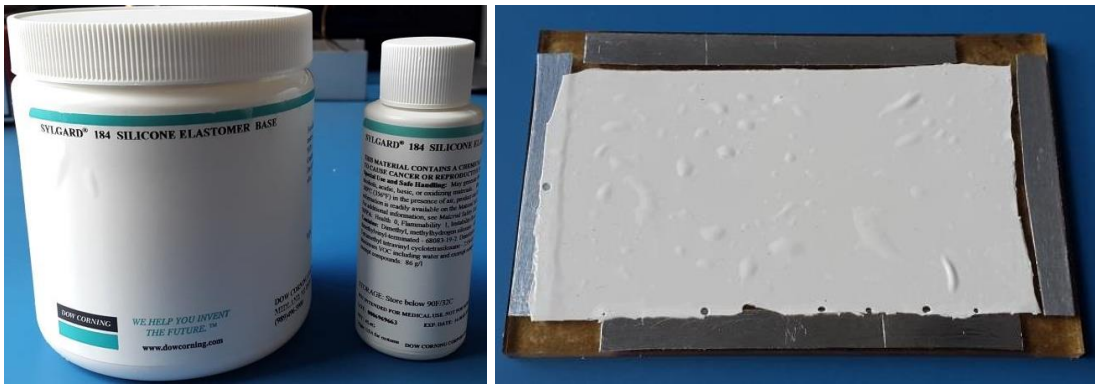

(a) (b)

FIGURE 3.18: (a) Two part PDMS (silicon-based gel) and (b) 100 micron thick layer containing TiO_2.

Chapter 4

4. Modeling for Skin Cancer Detection

This chapter includes papers A, B, and C. Paper A investigates the reflection profile of laser beam from a rough surface (the effect of enhanced backscattering along the lasing axis) experimentally, and incorporates these results into a Monte Carlo model to study the effects of numerical aperture of the beam on the laser Doppler velocimetry signal. This study has interesting conclusions such as the improvement of SNR of the Doppler spectrum as the numerical aperture of the beam increases. Paper B investigates the effects of the optical system on the morphology of the Doppler spectrum in a larger scale. The Doppler spectrum obtained from LFI signal is complex in morphology and its features are strongly related to system design. This study discuss the design features of LFI systems on the Doppler spectrum. There are a large number of the parameters that will dictate the Doppler spectrum characteristics like full width at half maximum, signal to noise ratio, and Doppler frequency of the signal. Major and minor contributors to the Doppler spectrum characteristics are investigated by sweeping different parameters and monitoring the results. Although the studies in both paper A and B have been carried out on simple systems such as velocimetry of a rotating disk target, it can be considered as a stepping-stone for all the future work in the thesis. That is because these papers inspect the fundamental science behind an LFI system by closely looking at numerous effects and phenomena such as the stochastic and deterministic photon trajectory patterns and backscattering profiles, laser characteristics such as aperture size, beam profile, polarization and the number of modes, stability, beam Gaussianity, lens diffraction, numerical aperture of the optical system and the lasing beam, the velocity and direction of the scatterers in relation to the photon's directions, spatial position and surface structure and size of the target or scatterers, system mechanical vibration, and the other sources of noise and imperfection such as any kind of unwanted wobbling, and the other contributors to the

signal. Finally, we have a tool to anticipate the Doppler and reflectance spectra acquired from complex structures.

This tool was then used in paper C to demonstrate the application of LFI in skin cancer detection. Doppler blood perfusion modality was applied to a cancerous skin model and discussion was made about the characteristics of this imaging system. Paper C presents a numerical study of a laser Doppler perfusion imaging system by means of an LFI system.

4.1 Paper A

Mowla, Alireza and Nikolić, Milan and Lim, Yah Leng and Bertling, Karl and Taimre, Thomas and Rakić, Aleksandar D, "Effect of the optical numerical aperture on the Doppler spectrum in laser Doppler velocimetry," IEEE, COMMAD, 72–74 (2014).

4.1.1 Abstract

We have investigated the effect of the optical system design on the characteristics of the Doppler spectrum of a laser Doppler velocimeter, by means of a Monte Carlo simulation model. We show that numerical aperture is one of the parameters that strongly affect the full width at half maximum and signal to noise ratio of the Doppler spectrum. The profile and intensity of the enhanced backscattering of the laser beam from a diffusive rough aluminum disk surface is measured using a range of lenses with different focal lengths and the results are incorporated into the Monte Carlo model.

4.1.2 Introduction

The Doppler spectrum obtained from the Doppler shift in the frequency of the laser beam incident upon moving solid objects or scatterers in fluid flows, has been used from the early days of lasers for sensing purposes [90–92]. including velocimetry, flowmetry, and biomedical applications [82, 93, 94]. Laser feedback interferometry (LFI) which is a simple and self-aligned technique is an implementation of laser Doppler velocimetry (LDV) [82]. Optical numerical aperture (NA) of the beam which is dictated by the lens configuration, is one of the parameters that can affect the shape of the Doppler spectrum. Study of the morphology of the Doppler spectrum is important in dealing with more complicated systems. In this work Monte Carlo (MC) simulation [60] is used to model a rotating disk LDV system with a LFI implementation. A reliable numerical model gives us a tool to investigate the sensitivity of the spectrum characteristics on the optical system parameters. To make a realistic model, all the parameters, variables and features of the LDV system should be embedded into the simulation based on physically realistic and measured quantities. The profile and intensity level of the enhanced backscattering [95] of the laser beam from the diffusive disk surface was measured using four lenses with focal lengths from 3.10 to 15.29 mm and the results are incorporated into the simulation.

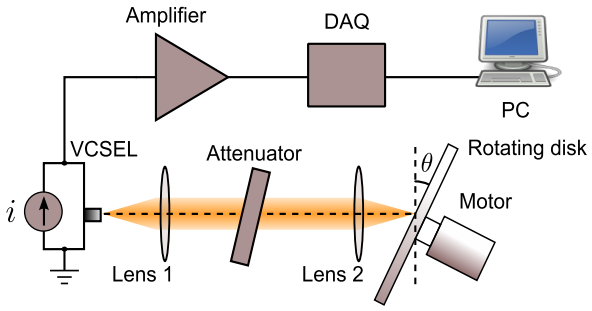

FIGURE 4.1: Block diagram of rotating disk laser Doppler velocimetry apparatus based on laser feedback interferometry.

Through simulation, Doppler spectra are obtained for four different lenses and the variations in signal to noise ratio (SNR) and full width at half maximum (FWHM) are studied. It was shown that increase in NA (equivalent to the decrease in focal length) results in the dramatic increase in SNR and FWHM. After explaining the model, we present a section on the measurement of the enhanced backscattering and then we include results and discussions and finally the conclusion.

4.1.3 Model

MC is a powerful and well-established method in studying the behavior of photons in an optical system [96]. MC looks at the stochastic movement of photons, emitted from a laser, in an optical system that may contain free space, lenses, other solid opaque or transparent components, biological tissues, scatterers in fluid, and moving objects. Photons are produced with a Gaussian spatial density profile with the beam divergence angle that matches the laser model. Physical laws will govern the system and affect the movement of the photons. Photons may undergo reflection, refraction, scattering, or absorption. Each one of the photons in the space has its own characteristics, such as position, direction, velocity, frequency, polarization, etc. The Doppler effect is a shift in the frequency that will happen when a photon impinges on a moving object or scatterer. In a LFI system, the laser acts as both transmitter and receiver. The part of the photon population that reenters the laser cavity will cause a modulation of the optical power of the laser [70–72]. A block diagram of the rotating disk LFI system is shown in Fig. 4.1. In this scheme, the photons that find their way back into the laser cavity are considered as detected photons. The frequency shift of the detected photons is extracted to construct the Doppler spectrum.

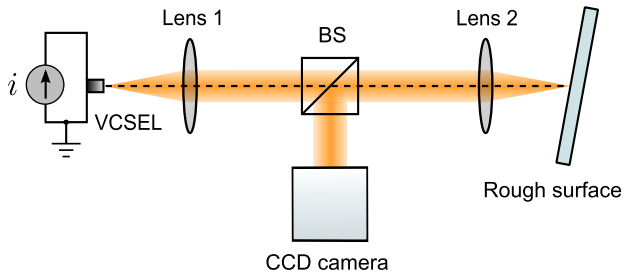

FIGURE 4.2: Block diagram of enhanced backscattering measurement apparatus.

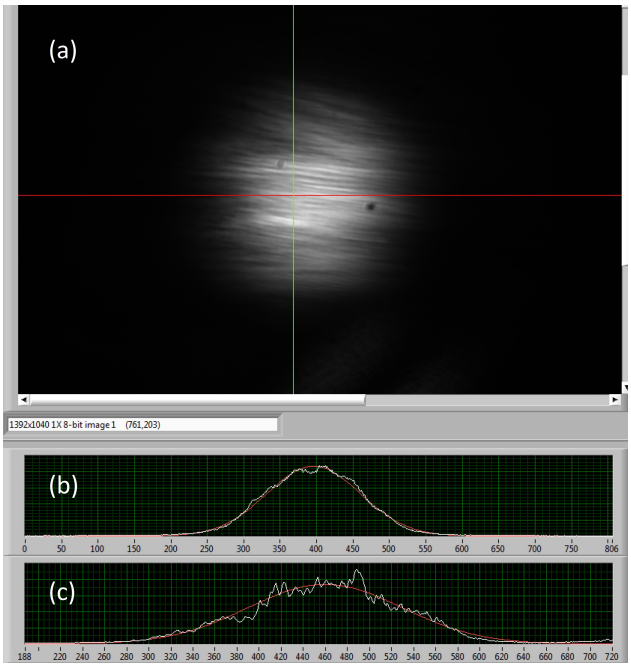

FIGURE 4.3: Image from CCD camera (a) to measure enhanced backscattering for a C240TME-B lens, including the horizontal (b) and vertical (c) intensity distribution.

4.1.4 Enhanced Backscattering Measurement

The backscattering distribution profile of the photons from a random rough surface, with a roughness greater than the wavelength of the beam, is one of the important parameters that should be embedded into the simulation to produce realistic Doppler spectra. For an ideal diffusive surface, the backscattering distribution is expected to be Lambertian [95], but experimentally for most rough surfaces we will have a Gaussian-like enhanced backscattering around the lasing axis superimposed on the Lambertian level [95]. We have measured the enhanced backscattering from the rough surface of an aluminum disk, using four different lenses. The block diagram of the apparatus used to measure

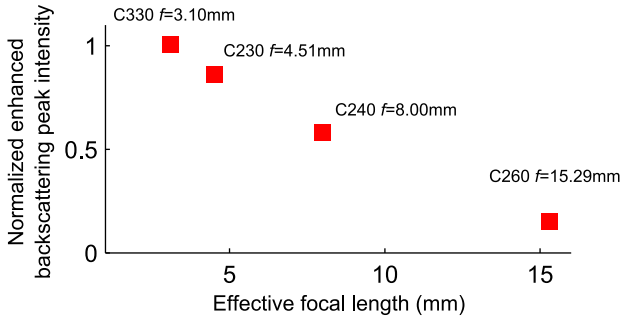

FIGURE 4.4: Normalized enhanced backscattering peak intensities for four different lenses C330TME-B, C230TME-B, C240TME-B, and C260TME-B, versus their focal lengths.

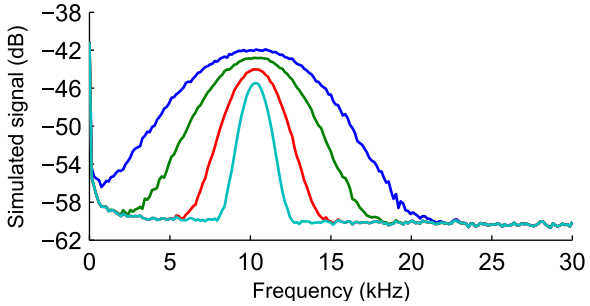

FIGURE 4.5: Simulated Doppler spectra varying beam NA. The beam NAs of the narrowest to widest signals are 0.06, 0.12, 0.22, and 0.32, corresponding to C260TME-B, C240TME-B, C230TME-B, and C330TME-B lenses, respectively.

the enhanced backscattering is shown in Fig. 4.2. VCSEL beam is collimated and focused on a rough disk using two lenses. Half of the backscattered beam, collected by the objective lens, is directed into a CCD camera using a beam splitter (BS). The CCD camera provides images that contain information about the distribution of the enhanced backscattering and the intensity level of its peak. The Thorlabs Inc. lenses C330TME-B, C230TME-B, C240TME-B, and C260TME-B with focal lengths of 3.10, 4.51, 8.00, and 15.29 mm, respectively, have been used to measure the level of the enhanced backscattering peaks at different focal lengths. One exemplar image from the CCD camera is presented in Fig. 4.3 (a) which shows the enhanced backscattering of the laser beam from a rotating rough aluminum disk, using C240TME-B as the objective lens. Figs. 4.3 (b) and (c) are the enhanced backscattering profiles along the horizontal and vertical axes, respectively. Figure 4.4 shows the normalized intensity level of the enhanced backscattering for different lenses, versus their focal lengths. As it is shown, the level of enhanced backscattering decreases significantly when the focal length is increased.

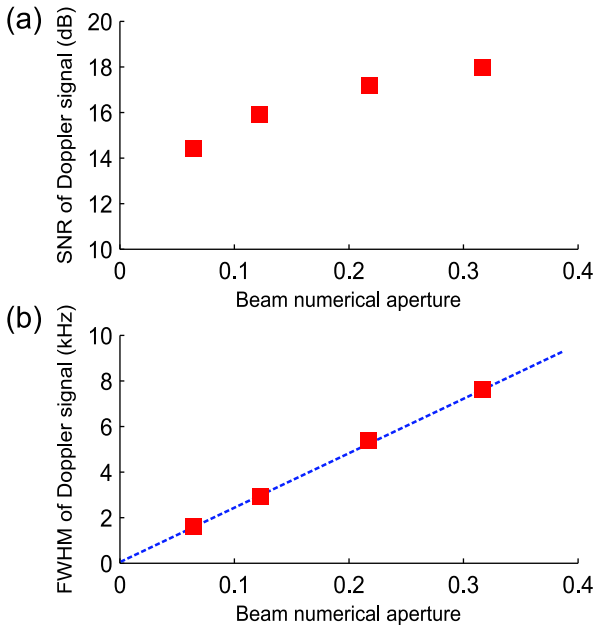

FIGURE 4.6: (a) SNR and (b) FWHM of the Doppler spectra versus beam NA.

4.1.5 Results and Discussion

We simulated a rotating disk LDV system with a LFI implementation. The model includes a collimated beam with $1/\mathrm{e}^2$ diameter of 1.96 mm emitted from a laser diode. Four different lenses C230TME-B, C240TME-B, C260TME-B, and C330TME-B, with focal lengths of 3.10, 4.51, 8.00, and 15.29 mm, respectively, were modeled to focus the collimated beam on a rough surface of an aluminum rotating disk. The disk model is rotating at the angular velocity of 0.79 rad/s and positioned at an angle of $15\,^\circ$ relative to the normal to the lasing axis. The $1/\mathrm{e}^2$ diameter of the enhanced backscattering beam is about 1.6 mm for all four lenses but with different intensity levels. The simulated Doppler spectra for optical beam NAs of 0.06, 0.12, 0.22, and 0.32, corresponding to C260TME-B, C240TME-B, C230TME-B, and C330TME-B lenses, respectively, is shown in Fig. 4.5. The SNR and FWHM were significantly affected when beam NA was varied. The trends of the SNR and FWHM are shown in Fig. 4.6. Both SNR and FWHM increased when beam NA increased.

4.1.6 Conclusion

The study of the morphology of the Doppler spectrum in the LDV system is of great importance when dealing with more complex, less predictable targets. There are many parameters and phenomena that will contribute to the signal characteristics. In this work, we have studied the effect of beam numerical aperture on the broadening and SNR of

the Doppler spectrum through the powerful simulation technique of Monte Carlo. The numerical engine developed here qualitatively reproduces the morphological features and trends observed in LFI Doppler spectra without any calibration. We experimentally measured the enhanced backscattering from the surface of a rough aluminum disk. Once these experimental backscattering profiles were incorporated into the model we obtained an experimentally calibrated numerical engine capable of producing highly reliable and accurate numerical experiments. We have shown that beam numerical aperture is a major influential parameter affecting the morphology of the Doppler spectrum. Increasing the optical numerical aperture by decreasing focal length, will increase SNR and FWHM of the Doppler spectra significantly.

4.2 Paper B

Mowla, Alireza and Nikolić, Milan and Taimre, Thomas and Tucker, John R and Lim, Yah Leng and Bertling, Karl and Rakić, Aleksandar D, "Effect of the optical system on the Doppler spectrum in laser-feedback interferometry," Appl. Opt. **54**, 18–26 (2015).

4.2.1 Abstract

We present a comprehensive analysis of factors influencing the morphology of the Doppler spectrum obtained from a laser feedback interferometer. We explore the effect of optical system parameters on three spectral characteristics: central Doppler frequency, broadening, and signal-to-noise ratio. We perform four sets of experiments and replicate the results using a Monte Carlo simulation calibrated to the backscattering profile of the target. We classify the optical system parameters as having a strong or weak influence on the Doppler spectrum. The calibrated Monte Carlo approach accurately reproduced experimental results, and allows one to investigate the detailed contribution of system parameters to the Doppler spectrum which are difficult to isolate in experiment.

4.2.2 Introduction

One of the earliest applications of the laser was to measure velocity using the laser Doppler spectrum [90, 91] which became a well established sensing technique for characterizing fluid flows and measuring the velocity of bodies in motion [51]. Laser feedback interferometry (LFI) is a well-established sensing technology that can be configured to operate on the same fundamental Doppler-shift principle as traditional laser Doppler velocimetry (LDV) systems [8]. An LFI velocimeter boasts quantum noise limited performance, simplicity of optical alignment and uses low cost semiconductor lasers. LFI has been used for biomedical applications [9] such as blood perfusion measurement [80, 97] and imaging of tissue phantoms [98] as well as for non-biomedical applications including fluid flowmetry [79, 81], velocimetry [72], refractive index [84], displacement, and absolute distance measurement [8]. An LFI velocimeter usually involves the analysis of a measured Doppler spectrum in order to infer information about the speed of the target. Therefore, understanding how different system parameters affect the morphology of the Doppler spectrum is of great interest. Modeling of the Doppler spectrum has been undertaken [51], however the impact of optical system parameters on the laser Doppler spectral

morphology is not well explored.

In this work we systematically investigate the effect of system parameters on the Doppler spectrum. In order to produce a stationary distribution of velocities that can be precisely controlled, we employ a diffusive rotating disk as a target. We investigate this system experimentally by means of LFI, and numerically via Monte Carlo (MC) simulation [60]. The system parameters we investigate are target velocity, beam spot position, target angle of inclination with respect to the laser beam axis, fractional change of velocity across the beam spot, beam numerical aperture (NA), system vibration, target surface profile, instability in target velocity, and laser linewidth. By accurately reproducing the experimental Doppler spectrum through MC simulation after calibration for the light scattering characteristics of the target, we are equipped with a powerful tool to predict and analyze the performance of LFI velocimeters.

4.2.3 Theory and methodology

Laser Feedback Velocimeter

The LFI velocimeter is a versatile laser sensing technique in which a portion of the Doppler-shifted light re-enters the laser cavity and mixes with the optical field within ("self-mixing"), modulating the laser's optical output intensity at the Doppler frequency. This modulation may be monitored using the power spectrum of the external photodiode current or laser junction voltage signal. The frequency shift due to target motion is the Doppler shift and is given by [51]:

$$\Delta f = \frac{1}{2\pi}(\mathbf{k}_s - \mathbf{k}_i) \cdot \mathbf{v}\,, \tag{4.1}$$

where Δf is the Doppler shift in the frequency of the light, $\mathbf{k}_s$ and $\mathbf{k}_i$ are the wave vectors of the scattered and incident waves, respectively, and $\mathbf{v}$ is the velocity vector of the target.

We used a rotating disk with a rough front surface (that is, the roughness was greater than the laser emission wavelength) to create a laboratory environment in which a stationary distribution of velocities can be produced in a precisely controllable manner. In practice, the Doppler spectrum of such a diffusive rotating disk has a Gaussian distribution profile centered at the frequency one would expect from (4.1) [99]. The width of this Gaussian is determined by a number of system parameters, which we investigate in section 4.2.4.

Laser speckle is a random intensity distribution observable when laser light is incident upon a diffusive surface [100, 101]. For a target that has roughness significantly greater

than the laser wavelength, as is our situation, the speckle statistics do not depend on the target characteristics. The speckle pattern can be modeled by spatial intensity distribution functions in the planes perpendicular to the diffusive surface (longitudinal speckle) and parallel to the diffusive surface (transverse speckle). For small longitudinal displacements, as is our case, speckle has no discernible effect on the measured spectrum [102]. Our target does have a component of velocity in the plane normal to the laser beam (and therefore detection) axis. Thus the transverse speckle pattern will change in time and therefore could have a discernible effect on the self-mixing signal we measure. However, the power spectrum in the frequency domain due to this time-varying speckle pattern is broadband and centered at 0 Hz [100]. The breadth of this dynamic speckle spectrum ensures that its spectral density amplitude is small in comparison to the relatively narrow-band fundamental Doppler peak, placing it below the typical noise floor of our apparatus. Indeed, an LFI system measuring fluid velocity (which is similar to our considerations in this article in many respects) has been modeled successfully considering only optical system parameters without any speckle effects [80]. Therefore on the basis of previous theoretical and experimental work, we take the effect of speckle to be small for our optical configuration, and explore in detail the effect of optical system parameters on the self-mixing signal.

In order to analyze the effect of system parameters on the Doppler spectrum, we characterize it by three quantities:

1. Central Doppler frequency (the frequency at the center of the Gaussian distribution).
2. Full width at half maximum (FWHM) of the Gaussian distribution.
3. Signal-to-noise ratio (SNR).

Because of physical characteristics of the system such as target velocity and beam NA, the FWHM is always non-zero [99]. Although this broadening can be viewed as reducing the accuracy of the system, it nevertheless contains information about the system/target characteristics. We define SNR here as the ratio of the peak power of the Gaussian distribution to the power of the noise floor measured in the absence of target motion. The noise floor depends on thermal, electrical, optical apparatus, and laser characteristics.

Experimental configuration and method

We used an 850 nm vertical-cavity surface-emitting laser (VCSEL) (Litrax Technology Co., Ltd.) with threshold and operating currents of 4 and 4.6 mA, respectively. The operating

current was chosen to have the highest possible SNR whilst maintaining stable operation by avoiding polarization switching [103]. The divergence half-angle of this laser was approximately 7°.

To collimate and focus the laser beam, a pair of lenses of focal length 8 mm, clear aperture of 8 mm, and NA of 0.5 were used (model C240TME-B, Thorlabs, Inc.). To avoid strong harmonic levels [104] we placed a 30 dB attenuator in the path of the collimated beam, giving a round-trip attenuation of 60 dB. The laser and lenses were mounted on a computer controlled, motorized translation stage to facilitate scanning. The laser beam was focused onto a diffusive rotating disk, which in turn was mounted on a servomotor with an attached encoder (FAULHABER GmbH & Co.). The servomotor was able to reliably produce angular velocities in the range from 0.14 to 2π rad/s. The disk and servomotor were mounted on a motorized rotational stage to accurately control optical angle of incidence. The VCSEL terminal voltage was amplified and then digitally sampled for post-processing on computer. The fast Fourier transform of the laser terminal voltage was averaged 16 times, with 2×10^4 samples and a 200 kHz sampling rate. A block diagram of the experimental setup is shown in Fig. 4.7. A typical Doppler spectrum obtained from this system will contain a fundamental Gaussian peak, where the frequency at the center of the peak (which we refer to simply as the Doppler frequency) corresponds to the velocity at the center of the laser spot on the target [99]. In addition, due to the non-linear effects of LFI [104], experimental spectra often display Gaussian harmonics, centered at multiples of the Doppler frequency.

We used a simple but effective procedure for extracting spectral characteristics from experimental data as follows: a Savitzky–Golay filter was applied to smooth the spectra, then the peak value was taken to correspond to the central Doppler frequency. The amplitude of the spectrum at this point was used to calculate SNR by comparing it to the amplitude of the spectrum at the same frequency point in the absence of target rotation. The FWHM was calculated by taking the point to the right of the Doppler frequency at which the spectral power decreased by 3 dB from its maximum and multiplying it by two, thereby avoiding potential difficulties which may arise with a simple Gaussian fit, for example if the Doppler peak was very close to 0 Hz. This method is fast, easy to use, and reliable to be used in this work.

As the simulated spectra were less noisy than the corresponding experimental spectra, and moreover were devoid of non-linear effects due to LFI, a simple Gaussian fit to the data was easy to use to extract relevant spectral simulated parameters.

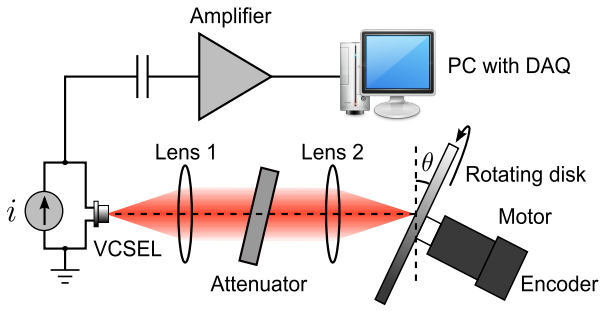

FIGURE 4.7: Block diagram of laser Doppler velocimetry apparatus.

Light scattering from a diffusive surface

The light scattering behaviour of our target needed to be known for the MC simulation. The roughness of the target was greater than the wavelength of the laser we were using, and whilst Lambertian scattering behaviour may be generally expected, cases of enhanced backscattering have been reported in experimental [63] and theoretical [64] studies. This enhanced backscattering was indeed what we experimentally observed using the apparatus shown in Fig. 4.8. By observing the intensity profile of the back-scattered beam on the CCD camera we were able to discern the strength of the enhanced backscattering relative to the strength of the Lambertian scattering. The target scattering behaviour in the MC simulation was calibrated using these experimental measurements. Although the enhanced backscattered beam does not completely maintain the polarization of the incident beam, the resulting LFI signal can be cast as a superposition of its transverse polarization states [105]. Also, regardless of the disk angle of inclination with respect to the lasing axis α (see Fig. 4.8), the peak of the enhanced backscattering distribution remains aligned with the lasing axis. As this scattering behaviour is target dependent, it is important to characterize and incorporate it into the MC simulation. However, the impact of optical system parameters on the Doppler spectrum investigated in subsequent sections, whilst calibrated to this target, are expected to hold more generally.

Monte Carlo method

MC methods are a broad class of simulation techniques, which have been successfully applied to problems in physics, engineering, finance, biology, medicine, and statistics [60]. They are especially applicable in the area of photon transport simulation in which one can replace the radiative transfer equation by more flexible MC methods [96]. We employed the standard MC practice of treating the laser beam as being comprised of a number of

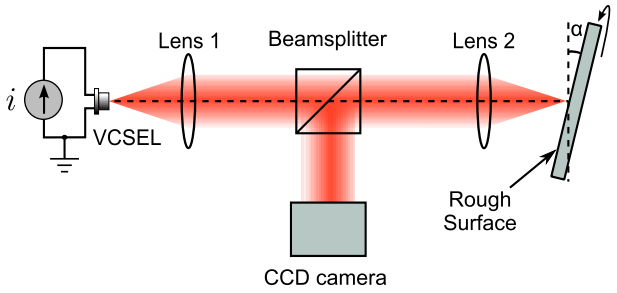

FIGURE 4.8: Block diagram of enhanced backscattering measurement apparatus.

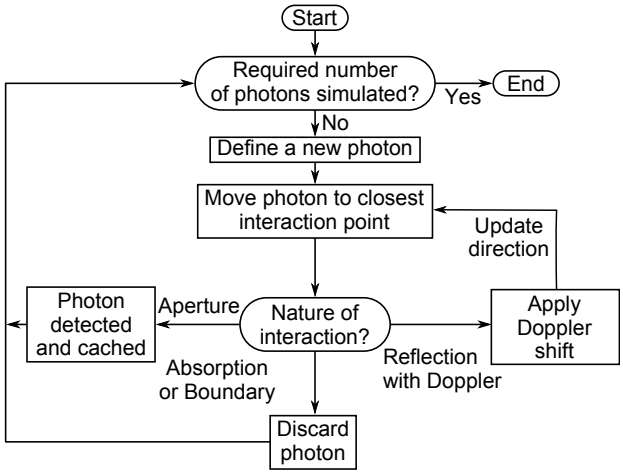

FIGURE 4.9: Flowchart of the MC photon transport simulation.

photons, each behaving as a standalone particle. Photons were launched from the lens closest to the target with a Gaussian spatial probability distribution governed by the size of the collimated beam incident upon the lens. The initial direction of each photon was assigned by considering its position relative to the center of the lens, as well as the NA and focal length of the lens, such that the spatial distribution of photons at the focal plane of the lens was Gaussian with a width governed by Gaussian beam optics [106].

The target scattering behaviour was modeled with a probability density function comprised of a Lambertian component and an enhanced (direct) backscattering component, the relative strengths of which were determined by the experimental measurements outlined in Sec. 4.2.3. Scattered photons were assigned a Doppler shift governed by Eq. (5.2), and those that returned to the focusing lens were considered to contribute to the Doppler spectrum. A flowchart of our MC model is shown in Fig. 4.9.

4.2.4 Results

In this section we present the experimental and simulated results of varying a number of optical system and target parameters. As there is a significant body of data, we dedicate a subsection to each of the parameters studied. We present the raw data here and leave discussion of overall implications for section 4.2.5.

Varying target angular velocity for fixed spot position

The angular velocity of the disk was varied by increasing the servomotor speed, thereby increasing the linear velocity at the measurement point. Measurements were performed at 11 different angular velocities from 0.22 to 5.56 rad/s. The focal length of the lens was 8 mm, the beam spot was located 20 mm above the disk center along the vertical axis, and the angle of incidence was $15\,^{\circ}$. The angular velocity was monitored by the motor encoder. The experimental and simulated Doppler spectra are shown in Fig. 4.10(a) and (b), respectively. As can be seen, the experimental and simulated results agree well. Fig. 4.11(a) and (b) show trends in the FWHM and SNR, while Doppler frequency, as expected, increases linearly with the disk angular velocity (trend not plotted). Based on these trends, all of the Doppler signal characteristics depend strongly on the velocity as indeed may be expected. Doppler frequency and FWHM increase, but SNR decreases when velocity increases.

Varying laser spot position for fixed angular velocity

The focused beam spot was scanned over the central vertical axis of the disk, from the disk center to its edge. The measurements were performed at 11 points at radial distances from the disk center of 1 to 49 mm. Throughout this experiment, the angular velocity was held constant at 1.53 rad/s, the focal length of the lens was 8 mm, and the angle of incidence was $15\,^{\circ}$. The linear velocity, v_{cent}, which is the velocity of the disk at the center of the beam spot can be calculated from $v_{\mathrm{cent}} = r\omega$, where r is the radial distance of the beam spot center from the disk center and ω is the angular velocity of the disk. The velocity will naturally increase as the spot moves closer to the disk edge, therefore having an effect on the Doppler spectrum similar to the trend observed in this section.

The experimental and simulated Doppler spectra are plotted in Fig. 4.12(a) and (b), respectively and the trends are plotted in Fig. 4.13(a) and (b) for FWHM and SNR, respectively, while Doppler frequency, as expected, increases linearly with the laser spot radial distance from the disk center (trend not plotted). Trends here are very similar to

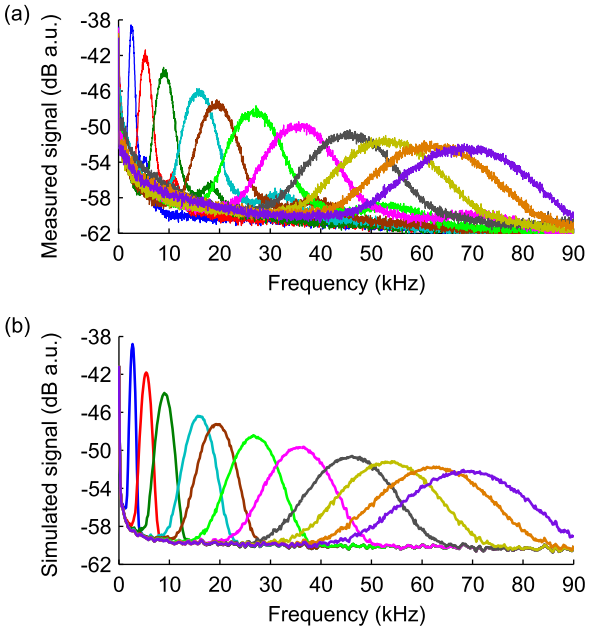

FIGURE 4.10: (a) Experimental and (b) simulated Doppler spectra varying angular velocity of the disk. The peaks from left to right correspond to angular velocities 0.22, 0.44, 0.74, 1.30, 1.56, 2.20, 2.93, 3.77, 4.38, 5.12, and 5.65 rad/s.

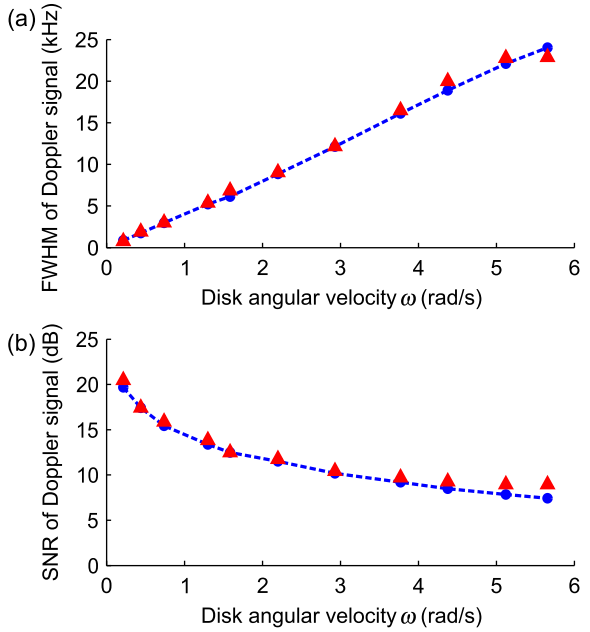

FIGURE 4.11: Experimental (red solid triangles) and simulated (blue broken line) results for (a) FWHM and (b) SNR vs. angular velocity of the disk.

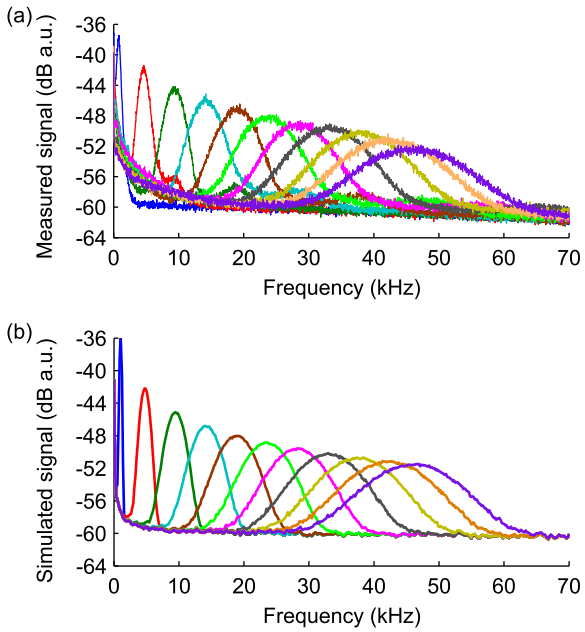

FIGURE 4.12: (a) Experimental and (b) simulated Doppler spectra varying the beam spot position on the vertical disk axis with constant angular velocity. The peaks from left to right correspond to beam spot positions of 1, 5, 10, 15, 20, 25, 30, 35, 40, 45, and 49 mm.

the trends in the previous subsection. However, by increasing the distance from the center, the fractional change of velocity across the beam spot decreases. This effect will be investigated in detail in Sec. 4.2.4.

Varying angle of incidence

The angle between the normal to the disk and the laser beam axis was varied over 8 different values from 3° to 36°, (θ; see Fig. 1). At each angle, both the experimental and simulated Doppler spectra were obtained and are plotted in Fig. 4.14(a) and (b). The target was placed in the focal plane by adjusting the target distance from the laser to achieve maximum signal strength. Experimental and simulated trends for Doppler frequency, FWHM, and SNR with regard to angle of incidence are plotted in Fig. 4.15(a), (b), and (c), respectively. Experimental and simulated trends agree well and it can be concluded that as the angle increases, the Doppler frequency increases, the FWHM steadily decreases, but SNR stays relatively constant. There are discrepancies between simulated and experimental FWHM at approximately 11° and 36°. This is possibly due to a limitation in the manner in which the target scattering is modeled. The focal length of the lens and angular velocity of the disk were 8 mm and 0.79 rad/s, respectively. The beam spot was located 20 mm above the disk center.

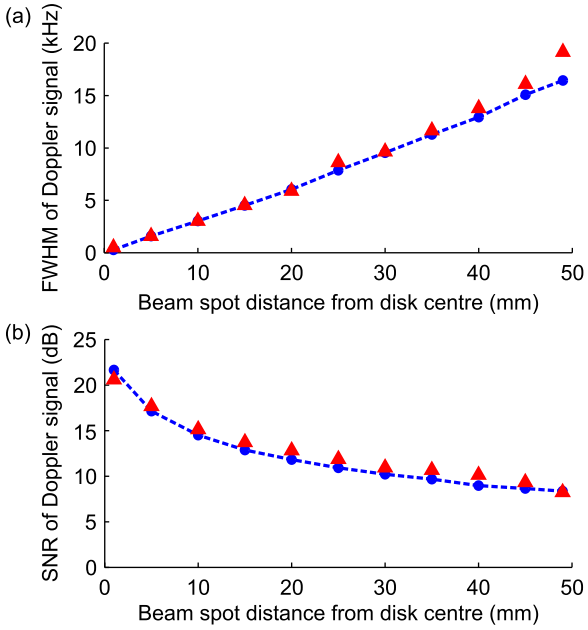

FIGURE 4.13: Experimental (red solid triangles) and simulated (blue broken line) results for (a) FWHM and (b) SNR vs. the beam spot position on the vertical axis with constant angular velocity.

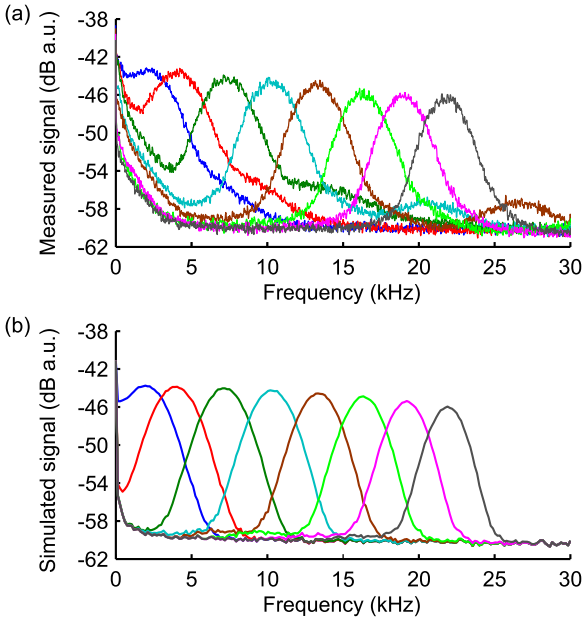

FIGURE 4.14: (a) Experimental and (b) simulated Doppler spectra for varying angle of incidence. Lines, in both sub-figures, correspond to angles $3\,^{\circ}$, $6\,^{\circ}$, $11\,^{\circ}$, $16\,^{\circ}$, $21\,^{\circ}$, $26\,^{\circ}$, $31\,^{\circ}$, and $36\,^{\circ}$ from left to right.

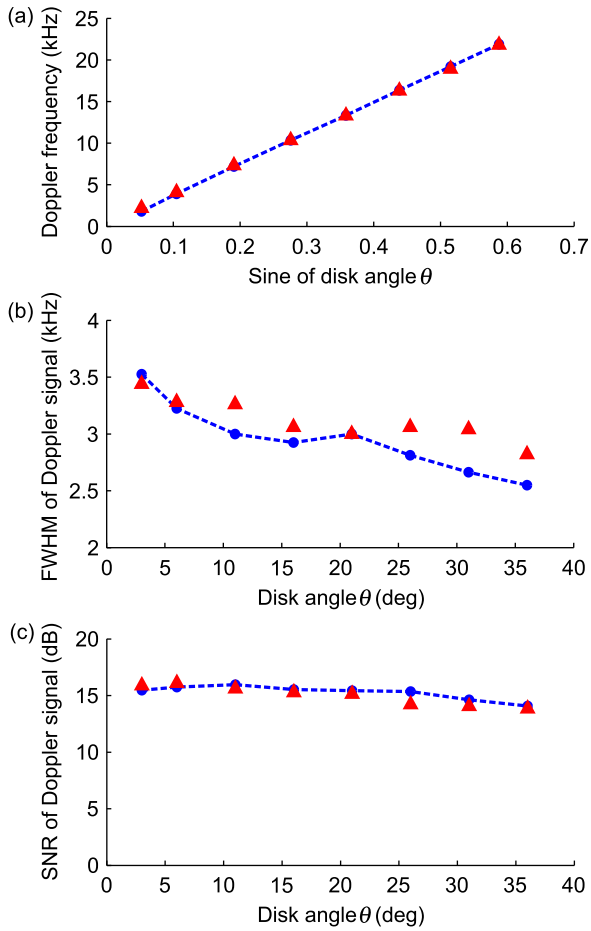

FIGURE 4.15: Experimental (red solid triangles) and simulated (blue broken line) results for (a) Doppler frequency, (b) FWHM, and (c) SNR vs. angle of incidence.

Varying fractional change of velocity across the beam spot

In this section we investigate the effect of the fractional change of velocity across the beam spot. The beam spot position was moved along the vertical axis of the disk, while the linear velocity at the beam spot center was kept constant. The angular velocity ω was adjusted to maintain the same Doppler frequency and therefore linear velocity at the center of each spot position. We choose to divide the effect of changing this parameter on the Doppler spectrum into two regimes — the regime when the laser spot is close to the disk center, and the regime when the laser spot is distant from the disk center. We term these regimes the close regime and distant regime, respectively, throughout the rest of the paper. To quantify the fractional change of velocity across the beam spot, we define

a fractional change ratio as:

$$F = \frac{\Delta v}{v_{\text{cent}}} = \frac{(v_{\max} - v_{\min})}{v_{\text{cent}}}\,, \tag{4.2}$$

where $\Delta v = (v_{\max} - v_{\min})$ is the difference between the maximum and minimum linear velocities of the disk surface within the spot and v_{cent} is the linear velocity at the center of the spot. For a focal length of 8 mm and collimated beam diameter of 1.96 mm, w_0 was calculated to be 2.2 µm [106]. We define the boundary between close and distant regimes at $F = 0.1$ (in this case corresponding to $r = 44$ µm); therefore, the close regime has $F > 0.1$ and the distant regime has $F < 0.1$.

A Doppler frequency of 10 kHz and an incidence angle of $15\,^\circ$ were maintained throughout this section to ensure the velocity at the spot center remained constant. The maximum speed that the servomotor could reliably produce was 2π rad/s. This meant that the beam spot could not be closer than 3 mm to the disk center whilst maintaining the same Doppler frequency. Thus, the close regime was studied only by simulation. The MC simulation was performed at 5 steps from 5 to 70 µm from the disk center and the Doppler spectra are plotted in Fig. 4.16 (a). The FWHM and SNR for the close regime are plotted in Fig. 4.16(b). The boundary between the close and distant regimes is indicated by a vertical line at $r = 44$ µm. It can be seen that the FWHM and SNR are strongly affected in the close regime, where F is greater than 0.1. FWHM decreases while SNR increases when the spot moves away from the center. On the contrary, no observable impact of velocity gradient on the FWHM was observed for measurements performed in the distant regime.

Varying beam NA

The NA of the beam is defined as $\mathrm{NA} = D/(2f)$, where f is the focal length of the lens and D is the $1/\mathrm{e}^2$ power diameter of the collimated beam when it crosses the objective lens. The beam NA of the system was varied through using objective lenses with different focal lengths. Changing the focal length of the lens also changes the beam spot size ($1/\mathrm{e}^2$ power diameter) on the disk. Simulation was performed for 5 different focal lengths from 8 to 24 mm. For the experimental validation of the results we refer to previous work which is consistent with the simulation results in this section [99]. The diameter of the collimated beam was 1.96 mm and the spot was positioned 20 mm above the disk center, with an incidence angle of $15\,^\circ$. Focal lengths of 8, 12, 16, 20, and 24 mm produce beam NAs of 0.12, 0.08, 0.06, 0.05, and 0.04, with beam spot sizes of 4.4, 6.6, 8.8, 11.1, and 13.3 µm,

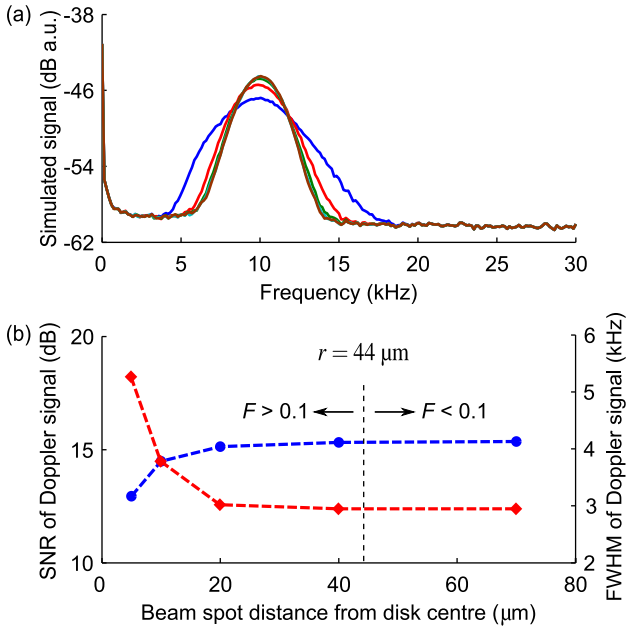

FIGURE 4.16: (a) Simulated Doppler spectra, varying fractional change of velocity across the beam spot in the case where the spot is close to the disk center. The beam spot distances from the center of the disk for widest to narrowest spectra are 5, 10, 20, 40, and 70 µm. (b) FWHM (diamonds) and SNR (circles) simulation results vs. beam spot distance from disk center, varying fractional change of velocity across the beam spot in the case where the spot is close to the disk center. 44 µm lines show the boundaries between close and distant regimes.

respectively. The disk was positioned in the focal plane of each lens. The simulated Doppler spectra for each of these different lenses are plotted in Fig. 4.17. Simulation results FWHM and SNR are shown in Fig. 4.18, respectively, while Doppler frequency, as expected, stays constant (trend not plotted). Based on these trends, it is seen that while Doppler frequency stays the same, FWHM and SNR increase strongly with beam NA. Although the effect of NA on spectral broadening is known [99], here we provide a quantitative analysis of its effect.

Other contributions to the spectrum

In this section we study the effect of system imperfections — system vibration, target surface profile, instability in target velocity, and laser linewidth.

Small mechanical vibration and target surface profile (imperfection in the flatness of the target) were simulated as uncertainty in the position of the target along the laser beam axis, with a maximum uncertainty of 10 µm. In both cases, the effect was a negligible broadening of the Doppler spectrum on the order of a few hertz. Moreover, the Doppler

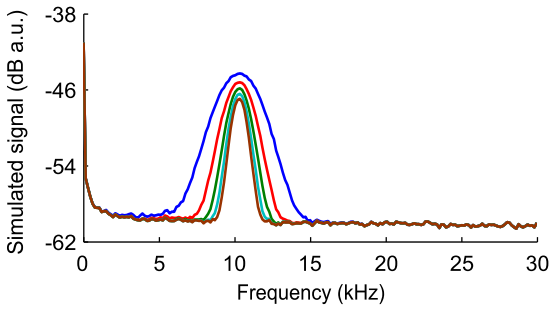

FIGURE 4.17: Simulated Doppler spectra varying beam NA. The beam NAs used for the narrowest to widest spectra are 0.04, 0.05, 0.06, 0.08, and 0.12.

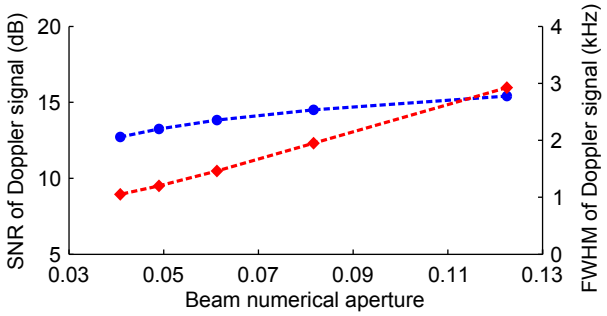

FIGURE 4.18: FWHM (diamonds) and SNR (circles) simulation results vs. beam NA.

frequency and SNR changes obtained by simulation were likewise negligible.

Instability in the disk velocity was simulated as random fluctuations with a Gaussian distribution in the angular velocity of the disk, characterized by analyzing the servomotor encoder signal via the fast Fourier transform. Instability in the disk velocity was measured as decreasing linearly from 5 to 0.1 % of the average velocity as the servomotor average angular velocity was increased from 0.14 to 2π rad/s. In order to further study the effect of velocity instability on FWHM, and to assist in the analysis of our other results, we use and modify an expression from [99]:

$$\mathrm{FWHM} \propto \frac{\mathrm{NA}\, v\, \cos\theta}{\lambda}, \tag{4.3}$$

where v is the linear velocity, θ is the angle of incidence shown in Fig. 4.7, λ is the laser's emission wavelength, and NA is the beam numerical aperture. From Eq. (4.3), broadening is linearly proportional to disk velocity, and so additional broadening due to instability in velocity will be fractionally proportional to the instability in velocity. As this ranges from 5 to 0.1 % of the mean velocity, as stated above, the corresponding additional broadening will also be 5 to 0.1 % of the nominal FWHM. To examine the analytical

results through simulation, we included the measured instability in disk velocity into the MC simulation by using a random angular velocity with Gaussian distribution, centered at the mean velocity. As expected the simulation results showed small broadening in line with the analytical results. Based on this simulation, the Doppler frequency and SNR changes due to instability in disk velocity are considered negligible.

The VCSEL's linewidth is in the range of tens of MHz, which is extremely narrow relative to its operating frequency of 350 THz (about $1:10^7$) [67]. To examine the contribution of the non-zero laser linewidth, instead of using a constant value as the photons' frequency in the MC simulation, we used a random frequency with Gaussian distribution around the central emission frequency with a FWHM of 50 MHz. As expected, the results showed negligible effects on the Doppler frequency, FWHM, and SNR. It is concluded that non-zero linewidth has a minor effect on the Doppler spectrum.

4.2.5 Discussion

In this section we examine the morphology of the Doppler spectrum as evidenced in the experimental and simulated results of the previous section. We classify the parameters as having major or minor effects on the Doppler frequency, FWHM, and SNR, depending on their significance in affecting each characteristic. Care must be taken when considering our analysis in the context of LFI velocimetry system configurations that differ greatly from our own, in terms of dimensions, target velocity range, beam NA, etc., since a parameter that has a minor effect here could be important in a different system or vice versa.

The central Doppler frequency is representative of the velocity of the disk at the center of the beam spot. This velocity and hence the disk's angular velocity are easily obtained from (5.2). The verification of the Doppler shift formula (5.2) is an expected outcome of the experiments and simulation. The parameters having a major contribution to Doppler frequency are target velocity and angle of incidence. The other parameters, which are the fractional change in velocity across the beam spot, beam NA, system vibration, target surface profile, laser linewidth, and velocity instability have minor effects on Doppler frequency. Trend in Doppler frequency for angle of incidence is plotted in part (a) of Fig. 4.15.

The intrinsic characteristics and imperfections of the system result in spectral broadening which we measure as FWHM. Velocity, spot position, angle of incidence, and beam NA are the parameters that have a major effect on FWHM. When the angular velocity of the disk increases, the FWHM will increase linearly as well, as shown in Fig. 4.11(a). The effect of angle of incidence on FWHM shown in Fig. 4.15(b) can also be obtained from

Eq. (4.3). The maximum FWHM occurs when θ is close to zero. When θ increases the FWHM will decrease. Therefore, when the angle between beam axis and target changes dramatically, a major variation in FWHM is observed.

All of the variables that could change the beam NA such as focal length, spot size, objective lens diameter, have a major effect on FWHM. As can be seen in Fig. 4.18(a), increasing the beam NA through reducing the focal length will result in an increase of the FWHM. The direction of the photons' $\mathbf{k}_s$ and $\mathbf{k}_i$ vectors depends on the beam NA of the system. This has an obvious effect on the Doppler shift formula Eq. (5.2), so changing the photons' directions causes a significant shift in the frequency of the photons and major broadening in the spectrum. Whenever beam NA increases or decreases, FWHM will likewise increase or decrease consequently. It is clear and expected from theory that a change in focal length results in a change in both NA and spot size. However, it is evident from the experiments described in Sec. 4.2.4 that what truly impacts the spectrum is the change in convergence angle due to NA.

The fractional change of velocity across the beam spot when the spot is close to the disk center, with $r < 44$ µm, has a major effect on spectral broadening, whilst in the corresponding distant regime, $r \geqslant 44$ µm, the effect is minor. Here, 44 µm is equal to only ten times the beam spot diameter and is negligible when considering our system dimensions.

However, this effect may be important in systems where the sensing volume is relatively large and the fractional change of velocity across the beam spot is considerable, as can be the case in microfluidic flowmetry systems [79]. In the distant regime, FWHM varies little with radial distance while keeping the spot center linear velocity constant. Experimental values are quite consistent except at the two lower r values. The increased FWHM at these points could be a result of increased noise due to speeding up the disk to keep the linear velocity constant. The effect of the fractional change of velocity across the beam spot on FWHM in the close regime can be seen in Fig. 4.16(b). It is shown by simulation that when the spot is very close to the disk center, the FWHM increases greatly. System vibration, target surface profile, laser linewidth, and instability in disk velocity are also among the parameters having a minor effect on FWHM. We note that our modified Eq. (4.3) encapsulates most of the above major trends for spectral broadening.

Figs. 4.11 (b), 4.13 (b), and 4.15 (c) show the SNR to decrease with angular velocity, beam spot distance from the disk center, and angle of incidence, respectively. In contrast, SNR increases with beam spot distance from the disk center (in the close regime) and beam NA, as shown in Fig. 4.16(c) and Fig. 4.18(b), respectively. For most of the system parameters examined here, trends in SNR are in opposition to trends in FWHM. This is

TABLE 4.1: Effect of system parameters on Doppler frequency, FWHM, and SNR. Major and minor effects are shown by ✓and ✗, respectively.

Parameter	Doppler freq.	FWHM	SNR
Incident angle	✓	✓	✗
Velocity	✓	✓	✓
Velocity change (close)	✗	✓	✓
Velocity change (distant)	✗	✗	✗
Beam NA	✗	✓	✓
System vibration	✗	✗	✗
Surface profile	✗	✗	✗
Non-zero linewidth	✗	✗	✗
Velocity instability	✗	✗	✗

consistent with the Gaussian Doppler component of the spectrum having constant power, whereby broadening of the Gaussian distribution will lower the peak power (that is, the power at the Doppler frequency). However, when beam NA increases, both the FWHM and SNR will increase, perhaps due to an increase in effective collection solid angle. Target velocity, spot position, fractional change of velocity across the beam spot when the spot is close to the disk center, and beam NA have a major effect on SNR. On the other hand, angle of incidence, fractional change of velocity across the beam spot when the spot is distant from the disk center, system vibration, target surface profile, laser linewidth, and velocity instability have a minor effect on SNR.

The effect from different parameters on the Doppler frequency, FWHM, and SNR of our LFI velocimeter are summarized in Table 4.1. We note that when the effect of the change in velocity distribution across the spot is small (i.e. in the distant regime), the effect of varying the position of the laser spot on the disk as explored in Sec. 4.2.4 is equivalent to simply changing the velocity of the disk.

4.2.6 Conclusion

In this work, experiments and accurate simulation of an LFI velocimeter have been performed to analyze the morphology of the Doppler spectrum. Major and minor effects on Doppler frequency, FWHM, and SNR are classified and discussed. The parameters that have a major effect on the spectrum are angle of incidence, velocity, beam NA, and fractional change of velocity across the beam spot when the spot is close to the disk center. System vibration, target surface profile, instability in target velocity, laser non-zero

linewidth, and fractional change of velocity across the beam spot when the spot is distant from the disk center are all parameters with a minor effect on the Doppler spectrum. The calibrated MC simulation technique used here was able to accurately reproduce experimental Doppler spectra, and subsequently to investigate the detailed contribution of system parameters to the Doppler spectrum which are difficult to isolate in experiment. The analysis carried out here will enable more precise design of LFI velocimeters to isolate or suppress particular effects. Moreover, the consistency of the calibrated MC simulation technique with experiment used here lends weight to simulated output, enabling its use for the analysis and rapid prototyping of more complex targets and systems in simulation.

4.3 Paper C

Mowla, Alireza and Taimre, Thomas and Lim, Yah Leng and Rakić, Aleksandar D, "Monte Carlo Model of Laser Doppler Perfusion Imaging in Skin Cancer Detection," Optical Society of America, CLEO-PR, Busan, Korea, 26H3_2 (2015).

4.3.1 Abstract

We present a laser Doppler perfusion imaging model to map the perfusion in melanoma and non-melanoma skin cancers. We numerically investigate the use of neovascularization as an early detection method using Monte Carlo method to simulate the interactions of photons and skin tissue.

4.3.2 Introduction

Melanoma and non-melanoma skin cancers (NMSCs) have the highest incidence rate among the white-skinned population and their incidence rate is increasing worldwide [107, 108]. Although NMSCs have a high cure rate, they are a heavy economic burden on the health systems. Despite advances in treatments for skin cancer, early detection remains the key to decrease mortality rate in all kinds of skin cancers [3] and reduce the chance of metastasis. To develop an effective method for early skin cancer detection, we need to study the biological traits of the cancer. Angiogenesis or neovascularization is amongst the hallmarks of cancer growth [14]. Angiogenesis occurs in early stages of tumorous growth and is the key mechanism for providing the oxygen and nutrition for the tumorous cells and removing their waste. Angiogenesis is the result of endothelial sprouting from the preexisted venules and it causes the microcirculation to show a series of structural and functional abnormalities [109]. Therefore monitoring skin perfusion can be a potential strategy for early detection. Laser Doppler flowmetry as a well-established technique is considered as the first choice in perfusion imaging [54]. Although laser Doppler perfusion imaging (LDPI) has been used in assessing perfusion levels in different skin tumors [12, 13], it hasn't been considered seriously as an early skin cancer detection tool yet. The lack of specificity and LDPI limitations are the main reasons for this. Developing a powerful model to describe photontissue interactions in a LDPI early skin cancer detection system can help us in better understanding of the effect of different parameters in biological micro regions on the perfusion image, and provide systematic investigations

into the characteristics of the LDPI system. Here we developed an accurate Monte Carlo model of a LDPI system and modeled skin tumors through their higher concentration and velocities of red blood cells (RBCs).

4.3.3 Methodology

Our approach is to model the skin by six layers of tissue and include the abnormalities of higher RBCs concentration and velocity to define tumorous tissue. The resulting photontissue interaction in an LDPI system with this skin model is then studied by means of Monte Carlo simulation and raster scanning the light source to create a perfusion image of the skin.

Laser Doppler Perfusion Imaging

A laser Doppler perfusion imaging device raster scans the laser beam over an area of interest on the skin surface to map the blood perfusion. It can utilize two rotating mirrors to scan the collimated beam or move the laser to scan the focused beam. Photons at proper wavelengths with longer penetration depth will enter the tissue and hit the chromophores and scatterers inside the tissue. Photons will be absorbed or scattered. The scattering events can be either static or dynamic from fixed and moving scatterers, respectively. Dynamic scattering events cause a Doppler shift in the frequency of the scattered photons. The Doppler shift will be calculated from the following formula:

$$\Delta f = \frac{1}{2\pi}(\mathbf{k}_s - \mathbf{k}_i) \cdot \mathbf{v}\,, \tag{4.4}$$

where Δf is the Doppler shift in the frequency of the light, $\mathbf{k}_s$ and $\mathbf{k}_i$ are the wave vectors of the scattered and incident waves, respectively, and $\mathbf{v}$ is the velocity vector of the moving scatterer. Backscattered photons from the skin tissue will be collected. Doppler power spectrum is derived by applying fast Fourier transform on the time domain photocurrent signal. Perfusion is proportional to the first momentum of the Doppler power spectrum:

$$\mathrm{Perf} \propto \int_0^\infty \omega P(\omega) d\omega\,, \tag{4.5}$$

where ω is the angular frequency and $P(\omega)$ is the Doppler power spectrum. By measuring the perfusion at each point in a raster scanning mode, we can map the blood perfusion

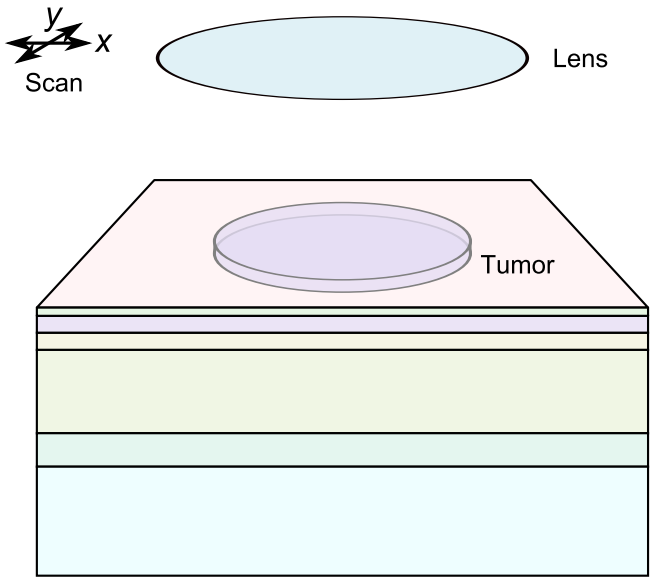

FIGURE 4.19: The schematic view of the six-layer skin tissue with the cylindrical tumorous area in the second layer.

image of the skin.

Monte Carlo

Our skin model in this work is based on a model presented by Fredriksson *et al.* [110]. This is a six-layer skin tissue model. Each layer contains three types of low, mid, and high velocity blood components of 0.3, 3.0, and 30 mm/s, respectively. Names and thicknesses of the layers from top to bottom are as follows: epidermis 75 µm, papillary dermis 150 µm, superior blood net 150 µm, reticular dermis 800 µm, inferior blood net 400 µm, and subcutis 2000 µm. Melanin as the main absorber exists only in the outer layer of epidermis. The Gegenbauer kernel phase function with $\alpha_{Gk} = 1$ and $g_{Gk} = 0.948$ is considered as the backscattering phase function of the photons from the RBCs [110]. In our model photons are launched in a focused beam format with a hyperboloid shape to resemble a Gaussian beam [61]. Variance reduction is undertaken to focus on the Doppler shifted photons [110]. The potential tumor is defined as cylindrical area with higher RBCs concentration and velocities. Its radius and thickness are 3 and 0.15 mm respectively. It is located in the depth of 75 to 225 µm in the papillary dermis layer. A schematic of the mode structure is shown in Fig. 4.19.

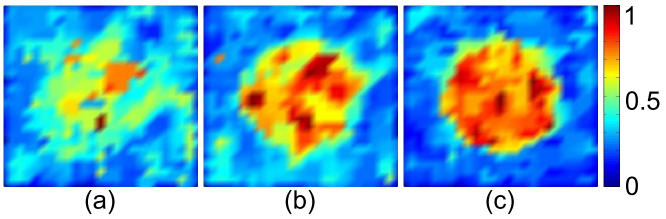

FIGURE 4.20: Perfusion maps of three types of skin lesions with RBCs concentrations of (a) two (b) four and (c) six times higher than normal and velocities of 1.5 times higher than normal.

4.3.4 Results and Discussion

Stücker *et al.* measured the perfusion of malignant and benign skin lesions [12, 13]. Based on their measurements, basal cell carcinoma, melanocytic nevus, and malignant melanoma have higher perfusion levels of about two, four, and six times the normal perfusion of the surrounding tissues [12]. Considering these measurements we modeled three types of precursors with different levels of RBCs concentration and velocities. Concentrations of two, four, and six times the normal volume concentration of 0.2 % and the velocities of 1.5 times the normal velocity of 0.3 mm/s have been studied. Resulted perfusion maps are depicted in Fig. 4.20 in a 25 by 25 steps scan images. The only blood component in the papillary dermis layer is the low velocity components of 0.3 mm/s with the concentration of 0.2 % volume [110].

As depicted in Fig. 4.20 the higher RBCs concentration and velocities in the model result in higher perfusion. All the images are normalized to their maximum values and the study is based on relative values more than absolute values. Absolute perfusion unit is one of the challenges in LDPI systems and one of the merits in LDPI early skin cancer detection is that there is no need to distinguish between the effects of RBCs concentration and velocities as both of them exist in a tumorous precursor and relative comparison between the lesion area and surrounding normal tissue is enough in diagnosis purposes. RBCs in this model are randomly scattered in the tissue and their velocity directions are randomly distributed in the space with an even distribution. As seen in Fig. 4.20 increasing the RBCs concentration and velocities even in low levels is detectable in the perfusion maps. This simulation model is useful in sensitivity and specificity evaluation and to compare the effect of RBCs concentration and velocities on the perfusion map separately.

4.3.5 Conclusion

We studied laser Doppler perfusion imaging as a potential early skin cancer detection method. Photons tissue interaction was studied using a Monte Carlo simulation which enables us to study the effects of biological micro regional parameters on the perfusion map and explore the systems features, systematically.

Chapter 5

5. Concurrent Laser Doppler Flowmetry and Confocal Reflectance Imaging

This chapter includes papers D and E. Paper D for the first time proposes concurrent acquisition of confocal reflectance microscopy and laser Doppler flowmetry using an integrated and compact LFI system. Both confocal reflectance microscopy and laser Doppler flowmetry are well-established non-invasive techniques which have been used in the area of optical imaging during the past few decades. This dual-modality imaging system not just improves the contrast and signal to background ratio of the images, but also provides functional and morphological information of the blood perfusion and optical properties of a sample at the same time. Although in this paper we applied the idea experimentally to a microfluidic channel containing a dynamic turbid flow, this combination technique can also play an important role in skin cancer detection, as it is discussed numerically in paper E. This paper delves into the details of the biology of skin cancer and the characteristics of the affected tissue. The use of different modalities such as Doppler flowmetry and confocal reflectance and the effectiveness of dual-modality imaging in the area of skin cancer detection are also included in this paper. In this paper, physiological changes that occur in melanoma and keratinocyte skin cancers are discussed. The proposed combinational technique is then applied numerically to provide images from two typical models for keratinocyte skin cancers, grouped as mild and severe cases, to evaluate the improvement in the imaging due to the application of the new technique. A numerical melanoma model is excluded as it has a different geometrical shape compared to keratinocyte skin cancer, but results are extendable to melanoma as well.

Angiogenesis or neovascularization is one of the biomarkers of cancer [14]. This abnormal blood activity can be detected by monitoring blood perfusion using a laser Doppler

flowmetry. On the other hand, cancerous activity changes the morphology of the affected tissue and its optical properties [11] which can be monitored by a confocal reflectance microscope. Therefore, an integrated LFI which is able to image both laser Doppler flowmetry and confocal reflectance microscopy at the same time, has the capacity to reveal information about both biomarkers at the same time. Applying this technique to skin cancer detection experimentally could effectively improve skin cancer detection.

5.1 Paper D

Mowla, Alireza and Taimre, Thomas and Lim, Yah Leng and Bertling, Karl and Wilson, Stephen J. and Prow, Tarl W. and Rakić, Aleksandar D, "A Compact Laser Imaging System for Concurrent Reflectance Confocal Microscopy and Laser Doppler Flowmetry," IEEE Photon. J. **8**, 3900709, (2016).

5.1.1 Abstract

We propose a compact laser feedback interferometry imaging system for concurrent reflectance confocal microscopy and laser Doppler flowmetry. This system acquires both confocal reflectance and Doppler signals in a confocal architecture to image dynamic turbid media with higher contrast than a system operating in either modality, and is coherent in nature. In a confocal optical configuration, reflectance confocal microscopy provides information about scattering from within a small volume centered around the focal point of the confocal system, and laser Doppler flowmetry provides information about the velocity of moving scatterers within the same volume. Raster scanning the sample enables the concurrent creation of two images, containing independent information, from a well specified depth within the sample. Concurrent spatial mapping of these independent sensing modalities affords improvement in the capability of the imaging system by obtaining additional information from both morphological and functional features of the dynamic turbid medium, at depths penetrable by near-infrared lasers. We realize the idea using a laser feedback interferometry imaging system scanning a microfluidic channel which contains a dynamic turbid medium. We show the effectiveness of this integrated imager quantitatively through the improvement of the signal to background ratio of a combined (multiplication) image.

5.1.2 Introduction

Two major optical imaging techniques used in non-invasive biological diagnostic practices are reflectance confocal microscopy (RCM) [31, 111] and laser Doppler flowmetry (LDF) [13, 15, 16]. RCM and LDF images spatially map the contrast in optical properties and blood microcirculation of the biological tissues, respectively. Optical properties, such as scattering and absorption coefficients and optical refractive index, are morphological biomarkers which can be mapped by measuring the optical reflectance in

RCM [31, 111, 112]. Blood microcirculation is a functional biomarker which can be quantified and imaged by LDF [16, 113]. Both can be considered as biomarkers for identifying deformity and abnormal activity in the tissue caused by a disease [13, 31].

Although reflected signals from dynamic turbid media contain information about both the reflectance intensity and Doppler, laser imaging systems normally record one of these modalities at a time. For instance, Wardell *et al.* considered the influence of tissues' optical properties on the Doppler signal, manifested through backscattering level, as a nuisance and ignored it by normalizing the photodetector signal to the average photocurrent and neglecting the dc part of the signal [16]. However, this neglected information is in fact the reflectance of the laser beam.

The combination of imaging modalities has previously been explored: for example, combining optical coherence tomography with Doppler flowmetry [50] or multispectral reflectance imaging with laser speckle flowmetry [114]. Furthermore, laser reflectance and Doppler images of the same tissue were provided using separate systems for the purpose of comparison [115]. Despite this, the authors remain unaware of any work to date that simultaneously extracts and utilizes both confocal reflectance and Doppler flowmetry parts of the signal in an integrated confocal laser imaging system.

In a confocal optical configuration, RCM provides information about scattering from within a small volume centered around the focal point of the confocal system, effectively suppressing reflection from the surface of the sample (as well as from outside this small volume). The measured signal is usually referred to as the RCM signal [31] and it provides information from a well specified depth within the sample, being entirely different from the conventional image of the sample surface. While the RCM signal provides information about morphology of the sample, the LDF signal provides information about the spatial distribution of velocities of moving scatterers within the sample. In this article, we obtain both of these signals concurrently using an laser feedback interferometer in a confocal optical configuration.

A laser feedback interferometry (LFI) imaging system works based on self-mixing effect [9, 10, 71, 116], and has already been used in reflectance imaging [117, 118] and Doppler imaging systems [81]. This technique has a simple, easy to align, and inexpensive configuration, wherein the laser serves as both transmitter and receiver. Images provided by this system can then be combined (e.g. added or multiplied) or interpreted separately to improve the sensitivity of the imaging system. To the best of our knowledge, this work is the first time that both confocal reflectance and Doppler modalities are used in an integrated confocal laser imaging system to generate two independent images

concurrently. This paper is structured as follows: We discuss experimental details in section 5.1.3 describing the method and technical considerations, section 5.1.4 presents signal processing procedures, section 5.1.5 contains results and related discussion, which is followed by conclusions in section 5.1.6.

5.1.3 Experimental Details

Our compact laser imaging system to realize the idea is a confocal LFI imaging apparatus [9, 10, 71] in an LDF implementation. This simple system has previously been used to monitor blood perfusion [9, 97]. In an LFI system, a portion of the emitted beam reflects back from the target, re-enters the cavity, mixes with intracavity field, and modulates the optical power, causing interference inside the laser cavity. Therefore, in this system the laser acts as both transmitter and receiver. The remote target forms an external cavity and any changes in the characteristics of this external cavity, either attributed to the dimensions of the external cavity or the behavior of the target, give rise to perturbations in the laser's optical and electrical properties. By monitoring the laser output power or terminal voltage (which is proportional to the output power), these changes can be sensed [10, 119, 120].

In this paper, changes of interest are target's reflectivity level and Doppler shift in the beam frequency. In order to experimentally demonstrate the technique, we require a dynamic turbid medium as a target which contains moving particles and possesses different optical properties with respect to a substrate. An optically turbid medium is a partially transparent material containing randomly distributed scatterer and absorber particles with scattering coefficient well above absorption coefficient so that light will be diffused when passing through such a medium. A dynamic turbid medium is an optically turbid medium that contains both moving and static particles.

We employed a fairly simple target to act as a biological tissue phantom. The target used was a microfluidic channel containing diluted milk flow which is commonly used as a test bed for such systems [121]. Homogenized milk has been used frequently as a blood phantom in modeling biological tissues as its fat particles mimic red blood cells in size and optical properties [85]. Homogenized milk also has high scattering and low absorption coefficients in the near-infrared range which are close to those of blood.

In this laser imaging system, moving fat particles will produce a Doppler shift in the beam frequency and the optical properties of the emulsified solution will generate a different confocal reflectance pattern with respect to the surrounding area of the flow channel, which is a transparent amorphous polymer called Zeonor.

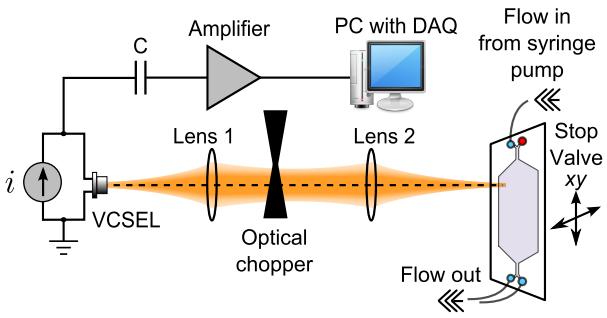

FIGURE 5.1: Laser feedback interferometry imaging set up as an integrated reflectance confocal microscopy and laser Doppler flowmetry imaging system.

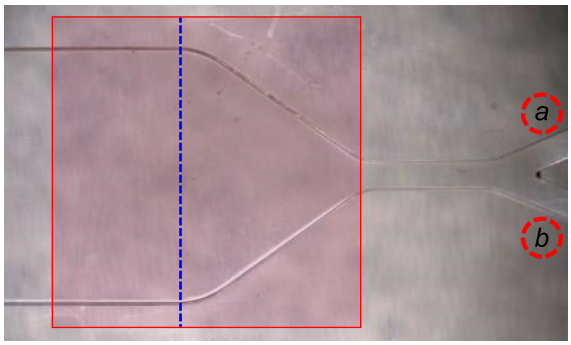

FIGURE 5.2: Two inlet rhombic microfluidic channel. Flow is pushed through from inlet *a* when a stop valve is placed on *b*. Red shaded square shows the scan area and signal to background ratio is calculated along the blue broken line.

Figure 5.1 shows the LFI imaging set up. An 850 nm vertical cavity surface emitting laser (VCSEL) (Litrax Technology Co., Ltd.) was used in this system. This wavelength is particularly interesting in biological applications as water has a low absorption coefficient at 850 nm. The VCSEL was operating at 3.55 mA, just above the threshold current, which was about 3.4 mA under the feedback regime, and the beam half divergence angle was about 7 degrees. The VCSEL's temperature was controlled at 35℃ as the self-mixing signal was stronger and more stable at this temperature [122]. A pair of lenses with focal lengths of 8 mm, clear apertures of 8 mm, and numerical apertures of 0.5 were used to collimate and focus the beam (model C240TME-B, Thorlabs, Inc.).

We used a two inlet microfluidic rhombic chamber chip (microfluidic ChipShop GmbH, product code: 12-0904-0172-05) as the target, shown in Fig. 5.2, containing a homogenized diluted milk flow. We diluted milk by adding two portions of distilled water to one portion of milk. The chamber capacity, depth, and width were 120 µL, 500 µm, and 6.5 mm, respectively. The microfluidic chip was made of Zeonor with a top lid thickness of 188 µm. We focused the beam approximately into the middle of the microfluidic channel

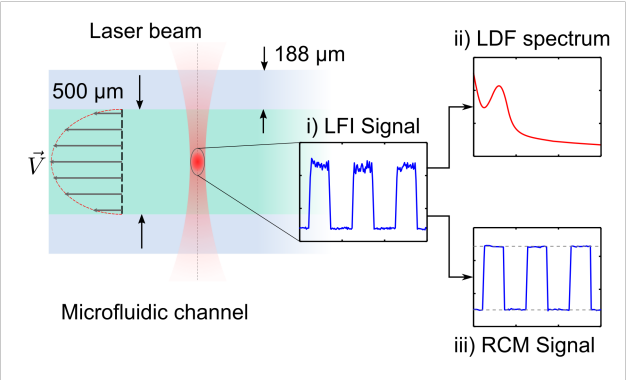

FIGURE 5.3: Cross-sectional view of microfluidic channel. The channel has a depth of 500 µm with 188 µm thick walls made of Zeonor. A focused laser beam is projected into the channel to measure confocal reflectance and Doppler signals due to diluted milk flow at the velocity of $\vec{V}$ (gray arrows). The focused beam has a sensing volume as defined by the gray ellipse. The insets show i) LFI signal containing LDF spectrum and RCM signal obtained from the LFI sensor. ii) depicts the LDF spectrum and iii) the RCM signal, which are both derived from i).

at the depth of about 440 µm from the top surface of the channel.

Figure 5.3 shows the side view of the microfluidic channel including the focused beam. The direction of diluted milk flow and position of the focal point and sensing volume in the center of the microfluidic channel are schematically depicted. The LFI signal contains both LDF and RCM information pertaining to the sensing volume, and is separated into an LDF spectrum and an RCM signal.

To create an intentionally uneven flow distribution in the channel, we put a stop valve on one of the inlets and pushed a 2:1 distilled water-milk solution through the channel using a syringe pump with a flow rate of 400 µL/min. Fluid enters the channel from inlet *a* in Fig. 5.2. The high flow rate and channel size results in a velocity gradient in the flow channel. We expect an even map from the confocal reflectance signal as optical properties stay the same over the whole scan area of the diluted milk. Thus, this non-uniformity of flow in the rhombic channel permits one to readily distinguish between confocal reflectance and Doppler maps. To generate the images, we used motorized two-axis translation stages (Zaber Technologies Inc.) to move the microfluidic channel so that the beam scans the channel in a raster fashion. We raster scanned an area of 8×8 mm^2 in 62×62 steps (at 130 µm pitch), depicted as the shaded area in Fig. 5.2. This area covers the entire channel width of 6.5 mm.

Photons collide with moving particles and are scattered. In a turbid medium the number of scattering events is well above the number of absorption events so that the photons will be diffused and travel in randomized directions. After each collision with a moving

scatterer a shift occurs in the photon's frequency which is equal to the Doppler shift. The effect of the optical system on the Doppler spectrum in an LFI system has been studied in previous work [120]. In the case of multiple dynamic scattering events, an accumulated shift occurs in the frequency of the photon and it becomes challenging to quantify the velocity of dynamic scatterers in absolute terms. Therefore, we compute a Doppler signal (which is a measure of perfusion), which is proportional to the product of the root-mean-square of the scatterer's velocity and concentration [123]. This signal is normalized to its peak value and expressed in arbitrary units, and we refer to it as the Doppler signal.

We used the first moment of the power spectrum to extract the Doppler signal, calculated as follows:

$$\mathrm{Perf} \propto \int_0^\infty \omega P(\omega) d\omega \,, \tag{5.1}$$

where ω is the angular frequency and $P(\omega)$ is the Doppler power spectrum.

In our scheme the beam axis is normal to flow and the resultant frequency spectrum is a broadened Doppler spectrum around zero. This scheme is different from conventional LDF systems, which work at a slanted angle with respect to the flow target. This scheme was chosen because perpendicular laser imaging systems are more desirable in biomedical applications [124].

We obtained the signal from the VCSEL junction voltage which was proportional to the optical output power [77], for simplicity, using less components, and having access to a broader bandwidth [119]. Because the laser was noisy at dc or low frequencies [122], we needed to modulate the beam at a higher frequency to extract the confocal reflectance signal. So we used an optical chopper as a mechanical modulator, shown in Fig. 5.1, to modulate the laser beam in the collimated path. Optical chopper blades modulated the beam at a frequency of 877 Hz, resulting in a time-domain signal containing two voltage levels, corresponding to two different feedback levels [125]. The number of photons which make their ways back to the laser cavity is a measure of the steady state confocal reflectance. LFI signal was obtained from the VCSEL junction voltage fed into a 16-bit data acquisition card after AC-coupled amplification. The sampling rate was 60 kS/s and the number of samples used was 12 kS. We applied the fast Fourier transform to the sampled time sequence to convert the time domain signal to a frequency domain signal and used a Savitzky–Golay filter in Matlab to smooth out the signal and reduce the level of noise.

5.1.4 Signal Processing

To discuss how the signal was processed in order to prepare images, Figs. 5.4 (a)–(c) are included showing three sets of frequency (obtained from fast Fourier transform) and time domain signals from three typical states of the target as: (a) signal from a flow area which includes both confocal reflectance and Doppler, (b) signal from a point outside the flow area including a weak specular reflection from the surface of the microfluidic channel, and (c) signal in the absence of the target (noise floor). Red and green broken lines in Fig. 5.4 are filtered Doppler power spectrum of the LFI signal and noise floor, respectively. This filtered Doppler power spectrum [e.g. the red broken line as annotated in Fig. 5.4 (a)] was taken as the power spectrum in Eq. (5.1). Doppler signal was then calculated as a discretization of Eq. (5.1) using the filtered Doppler power spectrum. As was previously mentioned and can be seen in Fig. 5.4 (a), the Doppler power spectrum is a broadened spectrum around the frequency of zero, as the laser beam axis was perpendicular to the surface of microfluidic channel in our scheme. The confocal reflectance signal was calculated as the magnitude of the first harmonic in the frequency domain signal with respect to the noise level, as annotated in Fig. 5.4 (a). The first harmonic occurs at the frequency of 877 Hz (optical chopper frequency), and higher harmonics due to square modulation of the beam are visible at integer multiples of this frequency. Confocal reflectance and Doppler data can also be interpreted from the time domain signal. For instance, time domain signal in Fig. 5.4 (a) has two levels. Low level shows the noise (obstructed beam), as annotated in Fig. 5.4 (a), while high level contains both the Doppler information, which is the fluctuations on top of the average high level signal as annotated in Fig. 5.4 (a), and steady state confocal reflectance information, which is the average magnitude of the high level signal. The signal in part (b) of Fig. 5.4 does not contain Doppler information whereas it encodes weak reflectance coming from the surface of the microfluidic channel. This reflectance can again be determined by measuring the magnitude of the first harmonic in the power spectrum and it generates a noisy background around the fluid channel. The signal in part (c) of Fig. 5.4 does not contain any confocal reflectance or Doppler information.

5.1.5 Results and Discussion

Normalized scan results are shown in Fig. 5.5. Maps are normalized to the maximum values of the signal at each part. Figure 5.5 (a) shows the Doppler flowmetry map of the scan. As expected the flow has a higher rate on the lower side of the channel as it enters

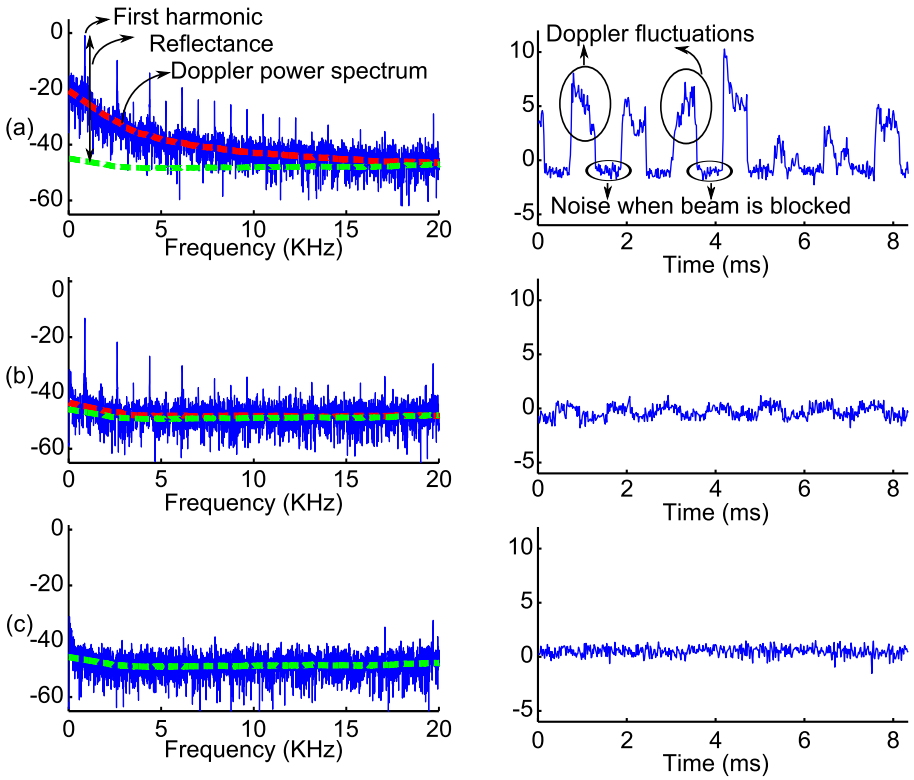

FIGURE 5.4: Frequency and time domain signals from three typical states of the target as (a) signal from a typical flow area, (b) signal from a point outside the flow area, and (c) signal in absence of the target (noise). Red broken lines are the Savitzky–Golay filtered power spectrum and green broken lines are the Savitzky–Golay filtered power spectrum in the absence of target which shows the noise floors.

from inlet *a* in Fig. 5.2. The area near the input of the rhombic channel has the highest flow rate in this image. Figure 5.5 (b) shows the confocal reflectance image from the same scan. These two images are formed concurrently, resulting in two clearly different maps, one containing the Doppler present in the mapped region [Fig. 5.5 (a), directly related to the velocity of the turbid medium] and the other containing information about the level of back-reflected signal [Fig. 5.5 (b), directly related to the optical properties of scatterers]. As expected, confocal reflectance stays at almost the same level over the entire channel because the optical properties of diluted milk remains uniform regardless of the flow rate.

Figure 5.5 (c) shows the combination map which is formed by adding (a) and (b) pixel by pixel. The combined image contains information from both modalities. Hence, loss of data in one modality will not result in a catastrophic loss of contrast in the combined image. To reduce the level of background signal (noise), we can multiply (a) and (b) pixel by pixel. This multiplication image is shown in Fig. 5.5 (d). Multiplying the images reduces the noise markedly. Although it is clear that noise in (d) is lower than noise in

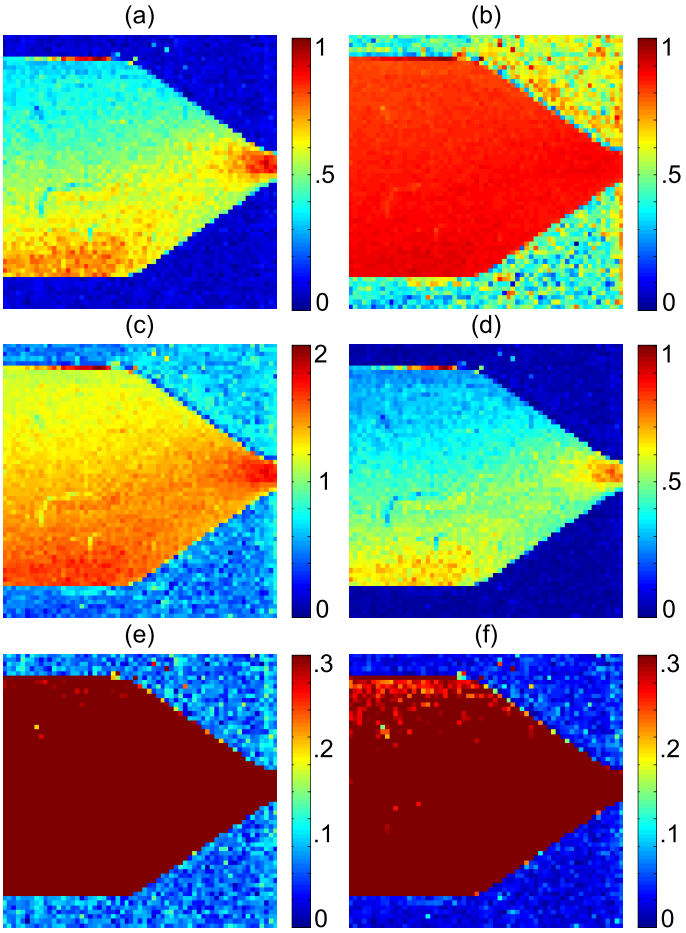

FIGURE 5.5: Normalized scan results and images of (a) Doppler flowmetry, (b) confocal reflectance, (c) addition (of the images in a and b), (d) multiplication(of the images in a and b), (e) Doppler flowmetry (image a) with a limited range, and (f) multiplication (image d) with a limited range.

(b), it is hard to notice this improvement with respect to (a). Therefore, both (a) and (d) are shown with a limited range in (e) and (f), respectively. From (e) and (f), it is clear that multiplication markedly reduces the noise level compared to the Doppler image. Although the noise of the Doppler signal outside of the channel is not high in this experiment, this noise reduction technique could be of great benefit for biological samples.

To quantify the improvement in the sensitivity or contrast of the multiplication image, we define a signal to background ratio (SBR) parameter as the average signal inside the channel (flow region) to the average signal outside the channel. We calculated the average signal level along the all scan lines parallel to and to the left of the blue broken line in Fig. 5.2. Blue, green, and red broken lines in Fig. 5.6 show the average Doppler, confocal reflectance, and multiplication signals, respectively. There are 62 pixels along the blue

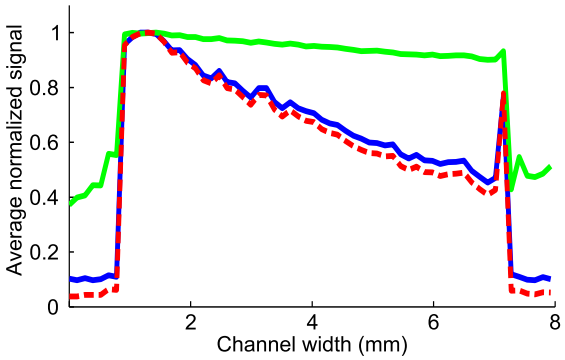

FIGURE 5.6: Average signals on the lateral scans of the microfluidic channel over the rectangular area (along the blue broken line in Fig. 5.2). Blue, green, and red broken lines show average Doppler, confocal reflectance, and multiplication signals, respectively.

broken line in Fig. 5.2, so the SBR was calculated as the average of the signal from the channel or flow area, pixels 8 to 56, to the average of the signal from outside the flow area, pixels 1 to 7 and 57 to 62. The SBRs for average Doppler, confocal reflectance, and multiplication signals are 6.8, 2.0, and 13.7, respectively. Therefore, the improvement in the SBR of the multiplication image compared to Doppler flowmetry and confocal reflectance images are 2.0 and 6.9, respectively.

5.1.6 Conclusions

A compact LFI system and scheme for concurrent RCM and LDF imaging of dynamic turbid media was proposed. In a confocal optical configuration, RCM provides information about scattering from within a small volume centered around the focal point of the confocal system, and LDF provides information about the velocity of moving scatterers within the same volume. Raster scanning the sample enables the creation of two images, containing independent information, from a well specified depth within the sample. This permits one to take advantage of both imaging modalities, and we believe this technique can be used to improve the capability of an integrated confocal laser imaging system. We experimentally demonstrated the applicability of the technique on a simple tissue phantom. The transition to real human tissue requires fast scanning but is otherwise fundamentally straightforward. Such rapid scanning could be achieved by replacing the mechanical translation stage with a fast scanning mirror. A study reporting on an LFI imaging embodiment of this technology has recently been reported in [126]. By conducting simple mathematical operations on the concurrently-obtained images, we can create combined images with increased contrast or sensitivity. For a combined image formed by direct

pixel-by-pixel multiplication, we demonstrated a minimum improvement factor of 2 in the signal to background ratio when compared to each of the individual images.

5.2 Paper E

Mowla, Alireza and Taimre, Thomas and Lim, Yah Leng and Bertling, Karl and Wilson, Stephen J. and Prow, Tarl W. and Soyer, H. Peter and Rakić, Aleksandar D, "Concurrent Reflectance Confocal Microscopy and Laser Doppler Flowmetry to Improve Skin Cancer imaging: a Monte Carlo Model and Experimental Validation," Sensors **16**, 1411 (2016).

5.2.1 Abstract

Optical interrogation of suspicious skin lesions is standard care in the management of skin cancer worldwide. Morphological and functional markers of malignancy are often combined to improve expert human diagnostic power. We propose the evaluation of the combination of two independent optical biomarkers of skin tumours concurrently. The morphological modality of reflectance confocal microscopy (RCM) is combined with the functional modality of laser Doppler flowmetry, which is capable of quantifying tissue perfusion. To realize the idea, we propose laser feedback interferometry as an implementation of RCM, which is able to detect the Doppler signal in addition to the confocal reflectance signal. Based on the proposed technique, we study numerical models of skin tissue incorporating two optical biomarkers of malignancy: (i) abnormal red blood cell velocities and concentrations and (ii) anomalous optical properties manifested through tissue confocal reflectance, using Monte Carlo simulation. We also conduct a laboratory experiment on a microfluidic channel containing a dynamic turbid medium, to validate the efficacy of the technique. We quantify the performance of the technique by examining a signal to background ratio (SBR) in both the numerical and experimental models, and it is shown that both simulated and experimental SBRs improve consistently using this technique. This work indicates the feasibility of an optical instrument, which may have a role in enhanced imaging of skin malignancies.

5.2.2 Introduction

Melanoma and keratinocyte skin cancers (KSCs) are the most common types of cancers affecting fair-skinned populations [107, 127, 128] with incidence increasing about 4% per year worldwide [129]. Although the cure rate is high in KSCs, such as basal cell carcinoma (BCC) and squamous cell carcinoma (SCC), they can become aggressive [128–130].

Squamous cell carcinoma, responsible for about 20% of KSCs, is associated with moderate risk of metastasis [128, 129]. Basal Cell Carcinoma (BCC) constitutes approximately 80% of KSCs, and although metastases are rare, BCC still imposes a significant burden of disease [128, 129]. To alleviate this burden, early non-invasive detection schemes are required.

Most of the technical developments in non-invasive skin cancer detection are based on imaging reflected light from the skin surface or deeper tissues and examination of the image by an expert clinician. These images are interpreted on the basis of structural or functional changes manifest in the optical properties of skin tissue due to neoplastic changes. Changes in optical properties (scattering and absorption coefficients) of neoplastic tissue are due to morphological, molecular and ultrastructural changes [17]. Optical properties of normal skin have been extensively studied [131], and a comparison between healthy and neoplastic skin lesions has been studied in other work [11]. Diffuse reflectance spectroscopy was used to study the light reflectance from tumourous tissues [132, 133]. Furthermore, reflectance confocal microscopy (RCM), which can be used in reflectance mode for in vivo applications [36, 40], evolved to be one of the most promising skin cancer detection tools [31–35]. RCM increases the contrast of a microscope image, provided from within a specimen, by restricting the observed volume.

Other biological traits can be used in early detection of cancers. One of the hallmarks of cancer is angiogenesis [14], as vasculogenic tumour cells cause neovascularization, which plays an important role in tumour growth and cancer metastasis [55,56]. Angiogenesis occurs very early in the multi-stage development of invasive cancers, and it can be attributed to the microscopic premalignant phase of neoplastic progression [14]. Therefore, using a technique such as laser Doppler flowmetry (LDF), a well-established blood perfusion measurement technique [54], to map skin blood perfusion in benign and malignant skin tumours, has potential as a tool in early skin cancer detection [12, 13, 57]. LDF has previously been used for cancer detection purposes and in diagnosing other diseases. Stücker et al. investigated the possibility of differentiating between benign and malignant skin tumours by assessing the level of microvascularization using laser Doppler perfusion imaging [12, 13, 58]. Saravanamuthu et al. used laser Doppler perfusion imaging of vulval skin blood flow to demonstrate abnormal perfusion in vulval cancer [134]. Seifalian et al. examined breast skin perfusion in cases of underlying breast cancer with the hypothesis that increased regional metabolism will result in higher perfusion. It was shown that breast cancer causes higher perfusion in breast skin [15]. This modality suffers from limitations, such as low specificity, because other peripheral vascular diseases,

such as diabetes, arteriosclerosis and vasospastic conditions, can cause similar disturbances in the skin perfusion [16].

In brief, all of the aforementioned techniques suggest that optical biomarkers of malignant changes in skin, used for detection purposes, can be roughly separated into two groups: one related to morphological changes in the skin tissue (quantified through techniques, such as RCM) and the other related to functional changes, such as blood flow (quantified through techniques, such as LDF). The purpose of this work is to combine these two modalities to improve the efficacy of the imaging system. The combination of multiple imaging modalities to improve imaging efficacy has been explored previously in the literature. Chen et al. proposed a method that combines the optical coherence tomography and LDF to measure the blood perfusion and tissue structure at the same time [50]. Yaroslavsky et al. combined multispectral polarized light imaging and confocal microscopy to localize KSCs more accurately [135].

Our approach to combine RCM and LDF is to employ a special configuration for RCM, which is able to pick up the Doppler shift in the frequency of the laser beam. We propose to use a laser feedback interferometry (LFI) system for this purpose. This technique is based on interferometry, which is one of the methods that can be used to extract the Doppler signal. By using LFI in a confocal configuration using a vertical-cavity surface-emitting laser (VCSEL), both confocal reflectance and Doppler flowmetry signals can be acquired concurrently in the same scan without changing the hardware. In the system, the aperture of the VCSEL acts as an RCM pinhole and defines the sensing volume (the lateral resolution and the depth of field of the instrument). The back-reflected beam then interferes with the intra-cavity field to give rise to the Doppler signal. An LFI system is a compact sensing tool which is based on the self-mixing effect [8–10, 71, 136]. It has been previously used for confocal reflectance [117, 118] and Doppler flowmetry [81, 121] imaging purposes.

We examine the proposed technique numerically by applying it to typical simulated models of KSCs, carried out by means of Monte Carlo algorithms specifically adapted for this application, and experimentally by conducting an experiment using an LFI system providing in-depth images of a dynamic turbid medium flowing in a microfluidic channel. We define a signal to background ratio (SBR) parameter to quantify the improvement in the contrast of an image resulting from the multiplication of the RCM and LDF images. There is consistency between simulated and experimental results, and it is shown that SBR for combination images improves significantly in both simulated and experimental studies. The common sensing platform for both measures being LFI, provides an imaging technique where both the confocal reflectance and Doppler flowmetry images can be

acquired concurrently during one single scan. Such an image can be used to discriminate between changes in the blood content and optical properties of skin tumours.

The paper is structured as follows: We discuss the methodology in Section 5.2.3, describing confocal LFI, LDF and Monte Carlo simulations in its subsections. Section 5.2.4 presents the results of the simulated skin tumour models. Section 5.2.5 and its subsections describe the experimental setup, technical considerations and results. This section is followed by the discussion in Section 5.2.6, and finally, we give the conclusion.

5.2.3 Methodology

Our approach to study the technique is through Monte Carlo simulation of photon-tissue interactions and experimental validation by examining a microfluidic channel containing a dynamic turbid medium. Our numerical configuration consists of tumourous skin models and a confocal LFI optical system [8, 10, 81, 120, 137]. We described skin using a six-layer model, and tumourous regions were included as areas with enhanced red blood cell (RBC) activity and altered optical properties. We considered two typical models for skin tumours, and the characteristics of these typical types of skin cancer were defined based on the reported values in the literature. To acquire the signal and form the image in simulations, we raster scanned the confocal LFI model over the skin model. The signal was then processed to extract confocal reflectance (from the number of detected photons) and the Doppler signal (from the Doppler power spectrum). Then, the confocal reflectance and Doppler images were combined by multiplying the signals point by point. Among the different techniques to combine the images, we chose multiplication, as it suppresses the background noise and improves the SBR. The combined image provided by this technique is affected by four different parameters: (i) RBC concentration, (ii) RBC velocities, (iii) tissue scattering coefficient (iv) and tissue absorption coefficient; all of which are optical biomarkers of neoplastic changes. Following the numerical part, we include an experimental part in the paper to evaluate the technique. Experiments were conducted using a confocal LFI system imaging a microfluidic channel containing a dynamic turbid medium, consisting of a diluted Intralipid (20%) with deionized-water. We obtained the confocal reflectance and Doppler images and combined them to make the multiplication image. There is a high level of concordance between the experimental and numerical results, which validates the technique.

In the following subsections, we discuss confocal LFI, LDF and also the specifications of our specifically-adapted Monte Carlo algorithm to examine the multi-layer tumourous skin model.

Confocal Laser Feedback Interferometry

One of the most widely-accepted non-invasive modalities used to provide in vivo images inside living organisms is RCM [138]. The idea of RCM is to eliminate out of focus light by situating a spatial pinhole at the focal point of the lens and to increase the resolution and contrast of the image in addition to the ability to provide in vivo images in the reflection mode. The idea was first proposed in 1957 [38], but it was only after the invention of lasers and computer systems that it quickly found its way in the biomedical community [39] and, recently, in applications, such as skin cancer detection [31]. Depending on the RCM configuration, the specimen is illuminated in a different way. A limited portion of light coming from an infinitesimal spatial sensing volume, which is able to pass through the optical system and spatial pinhole, is detected in the system to form the image. To perform optical sectioning in an in vivo application, the light and filtering system should be scanned over the specimen. A confocal LFI system using a semiconductor laser, such as a VCSEL, can be interpreted as a peculiar embodiment of an RCM system [77, 117, 118, 139–141]. In a confocal LFI system, which works based on the self-mixing effect [8, 10], light emitted from the laser is reflected off a distant target. A small potion of the beam that is reflected back from a very small sensing volume, in a focused beam configuration with a high numerical aperture beam, is able to pass through the optical system and VCSEL's aperture to re-enter the laser cavity. The interference of the reflected and intra-cavity field inside VCSEL's cavity gives rise to a range of perturbations in the operation of the laser, which can be detected by monitoring the laser's output optical power or terminal voltage for sensing purposes. The diameter of the aperture of a typical VCSEL is in the range of a few micrometers up to about 10 micrometers [142], which can be considered as the equivalent of an RCM pinhole in a confocal LFI configuration. Using a high numerical aperture (NA) objective lens is required to have a very small sensing volume, and a laser at a near-infrared optical window guarantees the maximum penetration depth in biological tissues. Figure 5.7 depicts the schematic of a confocal LFI system in an RCM implementation. The detection method in such a peculiar RCM is based on interferometry rather than photomultiplier tubes or avalanche photodiodes in conventional RCMs, and this feature can be exploited to extract the Doppler shift from the signal. The Doppler shift in the frequency of the beam due to the movement of the red blood cells in a living tissue is in the range of a few kilohertz, which is impossible to detect without an interferometric scheme. In Section 5.2.5, further explanations are included about how to extract both confocal reflectance and Doppler signals in an experimental situation.

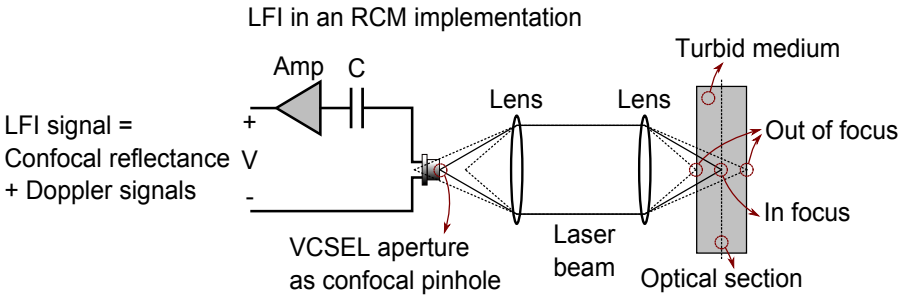

FIGURE 5.7: LFI with an RCM implementation based on a VCSEL as both the emitter and the detector. The VCSEL aperture with a diameter of a few microns acts as the spatial RCM pinhole in this structure, and the LFI signal is generated due to the self-mixing effect inside the VCSEL cavity.

Laser Doppler Flowmetry

Laser Doppler flowmetry has been extensively used in microcirculatory blood flow measurements, as it is a non-invasive method. In laser Doppler perfusion imaging, a collimated laser beam is raster scanned on the skin area of interest to create the perfusion map [16]. The operation of an LDF system is based on the Doppler shift in the frequency of the coherent beam. Photons at wavelengths with a long penetration depth enter the skin tissue and collide with scatterers and chromophores. They will either be scattered or absorbed. The photons that are scattered from moving scatterers, such as RBCs, undergo Doppler shifts. Doppler shift is calculated from the following Equation [51]:

$$\Delta f = \frac{1}{2\pi}(\mathbf{k}_s - \mathbf{k}_i) \cdot \mathbf{v}\,, \tag{5.2}$$

where Δf is the Doppler shift in the photon's frequency, $\mathbf{k}_s$ and $\mathbf{k}_i$ are the wave vectors of the scattered and incident waves, respectively, and $\mathbf{v}$ is the velocity vector of the moving scatterer. From the diffused photons in the turbid skin medium, some of them make their way out of the tissue and return to the detection system of the LDF, which usually involves an interferometric technique and a photodetector to acquire the beat frequency. Perfusion is defined as the product of the average RBCs' velocity and concentration and is proportional to the first moment of the power spectrum of the detected signal [143]:

$$\mathrm{Perf} \propto \int_0^\infty \omega P(\omega) d\omega\,, \tag{5.3}$$

where ω is the angular frequency and $P(\omega)$ is the Doppler power spectrum. By raster scanning the beam on the skin surface, we can create the perfusion map. In our numerical

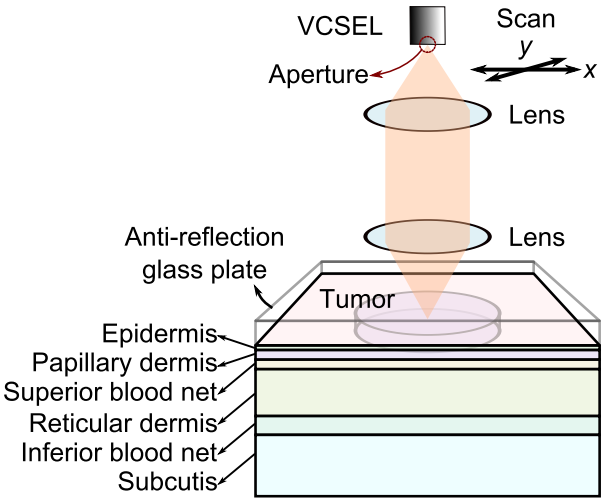

FIGURE 5.8: Block diagram of numerical model including a confocal LDF system raster scanning a six-layer skin tissue model to make the confocal reflectance and Doppler images of an embedded tumour model.

model, we perform this scan by moving the model of the confocal LFI system over the skin model. The schematic of the numerical model is depicted in Figure 5.8. As our numerical model shows, detailed in Section 5.2.3, light is emitted from a simulated 850-nm laser diode and focused on the six-layer skin tissue model. An anti-reflection glass layer is assumed on the top of skin model to reduce specular reflection. A portion of the photons enter the turbid medium of the tissue. Photons will diffuse after interacting with chromophores and scatterers. A portion of the diffused light makes its way out of the tissue and re-enters the laser cavity. Doppler shifted photons, which re-enter the laser cavity, contribute to the Doppler power spectrum. Photon frequencies shift due to collisions with moving RBCs. At each point, we numerically calculated the confocal reflectance signal by counting the number of detected photons, which make their way back into the laser cavity through the optical system and the aperture of the VCSEL; Figure 5.8. At the same point, the Doppler power spectrum is defined as the histogram of the detected photons' Doppler frequency shifts, and perfusion is the first moment of the optical Doppler spectrum calculated from Equation (5.3), which we defined as the Doppler signal in this paper.

In the proposed technique, we can neglect technical difficulties, such as measuring the blood perfusion in absolute value and distinguishing between the contributions of RBC's concentration and velocities to the Doppler signal, which commonly exist in LDF systems [54]. That is because, we are examining the relative values coming from the lesion compared to the surrounding normal area, and there is no need to distinguish

between the concentration and velocity of RBCs, as both of them exist in the tumourous neovascularization and both are indicators of cancer growth.

Monte Carlo Simulation

Monte Carlo is the gold standard in the study of photon-tissue interaction and has been used extensively in the field [18, 144, 145]. In our numerical model, at each scanning site, photons are projected toward the skin tissue, numerically, in a hyperboloid shape to resemble the focused Gaussian beam [61]. We separately executed the simulation for confocal reflectance and Doppler signals with 0.32 and 1.6 million photons, respectively. We defined numerical lenses in the model based on the physical characteristics of commercially available Thorlabs C240TME-B lenses with both a clear aperture diameter and an effective focal length of 8 mm. The features of the numerical lens determine the shape of the focused beam. We assumed the beam diameter at the objective lens is 1.96 mm. This beam diameter along with a 0.5 numerical aperture and 8 mm focal length of the numerical lens result in a beam spot diameter of about 4 m at the focal point. We employed a variance reduction technique when calculating the Doppler signal, in which photons with large Doppler shifts can split into up to 3200 photons [110]. We assumed the wavelength of the photons to be 850 nm, as the water absorption coefficient is almost negligible at this wavelength [146]. As shown in Figure 5.8, we used a six-layer skin model assuming an anti-reflective coating model on the top to avoid specular reflection. We adopted the skin model proposed in the paper of Fredriksson et al., which was validated through their experiments [110]. We assumed the refractive index of the glass plate was close to the skin refractive index to have the index matching. The names and characteristics of the skin layers are listed in Table 5.1. We approximated all of the layers' refractive indices to be 1.4 to avoid index mismatching between the layers [110]. We defined three types of blood components with average velocities of 0.3, 3.0 and 30 mm/s, each present in different volumes within the layers [110]. These low, middle and high velocity blood components can be associated with capillaries, venules (small veins and arterioles) and larger blood vessels. We assumed random RBC directions with a uniform distribution in 3D space. To approximate laminar blood flow, we defined the RBC velocities in a uniform random distribution from zero to two-times the average velocity components [110]. Melanin, as the main absorber of light, exists only in the epidermis layer of healthy skin tissue. Epidermis is the only layer with no blood components. We defined initial absorption and scattering coefficients for each layer and then added the optical properties of melanin and blood components in each layer [110], as listed in the Table 5.1. Blood has absorption and

TABLE 5.1: Six-layer skin tissue model, data from [110].

Layers Top to Bottom	Epidermis	Papillary Dermis	Superior Blood Net	Reticular Dermis	Inferior Blood Net	Subcutis
0.3-mm/s blood concentration (%)	0	0.2	0.6	0.1	0.25	0.1
3.0-mm/s blood concentration (%)	0	0	0.05	0.01	0.035	0.01
30-mm/s blood concentration (%)	0	0	0.001	0.0006	0.006	0.001
Melanin concentration (%)	2.0	0	0	0	0	0
Thickness (mm)	0.075	0.15	0.15	0.8	0.4	2
μ_s bloodless melanin-less (mm^{-1})	23	13	13	13	13	13
μ_a bloodless melanin-less (mm^{-1})	0.1	0.1	0.1	0.1	0.1	0.1
Refractive index	1.4	1.4	1.4	1.4	1.4	1.4

scattering coefficients of 0.5 and 222 mm^{-1}, respectively, and melanin has an absorption coefficient of 15 mm^{-1} and no scattering coefficient. The phase function of a scatterer determines the scattering direction of the photons. Here, all of the non-blood scatterers have a Henyey–Greenstein phase function with an anisotropy factor of 0.85, and RBCs have a Gegenbauer kernel phase function [66] with $\alpha_{\mathrm{Gk}} = 1.0$ and $g_{\mathrm{Gk}} = 0.948$, resulting in an anisotropy factor of 0.991 [110]. We used a variance reduction technique to focus on the Doppler shifted photons [110].

We numerically raster scanned an area of $10 \times 10\ \mathrm{mm}^2$ on the skin tissue model with 30 steps at each side and created 30×30 pixel images. We discussed the photon-tissue interactions in Section 5.2.3, and the configuration can be seen in Figure 5.8. The detected photon population (which determines the confocal reflectance) is the portion of photons that exit from the skin model, pass through the lenses and VCSEL's aperture and return back to the laser cavity. To speed up the numerical calculations, we approximated the radius of the aperture to be 45 µm. Photons move through the lenses based on the ray tracing rules, and the geometry of lens surfaces is derived from the data for C240TME-B.

5.2.4 Simulation Setup and Results

Setup

Tumorous regions in the numerical model are roughly defined as thin cylindrical volumes with diameters of 5 mm and thicknesses of 0.3 mm, laying within the second and third layers of papillary dermis and superior blood net, situated at a depth of 0.075 to 0.375 mm, as illustrated in Figure 5.8. To form the images, we configured the numerical model to keep the focal point of the beam in the middle of the tumour model at the depth of 0.225 mm from the surface. To study the applicability of the technique, we applied it numerically to two typical types of KSC and called them mild KSC (KSC1) and severe

KSC (KSC2). Tumorous abnormalities for these typical types of skin cancer are defined in the simulation as higher RBC concentration and velocities and lower absorption and scattering coefficients.

Stücker et al. used a commercial laser Doppler perfusion imaging device to measure perfusion in different types of skin cancer [12, 13]. They reported increases in the perfusion of BCCs and melanocytic nevi with respect to average healthy skin by factors of approximately 1.8 and 3.8, respectively [12]. In our numerical model, we defined the RBC concentrations of two- and three-times higher than healthy skin for typical KSC1 and KSC2 and RBC velocities of 1.5-times higher than healthy skin for both types. These abnormalities resulted in increases in the perfusion of KSC1 and KSC2 of about 1.7 and 3.7 higher than healthy skin, which we took to be roughly compatible with the data reported in [12] and acceptable for our purposes. On the other hand, Salomatina et al. measured the in vitro optical properties of infiltrative BCC, nodular BCC and invasive SCC in a large spectral range [11]. Their results show remarkable drops in the scattering and absorption coefficients of the tissues affected by these types of KSCs at some wavelengths. For instance, at 850 nm, the scattering and absorption coefficients of nodular BCC and SCC, reduce by factors of about 0.6, all with respect to normal dermis tissue [11]. However, these results are from in vitro measurements, and to apply them to an in vivo model, the effect of blood should be included. These numbers can be quite different for different types of skin cancer. In our numerical model, we assumed the scattering and absorption coefficients to reduce by factors of 0.6 with respect to normal dermis skin tissue for both typical types of KSC1 and KSC2.

To use ex vivo measurement results of tissue optical properties in an in vivo numerical model, we need to add the effect of average blood contents of the tissue to the measured ex vivo optical properties using the following expression [147]:

$$\mu_{\text{in vivo}}(\lambda) = V_{\text{blood}} \times \mu_{\text{b}}(\lambda) + (1 - V_{\text{blood}}) \times \mu_{\text{ex vivo}}(\lambda)\,, \tag{5.4}$$

where $\mu_{\text{in vivo}}$ and $\mu_{\text{ex vivo}}$ are the in vivo and ex vivo optical properties at the wavelength λ, respectively, V_{blood} is the volume fraction of blood in the tissue and μ_{b} is the optical property of blood. We mentioned optical properties of blood and bloodless tissue in Section 5.2.3. The typical average value for the blood volume fraction in the skin layers is about 0.2%, although its value is about 2–5% in the venous plexus [148]. In our numerical model, we used the blood volume fractions given in Table 5.1.

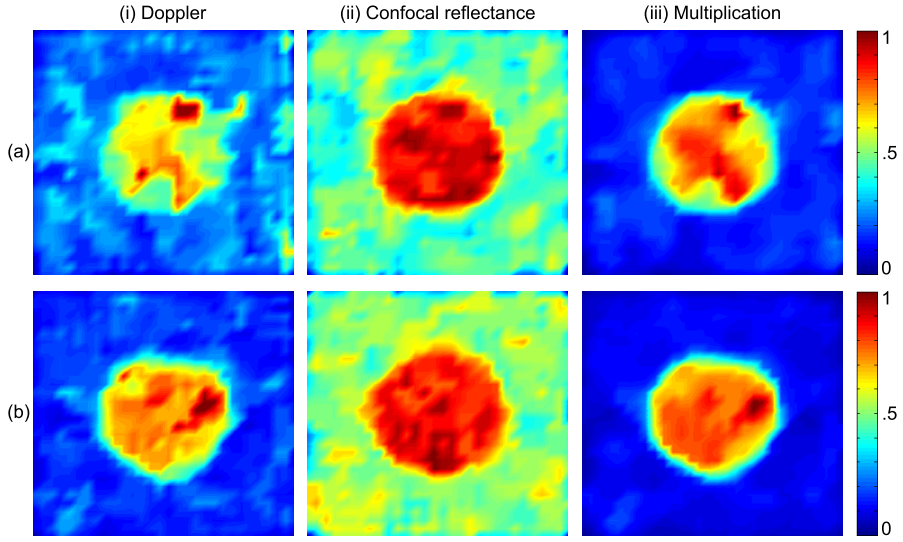

FIGURE 5.9: Monte Carlo simulated images of typical (**a**) KSC1 and (**b**) KSC2. Parts (i) and (ii) of the images depict blood Doppler and confocal reflectance images of 5 mm diameter tumours, respectively. Part (iii) shows the multiplication image, which is formed by multiplying Parts (i) and (ii), pixel-by-pixel.

Results

Parts (i) and (ii) of Figure 5.9a show the simulated Doppler and confocal reflectance images for the typical KSC1, respectively. Furthermore, Parts (i) and (ii) of Figure 5.9b show the simulated Doppler and confocal reflectance images for the typical KSC2, respectively. Part (iii) of Figure 5.9a,b shows the multiplication images. Results are normalized to the peak Doppler and confocal reflectance values, and it can be seen that increasing RBCs' concentration results in higher contrast by comparing Part (i) of Figure 5.9a,b. We filtered all of the images to eliminate spikes using two-dimensional median filtering in MATLAB (R2015a, UQ university liscence, Brisbane, Australia), and all of the values are relative and normalized to arbitrary units.

In order to quantify the numerical results, we defined an SBR parameter as the ratio of the average signal from the tumourous area to the average signal from the normal surrounding skin area obtained from the simulations. This parameter can be formulated as follows:

$$SBR = \frac{\frac{1}{N_{\mathrm{T}}} \sum_{i \in T} Sig_{\mathrm{i}}}{\frac{1}{N_{\mathrm{BG}}} \sum_{i \in BG} Sig_{\mathrm{i}}}, \tag{5.5}$$

where N_T and N_{BG} are the number of pixels in the tumourous and background areas,

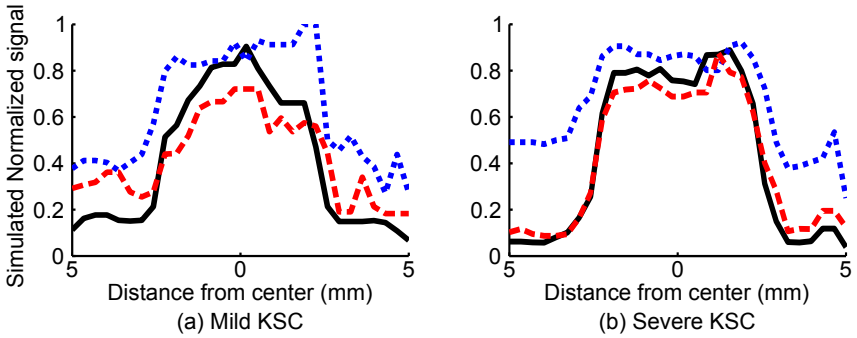

FIGURE 5.10: Improvement in the signal to background ratio as a result of multiplying Doppler flowmetry and confocal reflectance images. Red broken, blue dotted and black solid lines in (**a**) and (**b**) of this image correspond to the Doppler flowmetry, confocal reflectance and multiplication signals acquired along center-crossing horizontal axes in (a) and (b) of Figure 5.9, which correspond to typical KSC1 and KSC2 simulated models, respectively.

respectively, and Sig_i is the signal value at pixel i. Furthermore, T and BG denote the set of pixel indices associated with the tumourous and background areas, respectively. In the case of KSC1 shown in Part (a) of Figure 5.9, the SBR for Doppler, confocal reflectance and multiplication images is 1.4, 1.3 and 2.8, respectively. In the case of KSC2 shown in Part (b) of Figure 5.9, the SBR for Doppler, confocal reflectance and multiplication images is 2.9, 1.2 and 5.0, respectively. As can be inferred from these numbers, the combination of the two techniques is enhancing the SBRs of the images dramatically. The minimum increase factor is about 1.7 in the case of KSC2, which is the ratio of the SBR of the multiplication image to its value for the Doppler image, and in all of the other cases SBRs increase by factors greater than 1.7.

To more clearly see the SBR improvement, we plotted the signals along the center-crossing horizontal axis in Parts (a) and (b) of Figure 5.9 and present these plots in Figure 5.10. Parts (a) and (b) of Figure 5.10 correspond to the simulated models of KSC1 and KSC2, respectively.

5.2.5 Experimental Validation

To examine the feasibility of an experimental device for concurrent RCM and LDF, which is applicable for biomedical imaging purposes, we used a confocal LFI system to image a dynamic turbid medium [149]. The purpose of this experiment is to provide two independent images of confocal reflectance and Doppler flowmetry as a result of a single scan. Images should be able to depict the morphological features and flow characteristics of a dynamic turbid medium at a depth below the surface (where the confocal plane

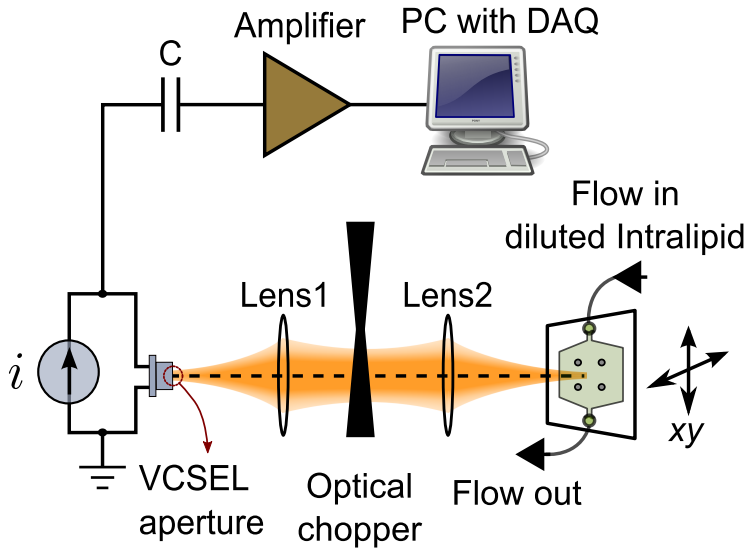

FIGURE 5.11: Experimental confocal LFI apparatus in the dual-modality imaging application, scanning a microfluidic channel containing diluted Intralipid flow.

is situated), which is penetrable to the laser beam, and with respect to a substrate. As we discussed briefly in Subsection 5.2.3, confocal LFI can be considered as a particular embodiment of RCM, which possesses an interferometric nature. It has been used previously to monitor blood perfusion [97] and also in confocal reflectance [117, 118, 141] and Doppler flowmetry [81] imaging systems.

Figure 5.11 shows a schematic of the experimental apparatus we constructed for this purpose. As can be seen and compared in Figures 5.7, 5.8 and 5.11, the suggested experimental setup is based on the concepts of the technique and compatible with the optical system in the numerical model.

Experimental Setup

As illustrated in Figure 5.11, an 850-nm VCSEL operating at 3.55 mA was used in this setup. The beam divergence angle of the VCSEL was about seven degrees, and its temperature was controlled at 35 ℃ to get an optimum signal [122]. The beam was collimated using a lens with a focal length and numerical aperture of 8 mm and 0.5, respectively (Model C240TME-B, Thorlabs, Inc.; Lens 1 in Figure 5.11), and focused using a second lens with a focal length and numerical aperture of 3.1 mm and 0.68, respectively (Model C330TME-B, Thorlabs, Inc.; Lens 2 in Figure 5.11). The second lens had a focal beam spot diameter and Rayleigh length of about 1.8 and 2.9 µm, respectively, which was appropriate for microscopy applications. We need to apply the technique to a

dynamic turbid medium, which is a semi-transparent medium, including both dynamic and static scatterers and absorbers, with a scattering coefficient well above the absorption coefficient. Such a target provides variations in both optical properties and flow distribution, which fits our purpose of dual-modality imaging. Therefore, we chose to use diluted Intralipid flow in a microfluidic channel as an imaging sample. Intralipid is a fat emulsion used as an intravenous nutrient, and its optical properties have been studied before [89]. It has also been used numerously as a phantom for biomedical tissues [150]. We diluted Intralipid 20% with deionized-water with a ratio of 30:1 and pushed it through a microfluidic channel with a channel area of about 8 $\times$ 10 mm^2 and a channel thickness of about 1 mm. The top view of this microfluidic channel can be seen in Figure 5.12a, and also, it is shown in Figure 5.11 as the target. A syringe pump was used to push the mixture with a flow rate of 800 µL/min through the channel. The laser beam was focused at a depth of about 500 µm below the surface of the diluted Intralipid, and the focal plane was kept at this depth throughout the scan. In order to make the images, we used two motorized translation stages (Zaber Technologies Inc.) to move the microfluidic channel vertically and horizontally, to raster scan the laser beam over the channel. An area of 12 $\times$ 12 mm^2 in 61 $\times$ 61 steps, at a 200-µm pitch, was scanned. In the proposed set up, the laser beam is perpendicular to the target, which is different from conventional LDF systems. This geometry is more common in biomedical imaging applications, and the Doppler power spectrum, which is a broadened signal around the frequency of zero, was extracted from the focused part of the beam with a high numerical aperture. At each step of the scan, the LFI signal was acquired from the VCSEL junction voltage and was fed into a 16-bit DAQ card after amplification. The time domain voltage signal was sampled at a rate of 60 kS/s, and 3 kS was used as the signal time sequence, which corresponds to 50 ms. To convert the time domain signal into the frequency domain, we applied fast Fourier transform to the time sequence and used a Savitzky–Golay filter in MATLAB (R2015a, UQ university liscence, Brisbane, Australia) to filter out the frequency domain signal.

Because semiconductor lasers are noisy at DC or low frequencies [122], we AC-coupled the VCSEL junction voltage when amplifying it. Therefore, we needed to modulate the laser beam to extract the confocal reflectance signal. As can be see in Figure 5.11, we used an optical chopper to modulate the beam at the frequency of 1 kHz. Modulating the beam created two different levels of feedback, which was then detected and used to quantify the level of reflection [125].

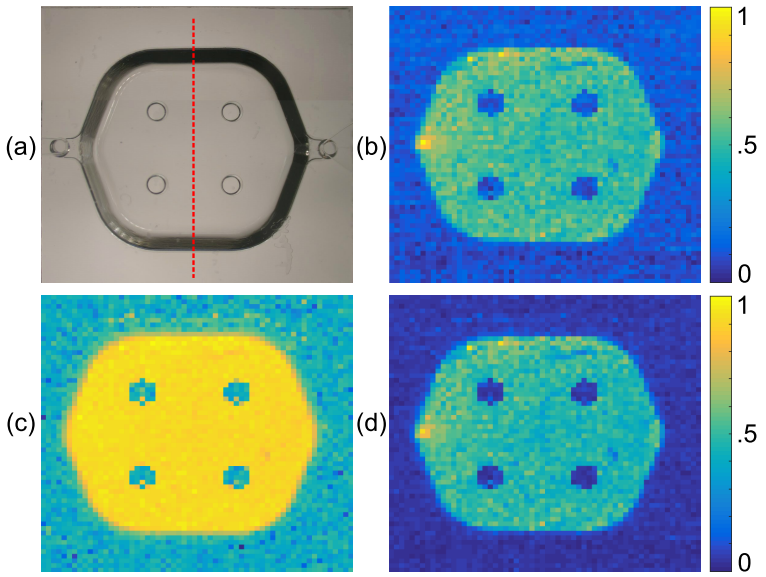

FIGURE 5.12: (**a**) Top view of the microfluidic channel (the red broken line shows the center-crossing axis alone which SBR was calculated) and experimental normalized (**b**) Doppler flowmetry, (**c**) confocal reflectance and (**d**) multiplication images.

Experimental Results

Scan results are illustrated in Figure 5.12. Doppler flowmetry, confocal reflectance and multiplication images are shown in Figure 5.12b–d, respectively. There are four pillars situated in the middle of the microfluidic channel by the manufacturer for stability purposes, which can be seen as four dots at the noise level in all of the images in Figure 5.12. Doppler flow distribution, depicted in (b), has the highest flow rate at the input of the channel on the left side of it. Confocal reflectance distribution, depicted in (c), has an even distribution all over the channel, as expected, because the optical properties of the turbid medium are maintained constant throughout the volume. The background noise level (signal from the outside of the channel area) is higher in (c) compared to (b), as there is a small amount of reflection from the surface of the microfluidic channel, although the surface is not at the focal plane, which is higher than the background noise in (b) (which is the overall rise in the Doppler spectrum in the absence of flow due to noises). The multiplication image, (d) of Figure 5.12, is made by multiplying (b) and (c), pixel-by-pixel. It can be noticed from (d) that the background noise is reduced in the multiplication image. Similar to what we did in the case of the numerical model in Section 5.2.4, we quantified the improvement in the contrast of the multiplication image by defining an SBR parameter similar to the way we defined it in Equation 5.5, as the average level of the signal from the flow area to the average level of the signal outside the flow area, along

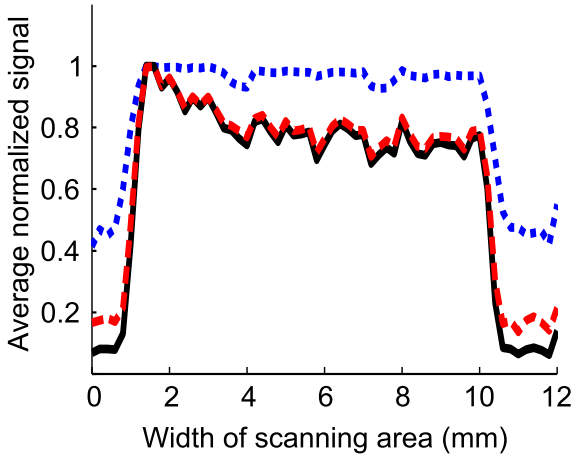

FIGURE 5.13: Red broken, blue dotted and black solid lines show average Doppler flowmetry, confocal reflectance and multiplication signals, acquired along the center-crossing axis of the microfluidic channel (shown with the red broken line in Figure 5.12a), respectively.

a center-crossing axis shown by a red broken line in Figure 5.12a. Average Doppler flowmetry, confocal reflectance and multiplication signals, acquired along the red broken line in Figure 5.12a, are shown in Figure 5.13. It is clear from this image that multiplication signal (black solid line) has a lower noise level (at left and right wings) compared to the other two signals. SBR for Doppler flowmetry, confocal reflectance and multiplication signals is 4.1, 1.9 and 7.2, respectively. SBR of the multiplication signal is improved by factors of 1.8 and 3.7 with respect to Doppler flowmetry and confocal reflectance signals, respectively. Therefore, the minimum improvement factor for SBR in the experimental result is 1.8, which is consistent with the figure for the numerical model, which was 1.7. This shows good agreement between experimental and numerical results.

The Doppler flowmetry and confocal reflectance parts of the LFI signal can be extracted from both the frequency (fast Fourier transformation of time domain signal) or the time domain signals. In order to show how the signal is processed to get both parts of the data out of it, frequency and time domain signals, acquired at a typical point inside the flow area, are shown in (a) and (b) of Figure 5.14, respectively. The red broken and black solid lines in (a) are the filtered Doppler spectrum (Savitzky–Golay filter) and the noise floor, respectively. Doppler flowmetry and confocal reflectance signals were calculated in the frequency domain by applying the filtered Doppler spectrum to Equation (5.3) and measuring the magnitude of the first harmonic (as the signal was modulated at 1 kHz) with respect to the noise floor, respectively. On the other hand, one can look at the level of fluctuations in the time domain (when the beam is not blocked by the chopper) and the

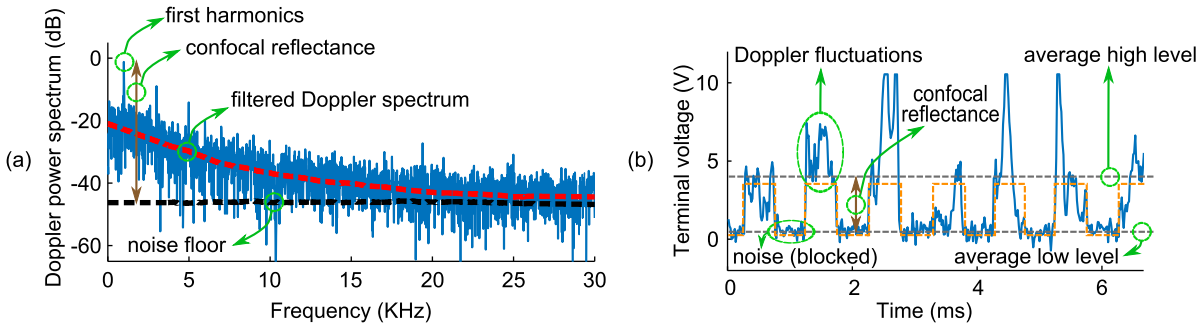

FIGURE 5.14: (**a**) Frequency and (**b**) time domain confocal LFI signals, obtained from the voltage of the VCSEL terminals. Red and black broken lines in (**a**) show the filtered Doppler spectrum and noise floor (in the absence of target), and the first large spike in (**a**) is the first harmonic of the signal (as the beam is modulated at 1 kHz); its magnitude with respect to noise floor is a measure of the confocal reflectance signal. The orange broken line in (**b**) shows the modulating signal at 1 kHz, and two grey broken lines show the average high and low time domain signals corresponding to the unblocked and blocked modes of the beam (by means of the optical chopper), respectively, indicating confocal reflectance. Doppler fluctuation can be seen on the high level of the time domain signal when the beam is not blocked.

difference between the average low and high levels of modulated signal, corresponding to the blocked and unblocked modes of the beam, to extract Doppler flowmetry and confocal reflectance signals. Figure 5.14 shows all of the aforementioned annotations. As can be seen in Figure 5.14, the Doppler spectrum is a broadened spectrum around the frequency of zero, because the beam in the suggested confocal LFI apparatus is normal to the flow. This configuration in conjunction with a high numerical aperture objective lens resulted in a broadened spectrum that was used in this work to extract Doppler flowmetry or the perfusion signal.

5.2.6 Discussion

We investigated and characterized the proposed imaging technique by applying it numerically to two typical types of tumourous skin as mild and severe KSCs (KSC1 and KSC2) in this work. We derived the optical properties of KSCs from the literature and take into account the lowest level of changes in the optical scattering and absorption coefficients of the tumours in our simulations [11, 12], in order to focus on the improvement in the sensitivity of the proposed technique. Malignant melanomas, which is not included in the numerical models in this article, have different shapes, relative locations in the skin tissue, alterations in optical properties, etc., compared to those of KSCs. It has been reported that total reflectance is generally reduced with the increase in the degree of malignancy

in the pigmented skin lesions in wide spectral ranges [151–155]. As can be seen in Figure 5.9, contrast in the multiplication images increases with the disease in severity, from KSC1 to KSC2. The increase in the scattering and absorption coefficients of malignant melanoma with respect to common nevi has also been reported [156, 157]. A reason for the increase of the scattering coefficient with malignancy in skin lesions could be the increase in nuclear to cell volume with the degree of malignancy in tumourous cells [158]; as in the case of cervical carcinoma, the increase in nuclear to cell volume is a well-known cytological indicator of the tumour malignancy [159].

The reduction in total reflectance can be attributed to a decrease in the ratio of μ_s'/μ_a of the tumourous tissue. This means that higher absorption or lower scattering coefficients in skin tissue are expected to reduce the total reflectance. Therefore, the total reflectance level is more properly determined by considering the combination of optical properties. The total reflectance approximation formula derived from diffusion theory for a semi-infinite turbid medium has the following form [153]:

$$R_p = \frac{1}{k_1 \frac{1}{\mu_s'} + k_2 \frac{\mu_a}{\mu_s'}}\,, \tag{5.6}$$

where R_p is the detected portion of the total reflectance, μ_a and μ_s' are the absorption and reduced scattering coefficients, respectively, and k_1 and k_2 are empirical parameters coming from the optical geometry of the setup. Figure 5.15 shows a comparison between the total reflectance against μ_s'/μ_a, from Equation (5.6) and our Monte Carlo skin model, described in Subsection 5.2.3. As can be seen, there is good agreement between the analytic formula and the Monte Carlo simulation. We assumed k_1 and k_2 of the optical system model to be three and one, respectively, and the anisotropy factor to be 0.85 in the analytic formula. The Monte Carlo simulation in Figure 5.15 is performed by keeping the absorption coefficients of each layer as they are and sweeping the reduced scattering coefficients. We assumed an anisotropy factor of 0.85 in the Monte Carlo simulation, as well.

We defined an SBR parameter as a touchstone to quantify the improvement in the sensitivity of the technique. Both simulation and experimental results concluded that combining two modalities increases the sensitivity dramatically. Numerical SBR values presented in Section 5.2.4 show that the ratios of multiplication SBRs to Doppler flowmetry SBRs increase by factors of 2.0 and 1.7, and the ratios of multiplication SBRs to confocal reflectance SBRs increase by factors of 2.2 and 4.2 for typical KSC1 and KSC2, respectively. In a similar way, experimental SBR values presented in Subsection 5.2.5 show that the ratio of multiplication SBR to Doppler flowmetry and confocal reflectance SBRs

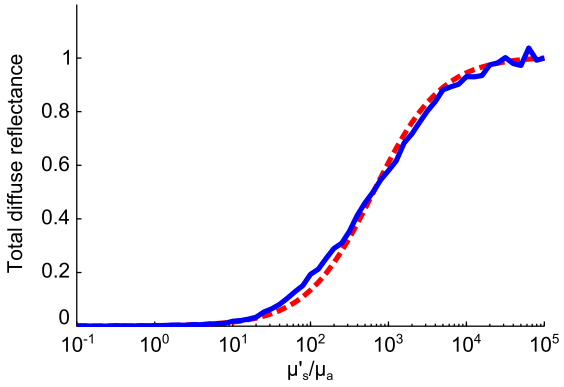

FIGURE 5.15: Simulated total reflectance from a typical tumourous skin model in our model (blue line) compared to the diffusion theory formula (red broken line), versus the ratio of the reduced scattering coefficient to absorption coefficient.

increase by factors of 1.8 and 3.7 for the microfluidic setup, respectively. Depending on the concentration of the dynamic turbid medium used in the experiment, SBRs have similar trends as the values obtained from numerical models, which shows the consistency between simulations and experiment.

Skin neoplastic diseases often develop from pre-existing skin lesions [160]. Actinic keratoses and dysplastic nevi are the most important precursors to SCCs and melanomas, respectively [160]. The sizes of actinic keratosis lesions are usually 1–3 mm, but can be up to several centimetres [161], as well, and the sizes of dysplastic nevi are mostly larger than 5 mm [160]. Hence, we assumed that the sizes of the tumourous tissues are 5 mm in diameter in our numerical models. BCC and SCC are different histopathologically, and the origin cells of sporadic BCCs are less well defined; there are not any well-known precursors to them [162].

Our assumptions in defining the geometry, location and properties of tumour models include generalization to make the study of the proposed technique easier. For instance, seborrhoeic keratosis, as probably the most common benign KSC, is different from SCC and BCC histopathologically. It usually occurs just as a thickened epidermis and no extension into the dermis layer, but still may rarely mimic KSC or MM clinically. Moreover, KSC can be thought of in the context of a field cancerization model. Therefore, care should be taken in determining where the healthy tissue is. Field cancerization theory states that there is a genomically-unstable area around the primary tumour, inclined to aberrant growth [163, 164]. Neovascularization as an abnormal growth requirement happens mainly in the primary neoplastic tissue. Therefore, the area around the primary tumour is called healthy tissue in this paper. In melanoma, the suspect lesion is pigmented, and it

is easier to distinguish the perilesional skin area.

Some obstacles to early skin cancer detection are the large skin surface area and its susceptibility to other types of skin lesions that can resemble a type of skin cancer, which are hard to differentiate. For example, differentiating between melanoma and dysplastic nevi is challenging clinically and histopathologically [28]. Optical properties [155] and perfusion [13] of dysplastic nevi have been studied, and it is shown that melanoma has higher perfusion and lower reflectance compared to dysplastic nevi. We are including both of these modalities in our method, and this combination can increase the specificity of detection. A higher concentration of RBCs changes the optical properties of the skin, as blood has a high scattering coefficient, and the out-flow of fluid and cells from the walls of leaky newly-developed venules [56] is another reason for the distorted optical properties. Examining the morphology and flow direction of these newly-developed venules also has the potential of discriminating between non-pigmented neoplastic skin lesions and assessing their degree of malignancy [165].

Our proposed technique implemented in a hardware platform would afford a non-invasive, in vivo and non-contact skin investigation tool with high spatial resolution (as the focused beam in the experiment has a $1/e^2$ power beam spot diameter of about 1.8 µm). Optical properties of human skin can vary greatly in different places of the body and between individuals, and it will affect both the confocal reflectance and Doppler flowmetry signals greatly. One advantage of our technique is that it focuses on changes relative to surrounding tissue. Therefore, there is no need for calibration or measurement of absolute values. In addition to early detection, this technique could also be useful in differentiating different types of skin tumours by quantifying the level of neovascularization and optical property distortions, estimating the stage of tumourous development and the rate of growth by monitoring and delineating a tumour's border for proper removal surgery [166].

Furthermore, care should be taken about the safe level of the laser beam optical power, and power should be limited by factors, such as the hazard of tissue damage and skin sensitivity [167]. Most of the commercially available laser scanning confocal microscopes use in-plane laser diodes with tens of mW of power [5] to achieve a signal to noise ratio that is detectable by the photodetector in a direct detection scheme; while our scheme uses a heterodyne detection scheme, in which a low power reflected signal mixes with strong intra-cavity fields (fields within the VCSEL's cavity). In such a system, the sensitivity is so high, that the signal is detectable when laser operates at currents just above the threshold, and the output power is less than 100 µW. Such a low power system is not only safe, but also has the minimum effect on the optical properties and the structure of biological tissues.

5.2.7 Conclusion

Cancer is the result of complex interactions between environmental and genetic factors. Cancer incidence is growing each year, and early detection can save many lives and reduce the burden of disease. One way to develop a robust early detection method is to include all of the possible potential cancer indicators in the detection system. We suggest modulating the laser beam in a confocal LFI system to measure confocal reflectance at the same time as it measures the Doppler flowmetry signal. This results in a new imaging technique of simultaneous probing for two abnormal cancer biological traits of distorted tissue optical properties and perfusion. It can improve the capabilities of the currently existing systems, which use only one of these modalities, through improving the sensitivity and specificity. We examined this technique through a range of numerical simulations and conducted an experiment to image a dynamic turbid medium. Simulated and experimental results showed a high degree of consistency, which validates the technique. We also quantified the results by defining an SBR parameter as the ratio of the signal from the tumourous (or dynamic turbid) area to the signal from the background area. The signal to background ratio of the combined images has increased remarkably in both simulated and experimental examinations with similar trends, which indicates the enhanced sensitivity of the technique.

Chapter 6

6. Laser Feedback Tomography and Tumorous Skin Phantoms

One of the features of the LFI imaging system that we implicitly relied upon throughout this work was that it can perform optical sectioning or provide cross-sectional images of samples. That is because in the setups we are using high NA lenses to focus the beam within the sample. This characteristic gives us the ability to make tomographic images as we can take numerous images of the sample and reconstruct a three-dimensional image of the interior features of the sample. Tomography is usually preferred to single-slice imaging among the medical community in diagnostic and therapeutic applications. The reason for this is that it illustrates the geometrical features and morphological aspects of the sample in a three-dimensional space and in many cases it presents a better visualization of the interior of the sample and a better comparison of slices relative to each other becomes possible.

This chapter includes paper F and section 6.2. In paper F for the first time, application of LFI in skin cancer detection has been investigated in a reflectance imaging configuration and using an agar three-layer cancerous skin tissue model. In this paper optical sectioning has been performed by moving the optical system toward the sample at physical lengths of 100 µm. The feasibility of optical sectioning is studied and the same structure (optical system and agar tissue phantom) is modeled using Monte Carlo simulation. Simulated results are consistent with the experimental results and this study paves the way for a laser feedback tomography system.

Section 6.2 proposes the use of confocal laser feedback tomography for non-invasive cross-sectional imaging of soft biological tissues. This is a manifestation of a compact system which uses a VCSEL as both transmitter and receiver of the beam and possesses

the imaging power of a confocal microscope. We used three different silicone-based phantoms of keratinocyte skin cancer tissue to examine the technique. Cancerous regions were introduced to the phantoms as macro-structural changes in the optical properties of dermis layer. Moreover, Monte Carlo simulation of the same optical system and tissue phantoms was conducted, which in tandem with experimental results shows the feasibility of a sensitive tomography system to be used for the application of skin cancer detection. The results presented in this section will be submitted for publication.

6.1 Paper F

Mowla, Alireza and Taimre, Thomas and Lim, Yah L and Bertling, Karl and Wilson, Stephen J and Prow, Tarl W and Soyer, H Peter and Rakić, Aleksandar D, "Diffuse reflectance imaging for non-melanoma skin cancer detection using laser feedback interferometry," International Society for Optics and Photonics, SPIE Photonics Europe, Brussels, Belgium 98870T–98870T (2016).

6.1.1 Abstract

We propose a compact, self-aligned, low-cost, and versatile infrared diffuse-reflectance laser imaging system using a laser feedback interferometry technique with possible applications in *in vivo* biological tissue imaging and skin cancer detection. We examine the proposed technique experimentally using a three-layer agar skin phantom. A cylindrical region with a scattering rate lower than that of the surrounding normal tissue was used as a model for a non-melanoma skin tumour. The same structure was implemented in a Monte Carlo computational model. The experimental results agree well with the Monte Carlo simulations validating the theoretical basis of the technique. Results prove the applicability of the proposed technique for biological tissue imaging, with the capability of depth sectioning and a penetration depth of well over 1.2 mm into the skin phantom.

6.1.2 Introduction

The low electromagnetic absorption of water and hemoglobin in the near-infrared spectrum has made this spectral region optimal for non-invasive *in vivo* optical interrogation of biological tissues for diagnostic purposes [168]. In the past few decades an extended range of non-invasive optical techniques, using this spectral window, have been suggested and developed to be used for non-melanoma skin cancer (NMSC), also known as keratinocyte skin cancer (KSC)[1], detection. Diffuse reflectance spectroscopy has been used to determine the *in vivo* optical properties (scattering and absorption coefficients) of KSCs for diagnostics, showing that KSCs altered the optical properties of skin tissue [157]. On the other hand, *in vitro* measurement of these properties is more easily

[1]KSC and NMSC can be used interchangeably and both encompass basal cell carcinoma and squamous cell carcinoma.

carried out and has been measured using spectrophotometers in combination with integrating spheres to look at the diffuse reflectance and total transmittance of light in biopsy samples [88]. Reduction in scattering and absorption coefficients have also been reported in KSCs, by *in vitro* measurement of diffuse reflectance and total transmittance of cancerous samples [11].

Most biological tissues are highly scattering over the near-infrared spectral window and light will diffuse quickly as soon as it enters the tissue [169]. Therefore, optical properties of a biological tissue can be investigated by monitoring the diffuse reflectance of light from the tissue and can also be analyzed to distinguish between tumorigenic and nontumorigenic cells [170]. Detecting diffuse reflectance to measure *in vivo* optical properties of a biological sample has usually been achieved by illuminating a larger area on the tissue using an optical source and looking at the reflectance by means of a charge-coupled device camera [171], or by transmitting light into the tissue using an optical fiber and collecting the reflected light using an arrangement of other optical fibers located near the source fiber [172], or by focusing a beam on the biological tissue and collecting the reflected light in a confocal detection scheme [31, 173, 174]. We propose a new technique based on the latter scheme which can be used in *in vivo* measurement of diffuse reflectance in the near-infrared range.

The technique proposed here is a laser feedback interferometry (LFI) system (based on self-mixing effect [9,10,71]) in a confocal laser feedback configuration [77,118]. In this system a near-infrared laser diode acts as both transmitter and receiver of the optical signal. The illuminating laser beam is focused on a target. A portion of the diffuse reflected light makes its way back into the laser cavity and affects the intra-cavity optical field. When the laser beam is modulated appropriately, these changes in the intra-cavity optical field due to diffuse reflected light can be measured. The focused beam is then raster scanned over the target yielding a spatially resolved image of the diffuse reflectance.

To examine the technique we applied it to two models: (1) a physical skin phantom and (2) a numerical model using Monte Carlo (MC) simulation. The physical model was a simple three-layer agar gel skin phantom containing a cylindrical 4 mm diameter region (representing a KSC). The tumorous region was included in the second layer which resembled dermis and the diameter size was in the range of a typical skin tumorous lesion [160,161]. This model was based on an approximate geometry for a typical skin with typical optical properties [131] and lower scattering coefficient in the tumorous area as it was reported by Salomatina *et al.* [11]. The numerical model was a MC photon transport model, mimicking the physical skin phantom and the geometry of the experimental set up.

The paper is structured as follows: we discuss the fundamentals of LFI in Sec. 6.1.3.

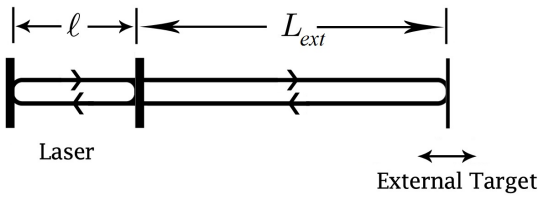

FIGURE 6.1: Three mirror model of laser in the presence of external target.

Skin phantom preparation procedure is presented in Sec. 6.1.4 and details about the experiment are outlined in Sec. 6.1.5. Experimental results are presented in Sec. 6.1.6 which is followed by MC simulation results in Sec. 6.1.7. Finally, we conclude in Sec. 6.1.8.

6.1.3 Laser Feedback Interferometry

Laser feedback interferometry works based on the self-mixing effect [9, 10, 71]. Self-mixing effect occurs when light emitted from the laser is reflected off a distant target and is reinjected into the laser cavity which perturbs the operation of the laser. This perturbation can contain information of interest relating to the target.

One way to study the self-mixing effect is to assume a three-mirror model instead of a conventional two-mirror model to examine the laser resonator cavity operation in the presence of an external target which can be defined as the third mirror. A schematic diagram of this model can be seen in Fig. 6.1. In this figure, l is the laser cavity length and L_{ext} is the distance between the exit mirror of the laser and the target. Lasing conditions in a free running laser (two-mirror model) are for the beam to have the same phase and unit gain coefficient after one round trip between the mirrors. When there is an external target in the vicinity of the laser so that a portion of the beam reflects back into the cavity, parameters of the laser are perturbed. In particular, the frequency of the free running laser shifts in order to maintain a modified phase condition for the new situation. The shift in the frequency has to satisfy the following modified phase equation (at timescales far slower than that of the internal laser dynamics) [74]:

$$0 = 2\pi\tau_{\text{ext}}(\nu - \nu_0) + C\sin(2\pi\nu\tau_{\text{ext}} + \arctan\alpha)\,, \tag{6.1}$$

where τ_{ext} is the external round-trip time, ν is the frequency of the laser with optical feedback, ν_0 is the frequency of the free running laser in the absence of the external target, C is the feedback parameter which depends on the level of optical feedback [75], and α is

the linewidth enhancement factor [76]. The equation for the feedback parameter C is as follows [74]:

$$C = \frac{\tau_{\text{ext}}}{\tau_\ell}\,\kappa_{\text{ext}}\,\sqrt{1+\alpha^2}\,, \tag{6.2}$$

where τ_ℓ is the intra-cavity round-trip time, and κ_{ext} is the coupling coefficient which is a function of reflectivity of the target and exit laser mirror as follows [74]:

$$\kappa_{\text{ext}} = \varepsilon\,\sqrt{\frac{R_{\text{ext}}}{R_s}}\,\left(1-R_s\right)\,, \tag{6.3}$$

where ε is the fraction of the reflected beam which coherently coupled back into the lasing mode [75], and R_{ext} and R_s are the reflectivities of the target and exit laser mirror, respectively. By defining the external round-trip phase in the presence of the target as $\phi = 2\pi\nu\tau_{\text{ext}}$ and external round-trip phase in the absence of the target as $\phi_0 = 2\pi\nu_0\tau_{\text{ext}}$, Eq. (6.1) can be written in the following form [74]:

$$0 = \phi - \phi_0 + C\sin(\phi + \arctan\alpha)\,. \tag{6.4}$$

Solving Eq. (6.4) for ϕ is not trivial as there is no closed-form solution for it. After solving this equation numerically, perturbation in the threshold gain of the laser due to the optical feedback can be formulated as [74]:

$$\Delta g_{\text{th}} = -\frac{\kappa_{\text{ext}}}{L}\cos(\phi)\,, \tag{6.5}$$

where L is the target distance from the laser. The variations in g_{th} can then cause an observable fluctuation in the laser optical power which is caused by the changes in the external round-trip phase in the presence of a target, as:

$$\Delta P = \beta\cos(\phi)\,, \tag{6.6}$$

where β is the amplitude of self-mixing signal which is dependent on the laser and system parameters (such as the amount of light being coupled back into the laser cavity, the distance to the target, and the photon lifetime in the laser cavity). The characteristics of the external target can then be sensed by monitoring the changes in the optical output power of the laser or changes in the terminal voltage of the laser [77]. In this paper we used a vertical cavity surface emitting laser (VCSEL) and measured the laser terminal voltage, from which we derive our self-mixing signal. [119]. Therefore, the proposed LFI system is compact and low-cost as VCSELs can be provided in small dimensions and

inexpensively.

6.1.4 Skin Phantom

Optical properties of human skin have been studied extensively for the purposes of diagnosis, treatment, and improved understanding of health and disease mechanisms [88, 131]. Human skin consists of three main layers: epidermis, dermis, and subcutaneous tissue. Epidermis contains mostly keratinocytes and no blood vessels though it does contain melanocytes as well. Melanocytes are the melanin producing cells. Melanin is a pigment which is the main absorber of light and is located above the nuclei of keratinocytes along the epidermal basal cell layer protecting the nuclear DNA from harmful ultra-violet irradiation. Dermis contains blood vessels, lymphatics, nerves, and two types of fibers: collagen and elastic fibers. Dermis is an optically turbid medium with a scattering coefficient much higher than its absorption coefficient as it normally does not contain any melanin [175] and it is also much thicker than epidermis. Subcutaneous tissue is the lowermost layer of the human skin which mainly consists of fat cells.

Agar is a matrix hydrogel material consists of a network of hydrophilic polymers. It is mainly made up of water and is a biologically and biochemically compatible material which has already been used as tissue phantoms [85, 150]. Agar gel has innate optical properties which depend on the purity and concentration of the agar powder in the gel. Scattering and absorption coefficients of a pure agar gel are usually low and to control the scattering and absorption coefficients of the agar gel in a phantom, materials to specifically modify the scattering and absorption must be added to the agar gel. We added titanium dioxide (TiO_2) and instant coffee to the agar gel to control its optical properties. Titanium dioxide powder is widely accepted as a scatterer in the near-infrared range [85] which is inexpensive and safe. Instant coffee can also be used as a good absorber of light in this frequency range [176].

The agar skin tissue phantom in this paper contained three layers. Figure 2 illustrates steps in making the agar gel skin phantom. All the layers were placed on a 150 μm thick cover slip individually. This cover slip on the top of the agar tissue phantom stopped agar from evaporation and held the sample relatively static. In Fig. 6.2(a) the outermost layer which was a 500 μm thick 1.2% weight to weight (w/w) agar gel doped with 1.2% w/w instant coffee powder was placed on the cover slip. This layer resembled epidermis (although epidermis is usually between 80 to 120 μm thick, to avoid complexity in making such a thin agar layer, we approximated this layer to be 500 μm) which is high in melanin concentration. Fig. 6.2(b) shows the second layer which was a 1000 μm thick 1.2% w/w

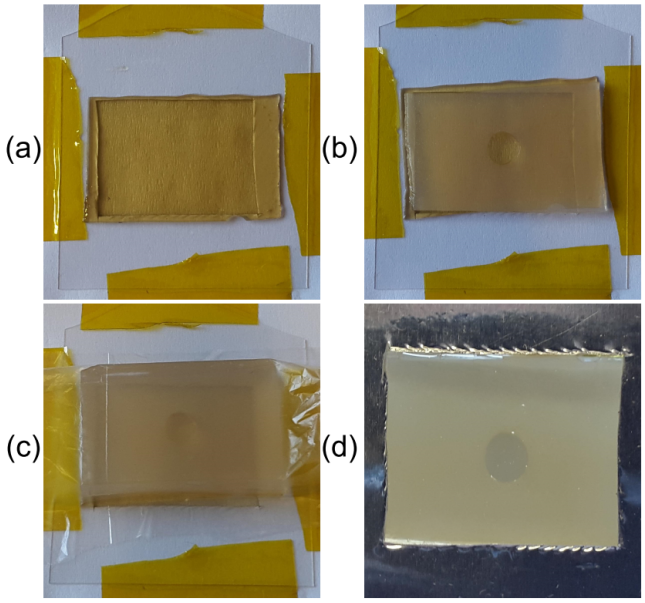

FIGURE 6.2: Agar skin tissue phantom; (a) a high absorptive 500 μm layer on a 150 μm thick cover slip resembling the epidermis, (b) a high scattering 1000 μm layer enclosing a 4 mm diameter cylindrical lower scattering tumorous model as the equivalent of dermis, (c) 3.15 mm pure agar layer resembling the subcutaneous tissue and a plastic wrap, (d) top view of the skin phantom.

agar gel doped with about 0.1% w/w TiO_2 powder on top of the first layer. This layer had a high scattering feature and it resembled dermis which is highly scattering. We punched out a 4 mm diameter cylindrical area in the middle of this layer and replaced it with a 4 mm diameter cylindrical layer made up of pure 1.2% w/w agar gel with the same thickness of 1000 μm, to approximately resemble a KSC area. Based on our measurements in this section, the scattering coefficient of this cancerous area is about 0.3 of the scattering coefficient of the surrounding second layer. This typical drop factor in the scattering coefficient of the cancerous area is consistent with the measured drops in the scattering coefficients of three type of KSCs, which are reported to be about 0.5, 0.03, and 0.005 for infiltrative basal cell carcinoma, nodular basal cell carcinoma, and squamous cell carcinoma, respectively, at the wavelength of 850 nm, with respect to that of a healthy dermis [11]. Third layer was a thicker pure agar gel layer which resembled subcutaneous tissue with relatively lower scattering and absorption coefficients. Fig. 6.2(c) shows the third layer which was a 3.15 mm thick pure 1.2% w/w agar gel on top of the second layer. We wrapped the bottom side with a piece of plastic to stop agar from evaporating and make the sample more stable. Finally the top view of the sample is shown in Fig. 6.2(d).

The agar gel was prepared by dissolving the w/w proportion of the agar powder in distilled water. The mixture was then placed in a microwave oven and heated up to the

boiling point to start the polymerization process. The mixture was removed from the microwave oven as soon as it reached the boiling point and was stirred well manually for a few minutes. Instant coffee was added to the mixture according to the desired w/w proportion. Instant coffee was very soluble in the hot mixture and was easily dissolved by stirring. Titanium dioxide in powdered form was added to the agar gel mixture as desired according to w/w proportion. Dissolving TiO_2 uniformly in the agar gel was not trivial as it was a metal oxide powder which was heavy and precipitated quickly if not stirred well. It resided in the agar gel in suspension before the gel was set and constant stirring for about 30 minutes was needed to avoid deposition and remaining in a clumpy powder form [85]. The mixture was also kept hot during the stirring process. To make a agar gel layer with specific thickness, we poured the prepared agar mixture into a Petri dish containing two microscope slides which were separated by two spacers at the ends with specific thickness as desired. The hot agar mixture spread between the two microscope slides and when solidified a layer with the required thickness was obtained.

To estimate the optical properties of the prepared layers. The agar gel layer, doped with different levels of absorber and scatterer, was illuminated with a collimated laser beam at 850 nm. Power of the collimated laser beam was recorded before and after passing through the sample. Based on the Beer–Lambert law, the total attenuation of light traveling in a transparent material depends on its optical properties, and can be described as:

$$\mu_t = -\frac{1}{L} \ln \frac{P}{P_0} \,, \tag{6.7}$$

where μ_t is the total attenuation of the light, L is the agar sample thickness, P is the power of the transmitted light, and P_0 is the power of the non-attenuated light. The total attenuation can also be formulated as:

$$\mu_t = \mu_{a_{\mathrm{sam}}} + \mu_{s_{\mathrm{sam}}} \,, \tag{6.8}$$

where $\mu_{a_{\mathrm{sam}}}$ and $\mu_{s_{\mathrm{sam}}}$ are the absorption and scattering coefficients of the sample, respectively. Optical properties of the sample can be a combination of the optical properties of the base gel and additive absorbers and scatterers based on their concentrations. In this work instant coffee and TiO_2 were used as the main absorber and scatterer. Therefore, the absorption and scattering coefficients of the sample can be written respectively as:

$$\mu_{a_{\mathrm{sam}}} = \mu_{a_{\mathrm{agar}}} \times C_{\mathrm{agar}} + \mu_{a_{\mathrm{coffee}}} \times C_{\mathrm{coffee}} \,, \tag{6.9}$$

and:

$$\mu_{s_{\rm sam}} = \mu_{s_{\rm agar}} \times C_{\rm agar} + \mu_{s_{\rm TiO2}} \times C_{\rm TiO2}\,, \tag{6.10}$$

where $\mu_{a_{\rm agar}}$ and $\mu_{a_{\rm coffee}}$ are the absorption coefficients of the agar powder and instant coffee, respectively, $C_{\rm agar}$ and $C_{\rm coffee}$ are the concentrations (volume proportion) of the agar powder and instant coffee, respectively, $\mu_{s_{\rm agar}}$ and $\mu_{s_{\rm TiO2}}$ are the scattering coefficients of the agar powder and TiO_2, respectively, and $C_{\rm TiO2}$ is the concentration (volume proportion) of TiO_2 powder in the gel.

We used a collimated laser beam at 850 nm to measure the optical properties of the samples and estimated the absorption coefficient of the pure 1.2% w/w agar gel to be equal to that of water which is also consistent with the literature [150] and was a start point for our measurements. This means we approximated $C_{\rm agar}$ to be about 0.01 for a 1.2% w/w agar gel and we took $\mu_{a_{\rm agar}}$ to be 50 $\rm m^{-1}$. After applying the technique to the pure agar gel, we measured the total attenuation μ_t to be 66.35 $\rm m^{-1}$ and considering the formula in the previous paragraph, $66.35 = 50 \times 0.01 + \mu_{s_{\rm agar}} \times 0.01$, $\mu_{s_{\rm agar}}$ was calculated to be 6585 $\rm m^{-1}$. After calculating $\mu_{a_{\rm agar}}$ and $\mu_{s_{\rm agar}}$ for pure agar powder, we were able to calculate the $\mu_{a_{\rm coffee}}$ and $\mu_{s_{\rm TiO2}}$ for pure instant coffee and TiO_2 powders as well, which were calculated to be 19948 and 142950 $\rm m^{-1}$, respectively. For this calculations we considered $C_{\rm coffee}$ and $C_{\rm TiO2}$ to be roughly 0.01 and 0.001 for 1.2% w/w instant coffee and 0.1% w/w TiO_2 agar gel samples, respectively. We assumed the refractive index of the samples to be equal to that for the water which is about 1.35 at 850 nm. The value for parameters as calculated in this part will be used in Sec. 6.1.7 to perform MC simulations.

6.1.5 Experiments

The experimental set up can be seen in Fig. 6.3. In this set up, we used an 850 nm VCSEL (Litrax Technology Co., Ltd.) operating at 3.55 mA, just above the threshold current which is approximately 3.4 mA under feedback regime, temperature controlled at 35℃, and two lenses (C240TME-B, Thorlabs, Inc.) with both focal lengths and clear apertures of 8 mm to collimate and focus the laser beam. We used an optical chopper to modulate the beam and extract the diffuse reflectance intensity modulated voltage signal from the VCSEL terminal voltage. The optical chopper modulated the laser beam at 877 Hz which prevented the steady state diffuse reflectance signal from being submerged in the low frequency noise of the semiconductor laser. Optical chopper created two operating states in the laser which are the free-running and under optical feedback states [125].

Diffuse reflectance signal can be obtained both from the time domain signal, by looking

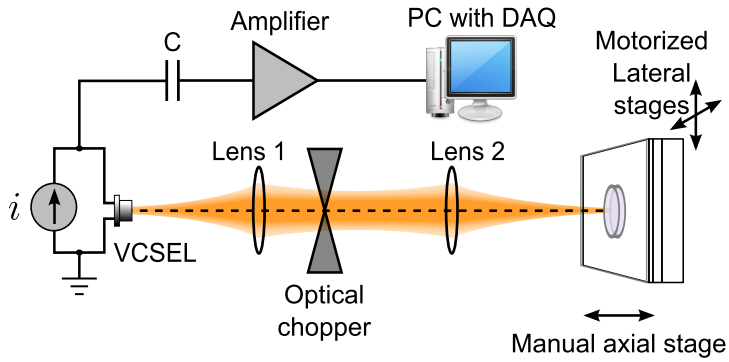

FIGURE 6.3: Experimental set up; laser feedback interferometry system raster scanning a three-layer skin tissue phantom including a KSC area.

at two levels of signal corresponding to the two aforementioned states, or from the signal spectrum by looking at the magnitude of the first harmonic of the frequency domain signal. We extracted diffuse reflectance signal from the frequency domain and normalized the measured signals at all the points to the maximum value to make the images.

We raster scanned the skin tissue phantom which was prepared as discussed in Sec. 6.1.4, to make the images. We scanned an area of 6×6 mm with 41×41 steps with 150 μm step sizes. At each point we obtained the amplified laser diode terminal voltage signal using a data acquisition card. The three-layer skin tissue phantom can be seen in Fig. 6.2. As discussed earlier, a cover slip was placed on the top of the three-layer phantom to stop agar from evaporating. It also suppressed the effect of strong surface reflection between the air and sample. Surface reflection from the cover slip was specular which was less likely to be backscattered into the laser cavity as it needed perfect alignment which we deliberately avoided in the experiment which is also challenging to achieve in an LFI system.

6.1.6 Experimental Results

Figure 6.4 shows the results of the experimental scans of the three-layer agar tumorous skin tissue which was prepared as discussed in Sec. 6.1.4 using the proposed LFI diffuse reflectance imaging technique. We scanned the tumorous model at eight different depths starting from above the tumorous area into the tumorous region to show the possibility of depth sectioning into the model. Scans started at the depth of about 280 μm from the surface of the first agar layer by adjusting the focal point at this depth and completing a lateral scan. We continued to perform the other scans by focusing into the agar sample at 100 μm length incremental steps which was equivalent to about 135 μm optical length

incremental steps, as the refractive index of the agar gel was taken to be 1.35. In other words, considering the surface of the first agar gel as the reference, the scans took place at eight different depths of 280, 415, 550, 685, 840, 955, 1090, and 1225 μm which are shown in Figs. 6.4 (a), (b), (c), (d), (e), (f), (g), and (h), respectively. The sample was mounted on a 3-axis translation stage with two motorized lateral stages and one manual axial stage along the laser beam. Then after accomplishing each lateral scan which produced an image, we manually moved the sample toward the laser using the axial stage by 100 μm which was equal to 135 μm optical length. All images then were normalized to the maximum recorded level of diffuse reflectance at each step. As discussed earlier, the thickness of the first layer was 500 μm and the tumorous model region was a 4 mm diameter cylindrical area enclosed in the second layer with the thickness of 1000 μm. Therefore the two first scans took place above the tumorous area which resulted in noise-like images which are illustrated in Figs. 6.4 (a) and (b), respectively. The third scan was perform at the depth of 550 μm and it can be seen in Fig. 6.4 (c) that the tumorous model region started to show itself at a lower level of diffuse reflectance compared to the surrounding area. As we continued to focus into the sample, the lower scattering tumorous model region manifested itself clearly in the provided images. Although all the other scans situated into the tumorous model area, as we focused deeper into the sample the signal started to fade out which was because of signal attenuation due to longer depth of scan.

The columns labeled as (i), (ii), and (iii) in Fig. 6.4 show raw, median filtered, and Gaussian filtered images, respectively. In other words, (i) is the image which was formed using the recorded self-mixing signal as it was obtained from the data acquisition card, (ii) was the raw image after applying a two dimensional median filter in Matlab, and (iii) was the raw image after applying a Gaussian filter in Matlab. Results show that our proposed technique can be used effectively in revealing the alterations in the optical properties of a tissue model non-invasively.

6.1.7 Monte Carlo Results

Monte Carlo is the name for a range of powerful simulation methods with a broad range of application which has also been used extensively in the field of modeling light–tissue interactions [18, 120, 144]. To interpret the experimental results obtained from laser feedback interferometry diffuse reflectance imaging technique, scanning a three-layer agar gel tumorous skin model, we numerically modeled the system by means of a MC simulation engine. Our MC model consisted of the optical system model, photon population, and a

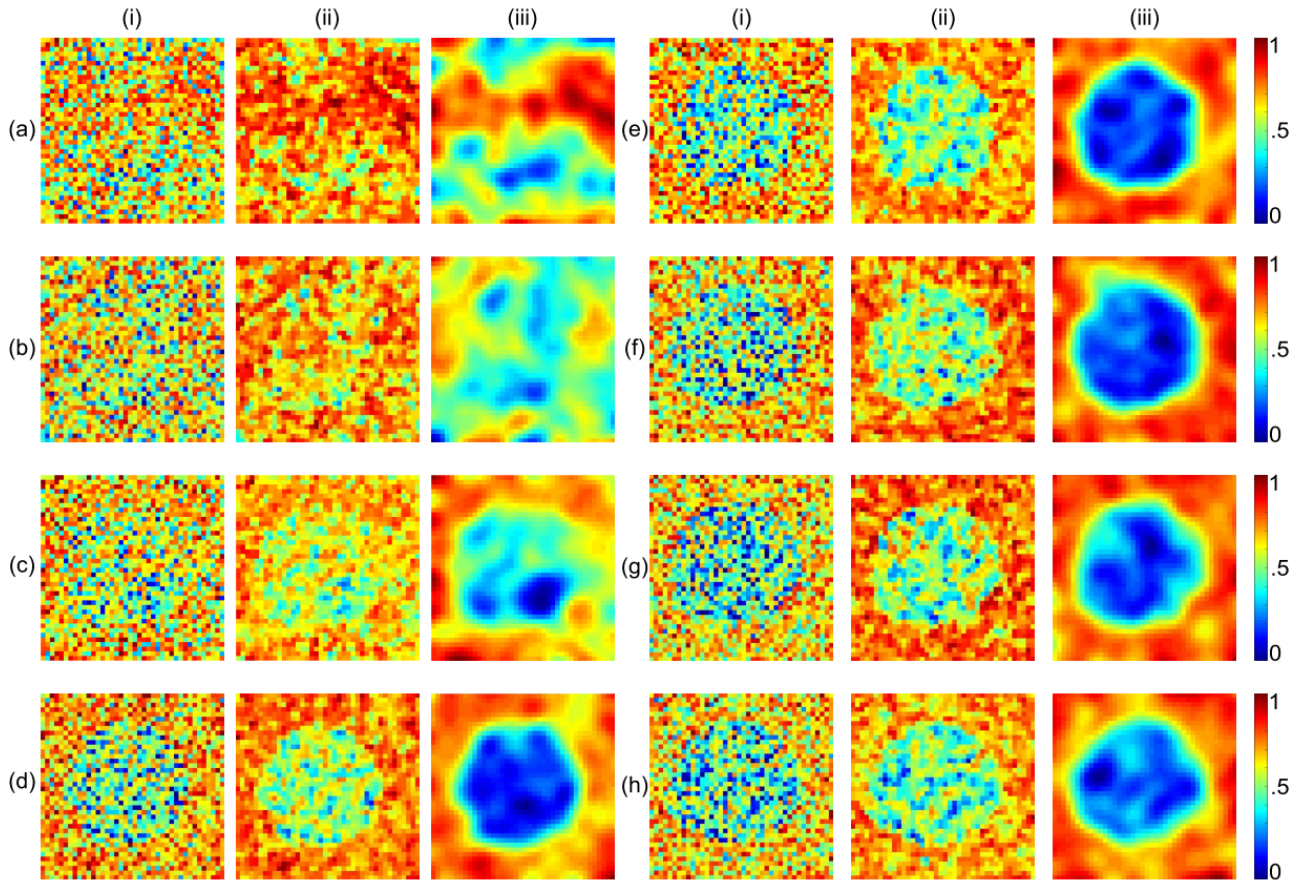

FIGURE 6.4: Laser feedback interferometry diffuse reflectance imaging experimental results; sub-figures of (a) to (h) illustrate the scan results at the focal depths of 280, 415, 550, 685, 840, 955, 1090, and 1225 μm from the surface of the first agar layer, respectively. (i)s show raw self-mixing image, (ii)s show the two dimensional median filtered image, and (iii)s show the two dimensional Gaussian filtered image.

three-layer tumorous skin model. We started the simulation by defining a Gaussian distribution of photons on the objective lens. About 2.5 million photons were included in the numerical model at each point which were characterized based on the specifications of the laser we used to conduct the experiments in Sec. 6.1.5.

We defined the geometrical and optical characteristics of the three-layer tumorous skin model in the simulation based on the properties of the agar gel sample that we described in Sec. 6.1.4. That is, the first layer in the numerical skin model was started with a 150 μm thick layer, modeling the cover slip, with scattering and absorption coefficients of zero. The second layer in the simulation was a 500 μm thick layer as the epidermis layer model, equivalent to an agar gel layer doped with about 1% volume proportion of instant coffee. The third layer in the simulation was a 1000 μm thick layer modeling the dermis layer, equivalent to an agar gel layer doped with about 0.1% volume proportion

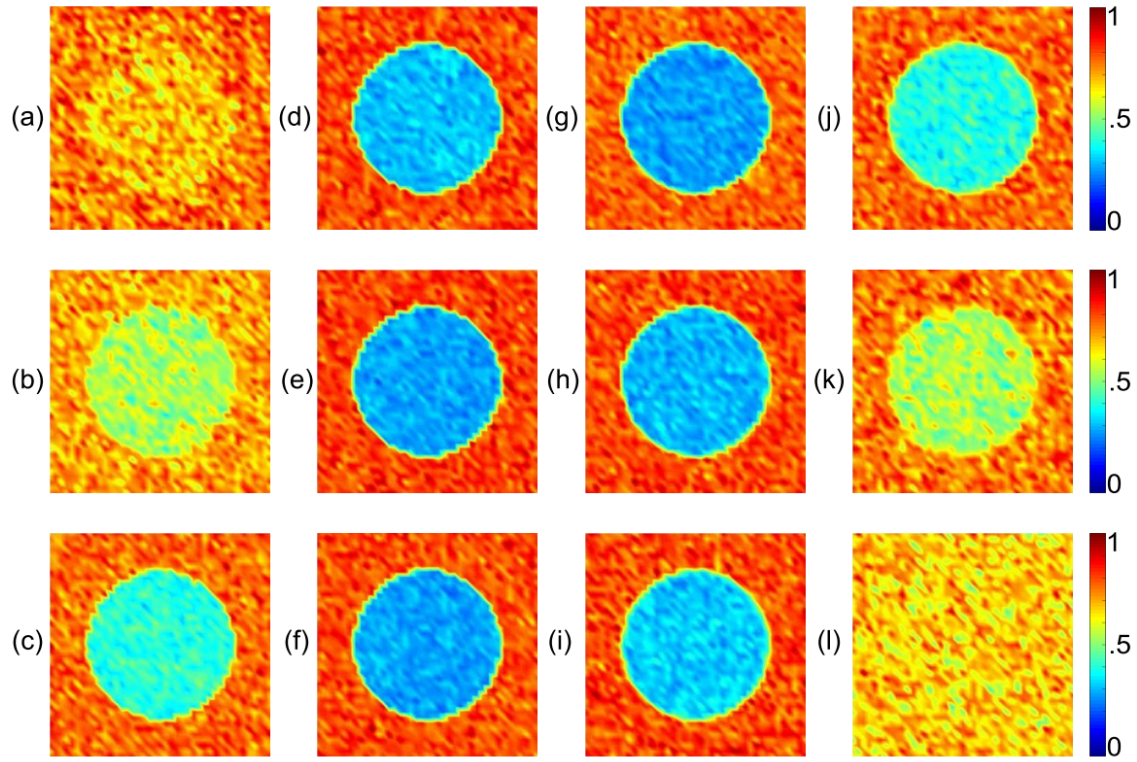

FIGURE 6.5: Monte Carlo simulation results for the three-layer tumorous skin model equivalent to the agar gel sample; sub-figures of (a) to (l) illustrate the simulated results at the focal plane depths of 185, 320, 455, 590, 725, 860, 995, 1130, 1265, 1400, 1535, and 1670 μm from the surface of the first skin layer model, respectively.

of TiO_2 enclosing a 4 mm diameter cylindrical lower scattering area in the middle. The fourth and final layer in the simulation was a 3.15 mm thick layer as the subcutaneous tissue model, equivalent to a pure agar layer. We defined basic scattering and absorption coefficients for all the three skin model layers equal to the values calculated in Sec. 6.1.4 for about 1% volume proportion of agar gel which were 65.85 and 0.5 m^{-1} for scattering and absorption coefficients, respectively. Then the extra optical properties due to the addition of TiO_2 and instant coffee were added to the basic optical properties. Scattering and absorption coefficients for TiO_2 were taken to be 142950 and 0 m^{-1}, respectively, and for instant coffee were taken to be 0 and 19948 m^{-1}, respectively, as measured in Sec. 6.1.4. We approximated the refractive index of all the layers including the cover slip to be 1.35 and the Henyey–Greenstein phase function with anisotropy factor of 0.85 was also considered to calculate the new direction of photons in the case of scattering events [66, 110].

Photons enter the skin model and interact with the turbid media in the simulation. A

small proportion of the photons travel back from the skin model and made their way back to the lens system. After performing ray tracing method to model the path of photons interacting with the lens system, the ones which found their way to the laser aperture were counted as a measure of diffuse reflectance level. To perform the ray tracing we defined the geometrical specifications of the lens system as it was used in the experiments conducted in Sec. 6.1.5. As with the experiments, simulations were also performed point by point by raster scanning the photon beam over the skin model to prepare the images. Furthermore, the area of simulated scans were 6×6 mm including 41×41 steps with 150 μm step sizes, similar to that for the experimental results.

Figure 6.5 depicts the simulated MC results at 12 different depths into the tumorous skin model. We started the first scan at the depth of about 185 μm into the tumorous skin model from the surface of the first skin layer and the result can be seen in Fig. 6.5 (a). We continued to scan by further depth sectioning. We moved the optical system numerically with 100 μm incremental steps which was equivalent to 135 μm optical length as the refractive index was considered to be 1.35. It means that the focal plane of the 12 scans laid at the depths of 185, 320, 455, 590, 725, 860, 995, 1130, 1265, 1400, 1535, and 1670 μm from the surface of the first skin layer model and the results of these numerical scans are shown in Figs. 6.5 (a) to (l), respectively. In the MC simulation, tumorous skin model was situated between the depths of 500 to 1500 μm. Therefore, the first three scans which were (a) to (c) and the last two scans which were (k) and (l) took place outside the tumorous area and it is clearly seen from Fig. 6.5 that images at these depths have lower contrast compared to the scans inside the tumorous area which are (d) to (j). Although the scans in Figs. 6.5 (b), (c), and (k) were performed at the depths outside the tumorous region, we are still able to see noisy images of the circular tumorous area as the sensing volume in the simulations at these depths were extended into the tumorous region. The simulated results in this section shows consistency with the experimental results in Sec. 6.1.5 and enables us to investigate the new possibilities and implementations of the technique in further research.

6.1.8 Conclusion

Keratinocyte skin cancer, in particular basal cell carcinoma and squamous cell carcinoma are the most frequently observed malignancies in the fair-skinned population [128, 129]. The most important factor in the development of KSC is exposure to increased ultra-violet

radiation while skin phenotype also plays an important role [128]. These kind of neoplastic skin diseases often develop from pre-existed skin lesions. As an example actinic keratoses are the most common precursors to squamous cell carcinomas [160]. Diagnosis of KSC in early stages is challenging as human skin has a large surface and it is susceptible to numerous diseases. Some of them may resemble one type of skin cancer closely. Laser and other optical imaging techniques based on functional and structural modalities of skin tissue which are able to provide in-depth images of skin tissue are promising tools to be used in early skin cancer detection compared to conventional techniques such as using a dermascope and histopathological tests.

In this paper we proposed a new technique of diffuse reflectance imaging in the near-infrared region with applications in *in vivo* biological tissue imaging and skin cancer detection. We proposed a compact, low-cost, self-aligned, and versatile LFI system in a confocal configuration. The confocal set up allowed to perform depth sectioning in preparing the images. To examine the technique we applied it to a three-layer skin tissue phantom and performed MC simulation of the experimental set up including the numerical model of the skin phantom. The skin tissue phantom was made up of agar gel dope with absorbers and scatterers to control the optical properties and included a 4 mm diameter cylindrical lower scattering region encapsulated in the second layer which resembled a KSC. We provided eight images from the skin tissue phantom at different depths into the sample by 135 μm optical incremental steps. A high degree of consistency exists between experimental and computational results which validated the theoretical base of the technique to be used in such purposes and the capability of the technique to produce sensitive images of the lower scattering region at different depths and with a penetration depth of well over 1.2 mm into the skin phantom.

6.2 Confocal Laser Feedback Tomography in Skin Cancer Detection

6.2.1 Abstract

We propose confocal laser feedback tomography for non-invasive cross-sectional imaging of soft biological tissues at depths penetrable to near-infrared beam. Confocal laser feedback tomography as an implementation of reflectance confocal microscopy is based

on laser feedback interferometry technique which is a heterodyne interferometric method of sensing. This compact system uses a semiconductor laser as both transmitter and receiver of the beam and possesses the imaging power of a confocal microscope. We examined the technique on keratinocyte skin cancer tissue phantoms by introducing macro-structural changes in dermis layer due to cancerous activities in the form of reduced optical properties. Experimental results tied with numerical simulations show the feasibility of a sensitive tomography system to be used in optical interrogation of deep skin tissue.

6.2.2 Introduction

Tomography which means the visualization of slices has gained momentum in biomedical imaging during the past decades [177, 178]. Optical tomography techniques such as diffuse optical tomography [179–181] and optical coherence tomography [37, 43, 45] use visible or near infrared lights to map the optical properties of highly scattering biological tissues. These techniques are safe and relatively low-cost compared to other tomography techniques [45] and are also able to image both morphological and functional features of biological tissues [182].

Despite all the advances, the research area is far from being mature and there is still place for a lower cost, versatile, and potentially portable tool which can be used for oncology purposes. We propose confocal laser feedback tomography (LFT) to be used for applications such as skin cancer detection. Confocal LFT works based on laser feedback interferometry (LFI) technique [8–10, 70, 71], and has already been limitedly applied to non-biomedical applications [140, 183, 184]. In the proposed system a vertical-cavity surface-emitting laser (VCSEL) serves as both transmitter and receiver of the beam and sensing signal happens as a result of interferometry of the beams inside the laser cavity [8–10, 70, 71]. This system has a confocal structure and can be considered as an implementation of confocal microscopy [38, 39, 138], where VCSEL aperture acts as a pinhole for the system to eliminate out of focus reflected beams [141]. One of the main advantages of this system is to be compact, at the same time it possesses the imaging power of a confocal microscope. That is because confocal LFT is self aligned; we only need to focus the beam into a tissue and back reflection to the laser occurs through the same optical system. On the other hand, there is no need for a detection arm as detection happens inside the VCSEL cavity and signal can be obtained from VCSEL's terminal voltage or photocurrent of an in-built photodiode situated inside the VCSEL's package. In addition, confocal LFT is a very low optical power system, in the range of a few hundreds of micro-watts, due to heterodyne nature of self-mixing detection, where a minute portion

of the reflected beam mixes with strong intra-cavity fields within the VCSEL's cavity to make a sensitive and safe sensing device [8–10,70,71]. Also, VCSEL is chosen to operate at 850 nm, within the biological window, to avoid high absorption of water, oxygenated and deoxygenated haemoglobin and benefit from maximum penetration into soft biological tissues [179].

To examine the system we tested it in a skin cancer detection application. Melanoma and keratinocyte skin cancers (KSCs) are the most common types of cancer among fair-skinned people [128] and the incidence rate is increasing ever year [129]. Although KSCs (equally called non-melanoma skin cancer) have a high cure rate, they can still be aggressive [128, 130] and early detection will reduce the mortality rate [3]. Use of non-invasive techniques to improve skin cancer detection started by introducing dermascope to the field in the late '80s [25, 26]. Afterward other techniques have been proposed and applied [28,46], but confocal microscopy can probably be considered as the most successful method in this application [31–35]. In this work, we used confocal LFT as an implementation of confocal microscopy to make three-dimensional (3D) and cross-sectional images of macro-structural changes in the skin tissue due to cancerous activities. We used three-layer silicone-based tissue phantoms of three different types of KSCs as cancerous tissue models. Three layers of tissue phantoms represent epidermis, dermis, and subcutaneous tissue layers. Cancer affected regions have been incorporated into these tissue phantoms as volumes of reduced optical properties (such as scattering coefficient (μ_s) and absorption coefficient (μ_a)) situated in the dermis layer [11]. Reduction of about 10, 30, and 40 percent in the μ_s of infiltrative basal cell carcinoma (infBCC), nodular basal cell carcinoma (nodBCC), and squamous cell carcinoma (SCC), as the three types of KSCs, have been reported in [11] and typical optical properties of skin tissue layers have also been reported in [110], which we adopted to prepare tissue phantoms. Results show that confocal LFT is able to provide cross-sectional images of the tissue at depths of up to 0.9 mm into the tissue phantom and volumes of the phantom at altered optical properties can be mapped in 3D space at different levels of sensitivity. It is also shown that this technique is sensitive enough to detect reduction in the μ_s of the dermis layer as small as only 10 percent. In addition to the experimental results, we also conducted a Monte Carlo (MC) simulation which studies the execution of the proposed optical system on equivalent numerical models for the KSC tissue phantoms. Numerical results show a high degree of consistency with the experimental results and endorse the idea of using confocal LFT in such an application.

This work investigates the feasibility of a new optical technique which may have an

effective role in skin cancer detection. The remainder of the paper is structured as follows: section 6.2.3 discusses the theory and configuration of confocal LFT, section 6.2.4 presents the experimental aspects of the work including tissue phantom making procedures and also details and results of the experiments, in section 6.2.5 a MC numerical model of the same optical system and tissue models is presented and simulated results are compared with the experimental results, and finally section 6.2.6 concludes the paper.

6.2.3 Confocal laser feedback tomography

Confocal LFT works based on LFI technique [8–10, 70, 71]. Sensing in this technique occurs when a fraction of the laser beam reflects back from a distant target into the laser cavity and interferes with the strong intra-cavity fields, therefore modulating both the amplitude and frequency of the lasing field. Back-reflected beam contains information about the target which then can be extracted by monitoring the laser's output optical power or terminal voltage. Although this phenomenon can be observed in different types of lasers, laser diodes are mainly used as the source/detector in such systems [71, 82]. LFI can be used in general remote sensing applications such as distance, displacement, vibration, and velocity measurements [71], but two applications that show its potential functionality to be applied to *in vivo* biological tissue tomography are 3D imaging and microscopy. LFI has been used to obtain images of objects in 3D space [185–187], and also in non-biological [77, 117, 118, 139] and biological [188, 189] microscopy applications, where is can easily go down to sub-micrometer lateral resolutions. In one of the first demonstrations, Juškaitis *et al.* represented a simple and compact confocal microscope using just a laser diode and a optical system based on LFI technique [77].

In a reflectance confocal microscope, a fraction of the back-reflected beam coming from a minute spatial sensing volume around the focal point, which passes through a pinhole situated on its way back, is detected usually by photomultiplier tubes or avalanche photodiodes. Pinhole acts as a spatial filter to eliminate out of focus beams [38, 39, 138]. To achieve optical sectioning, we need to scan the focal point over the target at a constant depth. Confocal LFT using a semiconductor laser such as a VCSEL, is a special embodiment of a confocal microscope, where VCSEL aperture (with a diameter normally in the range of a few micrometers) serves as a confocal pinhole. The main difference is that in a conventional confocal microscope sensing signal is the amount of back-reflected light detected by a photodiode, while it is as a result of interferometry in the laser cavity in a confocal LFT which makes it a simple and compact technique. Figure 6.6 illustrates the configuration of the confocal LFT used in this work, and it shows

how VCSEL's aperture acts as a confocal pinhole to eliminate the out of focus beams. Furthermore, VCSEL operates just above the threshold current and incident optical power on the target is in the range of a few hundreds of micro-watt which makes it a safe and low-power device compared to other similar counterparts for the purpose (for instance, a typical confocal microscope uses an in-plane laser diode with a maximum optical power of 35 milliwatts [5]). Being safe, low-power, and compact, confocal LFT has a potential to be used as a portable tool for oncology purposes. We have previously suggested confocal LFI for skin cancer detection purposes [141, 149] and its versatility is shown by a dual-modality imaging application D.

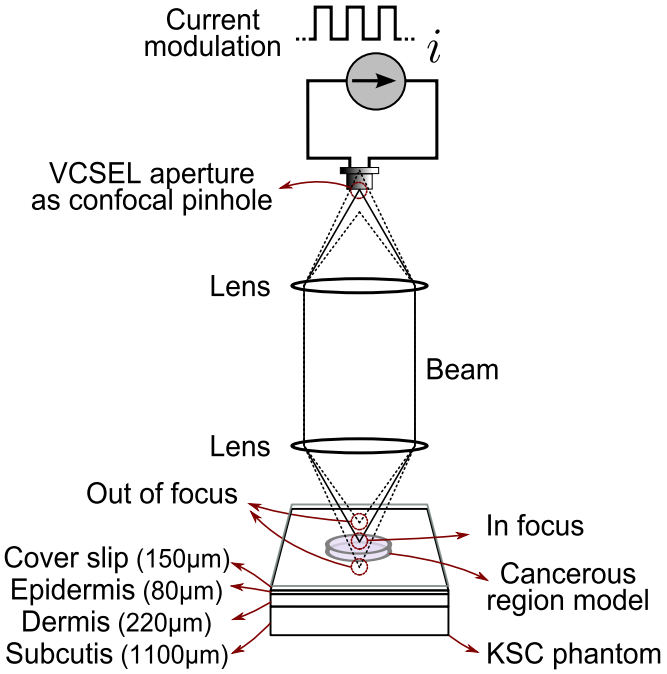

FIGURE 6.6: Confocal laser feedback tomography apparatus with VCSEL's aperture acts as a confocal pinhole to eliminate out of focus beam. VCSEL current is modulated at a low level around the operating current to create two levels of LFI signals. Beam is focused on a silicone-based three-layer KSC tissue phantom.

6.2.4 Experiments

Keratinocyte skin cancer tissue phantom

Human skin is a multi-layer tissue and mainly consists of three layers of epidermis, dermis, and subcutaneous tissue. Epidermis, the outermost layer, contains melanin, the main absorber of visible light, while dermis doesn't and has a lower μ_a. Subcutaneous tissue

is the lowermost layer and consists of fat cells. Optical properties of human tissue have been studied extensively [88]. However, universal and well-known cancerous activities such as angiogenesis [14], abnormal cell nucleus structure [190] (as the main scatterer of light), increased nuclear to cell volume [158], out-flow of fluid from leaky blood vessels [56], and other morphological and molecular changes will alter the optical properties of cancerous skin tissue [11]. These micro- and macro-structural changes are considered as biomarkers in an optical system for diagnostic and treatment purposes.

This work focuses on detecting regions at altered optical properties in three types of KSC. In order to make skin tissue phantoms, μ_ss of epidermis, dermis, and subcutaneous tissue models are taken to be 23, 13, and 13 mm^{-1}, respectively, and μ_as of them are taken to be 0.4, 0.1, and 0.1 mm^{-1}, respectively [110]. We included the cancer affected regions as cylindrical regions situated at the second layer (dermis) and enclosed by it, with a diameter of 3 mm, and a thickness similar to dermis layer. Diameters of the cancerous models were in the range of typical KSC precursors [161]. We considered reduction in the optical properties of the cancerous models with respect to dermis layer. In [11], optical properties of infBCC, nodBCC, and SCC samples were measured over an extended spectral range, and it was shown that at 850 nm the μ_ss of infBCC, nodBCC, and SCC drop by factors of 0.9, 0.7, and 0.6, respectively, and μ_as of them drop by factors of 0.8, 0.2, and 0.4, again respectively, all with respect to dermis tissue optical properties [11]. We applied these levels of decrease in the optical properties of the cancerous regions in three types of KSC tissue phantoms.

We chose to fabricate silicone-based tissue phantoms due to their stability and good performance in providing homogeneous samples. Commercial kit for base and curing agent for two-part polydimethylsiloxane (PDMS), which is a room-temperature vulcanizing silicone, were purchased (Sylgard® 184 Silicone Elastomer Kit). PDMS refractive index is about 1.43, in the range of infrared. This is close enough to its value for human skin tissue [191]. PDMS is a clear material with negligible μ_s and μ_a. Therefore, we used titanium dioxide (TiO_2) and Indian ink to control its optical properties. TiO_2 and Indian ink are among the most accepted scatterer and absorber of light in this spectral range, respectively [85]. We purchased commercially available TiO_2 (Sigma-Aldrich, Corp.) and Indian ink (Winsor & Newton, Co.). TiO_2's μ_a and Indian ink's μ_s can be neglected as they are much smaller than their other optical properties. We approximated the μ_s and μ_a of pure TiO_2 and Indian ink, using Beer-Lambert technique [149], to be about 380 and 290 mm^{-1}, respectively.

To make the base silicone gel for each one of the layers, we added 2.5 gr of PDMS curing agent to 25 gr of base part (one to ten proportion). We added TiO_2 and Indian ink

to the base gel based on the calculated proportions to make favorite optical properties for each one of the layers. TiO_2 was added in a weight-to-weight way using a 0.1 mg precision balance, while Indian ink was added using a 1 micro-liter precision pipette. After adding TiO_2 and Indian ink we stirred the mixture mechanically for about 30 minutes to achieve a uniform distribution of scatterers and absorbers. In order to make the layers, we poured the mixture between acrylic glass sheets and put thin sticky tapes or other spacer between the sheets to achieve favorite thicknesses. Layers were then left for at least two days to cure. We chose acrylic glass sheets because it was easier to remove the layers from them after curing process, compared to other types of glass slide. We built epidermis, dermis, and subcutaneous tissue layers with thicknesses of 80, 220, and 1100 µm, respectively, and the thickness of cancerous models are the same as epidermis thickness. We place a 150 µm glass cover slip on top of the KSC tissue phantoms as an anti-diffusive layer. A schematic diagram of one of these KSC tissue phantoms can be seen in Fig. 6.6.

Experimental details

Experimental setup is shown in Fig. 6.6. In this setup we used an 850 nm VCSEL (Litrax Technology Co., Ltd.) operating at 3.55 mA, just above the threshold current (at about 3.4 mA). VCSEL was temperature controlled at 35℃ to have a better LFI signal [122]. Beam was collimated (using a C240TME-B, Thorlabs, Inc. lens) and focused (using a C330TME-B, Thorlabs, Inc. lens) on the target. Focused beam had a focal length and numerical aperture of 3.1 mm and 0.68, respectively, and a focal beam spot diameter and Rayleigh length of about 1.8 and 2.9 µm, respectively. Laser and optical system were placed on a three axes translation stage (Zaber Technologies Inc.). Perpendicular beam was then raster scanned over the phantoms. Scanned area at each one of the optical sections was 4.5×4.5 mm in 91×91 steps at 50 µm pitches (lateral resolution), and when accomplished, focal point was moved deeper into the phantom by 20 µm (axial resolution) to the next optical section, by 48 steps (scanning an axial length of 0.94 mm). Scans were started at about 40 µm above the phantoms and a volume of $4.5\times4.5\times0.9$ mm of the phantom was scanned. VCSEL current was modulated at a low level around the operating current (as shown in Fig. 6.6) to create two levels of feedback which was then extracted as the LFI signal to quantify the reflection level. Frequency of current modulation was 5 kHz. Signal was acquired from an in-built photodiode in the VCSEL package, using a data acquisition card at a rate of 100 kS/s. At each point 1000 samples of the signal were read and fast Fourier transform was applied to the time sequence to

convert the signal into frequency domain. LFI signal was then extracted at the frequency of modulation (5 kHz).

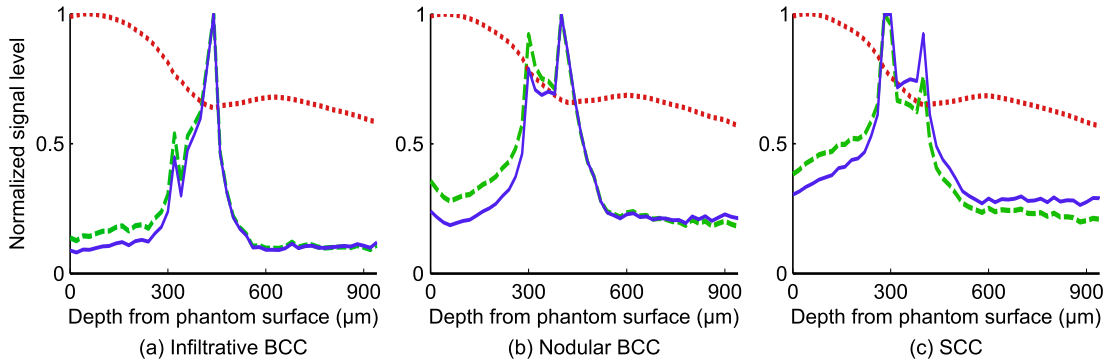

FIGURE 6.7: Average signal levels (red dotted line), dynamic range of the signal at optical sections (green dashed line), and compensated dynamic range (blue solid line) versus the scan depth from the top of the cover slip (all normalized to the maximum levels), for three types of KSC tissue phantoms: (a) infBCC, (b) nodBCC, and (c) SCC.

Skin phantoms are strongly scattering and beam will be attenuated as soon as it enters them. Therefore, we needed to compensate for the signal attenuation to reconstruct the 3D images. We measured the average signal level at each one of the optical sections and compensated for the drop in the signal levels as the beam got deeper into the phantom. In addition, we needed to compensate for the drop in the dynamic range of the signal at each one of the optical sections. So, after normalizing the signal levels at optical sections, we multiplied them by a reverse factor of attenuation. Figure 6.7 shows the average signal levels, dynamic range of the signal at optical sections, and compensated dynamic range versus the scan depth from the phantom surface (phantom surface is considered as the surface of the cover slip). Higher dynamic ranges of signal in this Fig. happen at depths where cancerous models are incorporated and are indicators of strong changes in the optical properties over the scanned areas.

Results

Figure 6.8 shows the scan results at each one of the optical sections, starting at just above the top surface of the epidermis layer in the SCC phantom and ending at the depth of 400 μm, including 21 images. A two dimensional median filter has been applied to provide these images, and slice images are compensated for the drop in the level of signal and dynamic range (as discussed in section 6.2.4) and are normalized to the maximum level of signal in all the slices. The first five slices occur in the epidermis layer (80 μm

tick) where there is no cancerous region. And, small circular drop in the level of signal is due to the cancerous model at deeper areas. Images at the depths of 100 and 280 µm and between, cross the cancerous model (with lower optical properties) situated in the dermis layer (220 µm tick). Stronger contrast can be seen in these images. Other images situate in subcutaneous tissue. Small areas with higher contrast on the right side of the first slices outside the cancerous image in Fig. 6.8, are due to an air gap between the epidermis and dermis layers, where these layers are not stuck together completely.

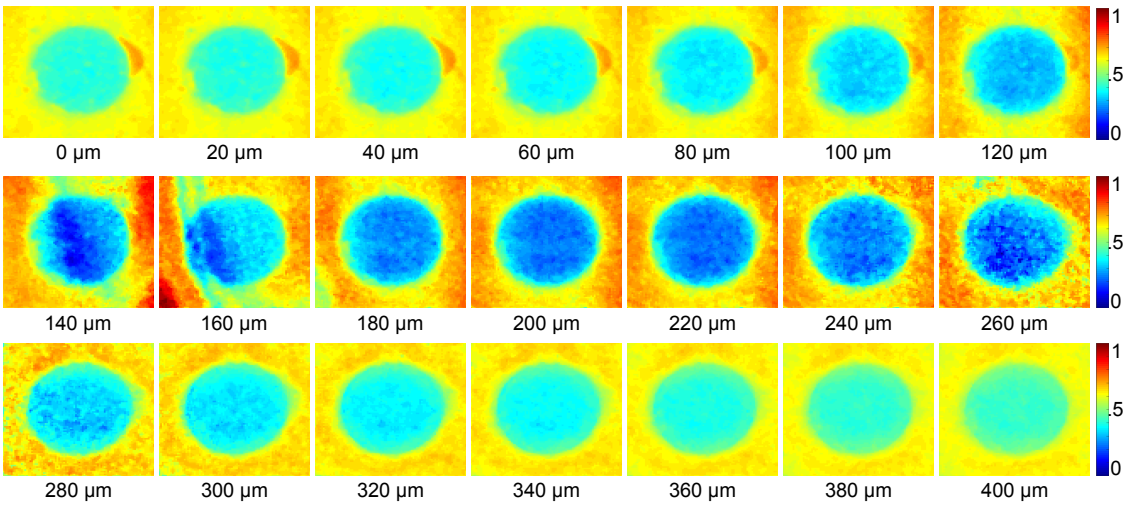

FIGURE 6.8: Images provided at different depths of SCC phantom, starting at just above the top surface of the epidermis layer and ending at the depth of 400 µm in subcutaneous tissue. Stronger contrast can be seen at depths where cancerous model is incorporated, enclosed in the dermis layer.

If we put all the optical sections on top of each other and resolve the signal points in a 3D space, we have a 3D matrix of signals that can be used for making different types of 3D visualization. For instance, isosurface of points at a constant reflection level (CRL) can be illustrated. It is an enclosed surface, encompassing regions at lower level of signal. It means at a proper level of signal, isosurface should display regions at a reduced optical properties (KSC models). Figure 6.9 (a) to (c) shows (i) angle view, (ii) top view, and (iii) side view of isosurfaces for infBCC, nodBCC, and SCC, respectively. Larger drop in the optical properties of cancer model results in higher contrast in signals, while smaller drop results in lower contrast, where noise and imperfections of the system may submerge the signal area. Isosurface images for infBBC, nodBCC, and SCC in Fig. 6.9 are provided at CRLs of about 0.7, 0.5, and 0.3, respectively (considering the normalization of signal to the maximum signal value in each one of the cases). Formation of an enclosed volume at a lower CRL indicates a stronger contract in the level of optical properties. From the

CRLs in Fig. 6.9, it is inferred that SCC has the highest contrast, while infBCC has the lowest one. This result matches the level of drop in μ_s for infBCC, nodBCC, and SCC which are by factors of 0.9, 0.7, and 0.6, respectively (considering μ_s as the dominant optical property as it is much larger than μ_a). Figure 6.9 (a) shows that this confocal LFT is sensitive enough to show just 10 % drop in μ_s which can be considered as the sensitivity level of the system as well.

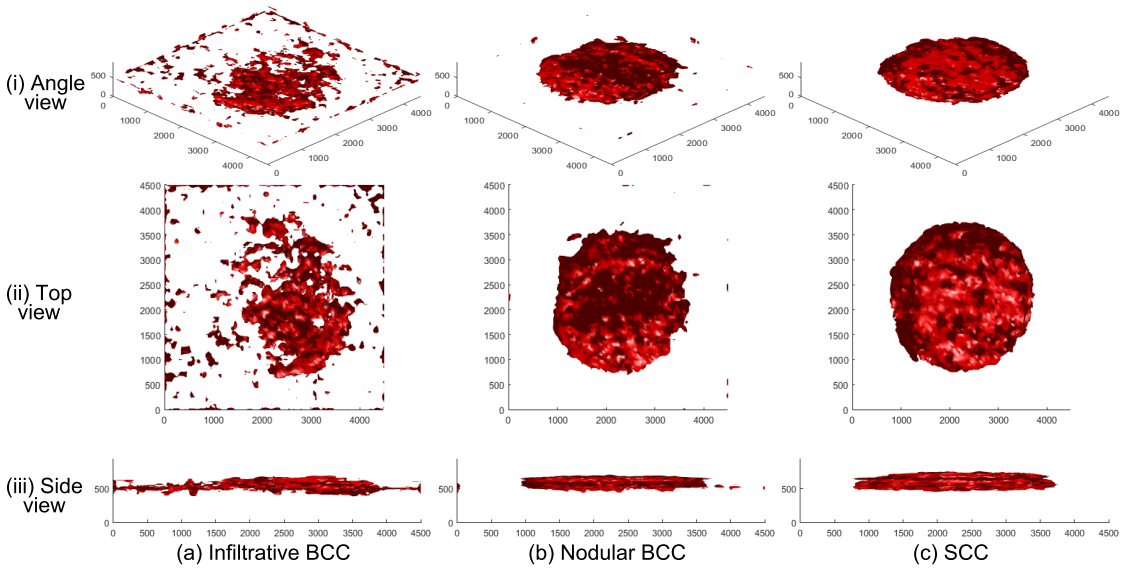

FIGURE 6.9: Isosurfaces for (a) infBCC at CRL of about 0.7, (b) nodBCC at CRL of about 0.5, and (c) SCC at CRL of about 0.3. (i), (ii), and (iii) represent the angle, top, and side views, respectively. Axes of the plots are the coordinates of the scanned volume in µm.

In order to find the threshold CRLs in Fig. 6.9, we plotted isosurfaces for CRLs from zero to one in 0.01 increments. Regions at lower reflections appeared first and at a threshold CRL, volume at reduced optical properties and its boundaries were visible. Figure 6.10 visualizes how CRLs are used to make isosurfaces. It shows a CRL at 0.3 cutting a surface view of one of the SCC phantom optical sections. Regions at a lower reflection level are enclosed in the corresponding isosurface.

6.2.5 Simulations

Monte Carlo model

Monte Carlo is a powerful method for modeling light-tissue interactions and characterizing optical techniques [144]. We performed a MC simulation to examine the experimental results. We used an in-house object-oriented MC engine prepared in MATLAB (R2015a,

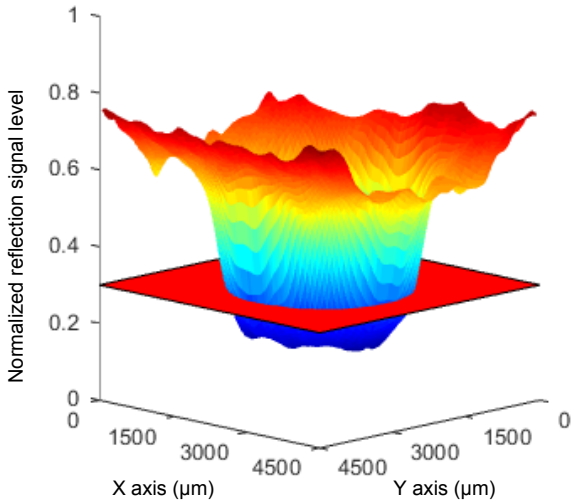

FIGURE 6.10: A constant reflection level (red plane) at 0.3 cutting one of the optical sections of SCC phantom (regions below the constant reflection level will be enclosed in the isosurface view).

UQ academic license, Brisbane, Australia). To perform MC modeling, we numerically defined optical system (laser and lenses), beam (a population of photons moving in 3D space), and KSC models. Numerical models for infBCC, nodBCC, and SCC were defined with the exact geometrical shapes and optical properties of that for the KSC phantoms, a explained in section 6.2.4. We took the refractive indexes of the models for cover slip and layers to be 1.35 for the purpose of index matching. A population of 0.2 million photons was defined with a spacial Gaussian distribution on the objective lens. Photons were launched toward the targets in a hyperboloid geometry [61]. A portion of the photons enters the KSC models and interacts with scatterers and absorbers. We used a Henyey-Greenstein phase function with anisotropy factor of 0.85 to define scattering angles. A portion of the photons exits the KSC models, passes through the lenses, and reenters the laser aperture which we considered as detected photons. Lenses were defined based on the physical characteristics of the ones we used to conduct the experiments (C330TME-B and C240TME-B) released by Thorlabs incorporation. Numerical structure resembled the experimental setup as shown in Fig. 6.6. Numerical model was scanned over the KSC models in a similar way as we scanned the experimental setup, scanning the same volume but with different numbers of step. A volume of $4.5\times4.5\times0.9$ mm in $37\times37\times31$ steps, at pitches of $125\times125\times30$ μm was numerically scanned and at each point the number of detected photons was considered as the reflection signal level.

Results

In a similar way, we put the numerical reflection signals in a 3D matrix corresponding to the scanned volume of the targets and plotted the isosurfaces of regions at lower reflection levels. Figures 6.11 (a) to (c) show (i) angle, (ii) top, and (iii) side views of isosurfaces for infBCC, nodBCC, and SCC models, respectively. It can be seen that numerical results are closely similar to experimental results in Fig. 6.9. Figure 6.11 (a) is at a lower noise level compared to Fig. 6.9 (a), which is expected as numerical model is not noisy as its experimental counterpart.

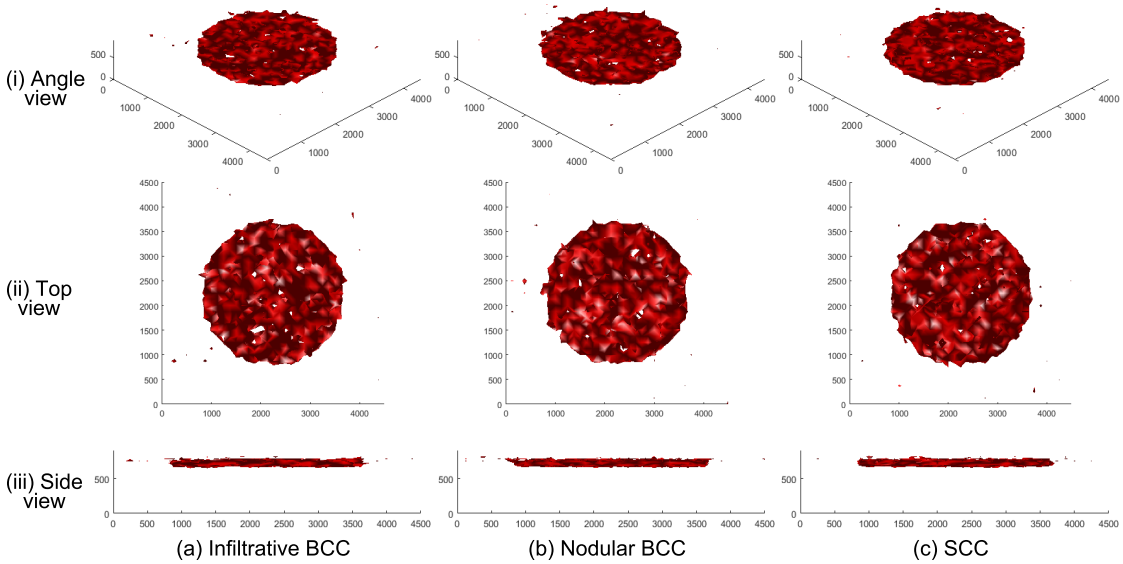

FIGURE 6.11: Numerical isosurfaces for (a) infBCC, (b) nodBCC, and (c) SCC, when (i), (ii), and (iii) represent the angle, top, and side views, respectively. Axes of the plots are the coordinates of the scanned volume in µm.

6.2.6 Conclusion

Confocal laser feedback tomography was proposed to be used in non-invasive skin cancer detection. This technique was applied to cancerous tissue phantoms. Three-layer silicone based phantoms for infiltrative basal cell carcinoma, nodular basal cell carcinoma, and squamous cell carcinoma were built and cancer affected models were incorporated in these phantoms as regions at reduced optical properties. Cross-sectional imaging were done and tomographic presentation of macro-structural changes in the optical properties of the phantoms were illustrated in three dimensional space. To underpin the experimental results, system was studied numerically using Monte Carlo simulation and it was shown

that numerical results were consistent with experimental results. Results of this work suggest the feasibility of a sensitive, low-cost, versatile, and compact device with potential applications in early skin cancer detection.

Chapter 7

7. Parallel Laser Imaging

The parallel read-out sensing scheme enables high-resolution imaging systems employing electronic scanning with faster acquisition rates in one dimension than mechanical scanning systems. To achieve this, a 24 channel monolithic VCSEL array imaging system was proposed by the previous group members [192, 193] and electronic parts such as a 24 channel driver including the receiver, and amplifier were designed and built. As a part of my PhD I tested and characterized the VCSEL array, measured the light–current and voltage–current curves for the channels, measured SNRs of the channels under different current operations, determined optimized operational currents to gain the best SNR from the channels, investigated the thermal behavior of the array by installing thermistors next to the array, installed electric triggering of the channels, conducted the noise characterization of the channels, was involved in mounting the laser array head on x–y–z translation stages, created LabVIEW software to control and run the system and save the signals in a PC, tested and automated the software to control the currents of the array, and performed signal processing, amongst other work.

This chapter includes the details of the activities that I have carried out or I was actively involved within this project. Then it is followed by paper G which discusses the enhancement of the SNR of each one of the laser channels in a concurrent operation of VCSELs in the array, a phenomenon that was linked with temperature increasing due to concurrent operation of laser channels in the array, which was observed and documented for the first time in such systems.

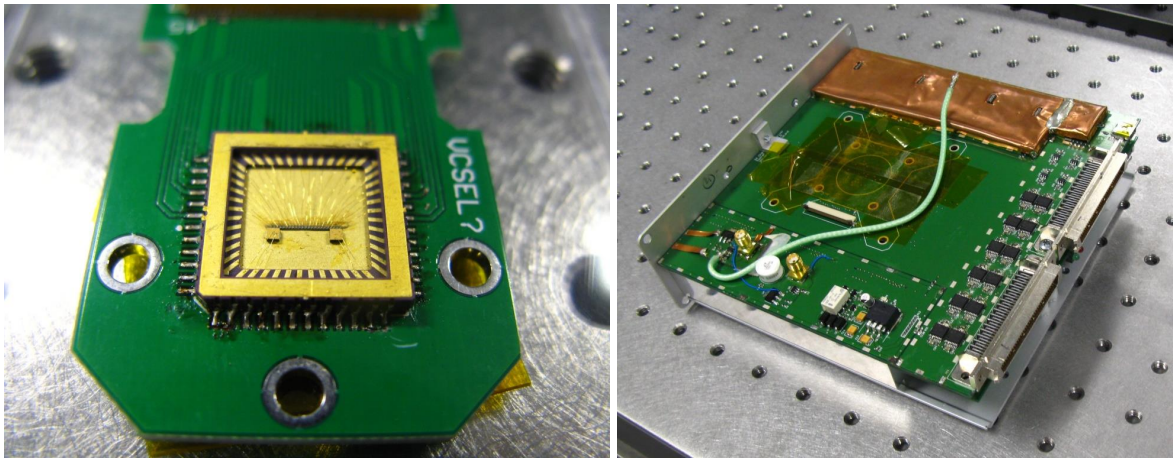

(a) (b)

FIGURE 7.1: Parallel readout components (a) mounted 24 channel VCSEL array including two thermistors at the ends (b) 24 channel driver including receivers and amplifiers of the channels.

7.1 Optical Laser Head

The first step in conducting the project was to prepare a circuit for the optical laser head. A 24 channel proton implanted VCSEL array (purchased from LITRAX Company) was installed on a one squared centimeter Surface Mount Ceramic Package by epoxy. The length of the array was about 5 mm with pitches of 220 µm (distance between channels). Due to safety regulations, the wavelength of 850 nm (near-infrared) was chosen for the lasers as light at this wavelength is safe (safer compared to ultraviolet) for human tissue, where it has a low absorption and longer penetration depth. However, one important precaution when working with lasers at 850 nm is to wear proper safety goggles as the beam at this wavelength is invisible. Wire bonding was done by a local company which had thermo-sonic wire bonding facility to solder golden micro wires to the laser electrodes and ceramic package contacts. The printed circuit board (PCB) which was needed to mount the ceramic package on, was prepared by other group members. A 40 pin connector was placed on the PCB and a proper ribbon cable was provided to connect the optical head to the laser drivers. Figure 7.1 (a) shows the laser mount package and fig. 7.1 (b) shows the 24 channel driver which includes the receivers and amplifiers to run the array.

7.2 Thermal Effects on the Operation of VCSEL Array

The thermal behavior of the laser array was characterized. Two miniature surface mount thermistors were ordered and installed near the ends of the laser diode array to monitor the temperature changes. Thermistors can be seen at the two ends of the laser array in fig. 7.1 (a). Investigating the effects of temperature changes on the operation of the lasers is important in finding optimized laser currents. We measured the thermistor parameters and characterized them by placing the circuit, including the thermistors, in a constant temperature chamber with a controlled temperature. We plotted the resistance–temperature curves for the thermistors by sweeping the temperature of the chamber and writing down the resistances of the thermistors. We used the Steinhart-Hart formula model as follows to estimate the thermistor's parameters:

$$\frac{1}{T} = A + B \cdot \log(R_T) + C \cdot (\log(R_T))^3, \tag{7.1}$$

where A, B, and C are the thermistor's parameters and R_T is the resistance at the temperature T. We required these parameters to determine the temperature by measuring the resistance of the thermistors.

Operation of each one of the lasers has thermal effect on the operation of other adjacent lasers. This is known as thermal crosstalk between the laser channels. The heat at each one of the lasers is generated by the electric current passing through them. We monitored the thermal changes in the laser array, which is a function of the currents passing through channels using thermistors and also a thermal camera. Further discussions about thermal effects are included in paper G.

7.3 Characterization of VCSELs in the Array

We characterized each one of the laser diodes in the VCSEL array to predict their behaviors in the system. Characterizing a laser means to obtain its L-I-V curves which are the optical power and junction voltage versus laser current. These curves help to determine threshold and thermal roll-over currents. A circuit was built to get access to the terminal voltage of each one of the single channels in the array and an Arroyo Instruments laser driver was used to sweep the current of each one of the lasers automatically and saved the junction voltages and optical powers concurrently. Optical power was measured by means of a power meter. The light–current curves for seven of the lasers are shown in fig. 7.2 (a).

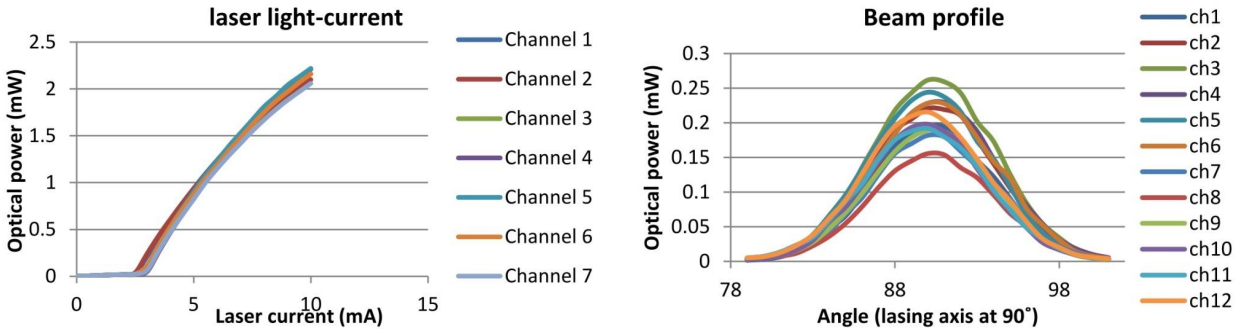

FIGURE 7.2: (a) Light-current curves for 7 exemplar channels of the VCSEL array and (b) beam profile of 12 exemplar channels of the VCSEL array.

We also measured the beam profile of each one of the single channels, which contains information as the beam shape and divergence angle. Determining the beam profiles helps us to control, collimate, and focus the beams. To do that, we turn on the lasers one by one and measured the emitted optical powers at different angles around the lasing axis. In the setup, we placed the laser at a fixed position and swept the power meter head around the laser. The maximum power occurs along the lasing axis (which is the axis perpendicular to the laser aperture surface) and as one moves away from the lasing axis, the optical power drops. The measured beam profiles show that they are approximately Gaussian with divergence angles of about 7.5°. The beam profiles of the first 12 channels can be seen in fig. 7.2 (b). As shown in this Fig., the maximum optical power occurs at 90°, as expected (lasing axis).

7.4 Driver, Control Software, and Translation Stages

We tested and troubleshot the driver of the 24 channel system. The driver was composed of 24 separate channels of drivers, receivers, amplifiers, and filters. The driver was designed and built by other group members. We connected the lasers and optical head to the driver by a cable ribbon. Then we connected the driver to the PC using a National Instrument Data Acquisition Card. We examined the signals from the channels coming from a simple rotating disk target. We located the faulty channels and the nature of the problems and we looked up the bad connections on the laser driver boards and noisy channels. One of the problems with the laser driver was that there was not any trigger input in the driver to synchronize the measurement with an external trigger signal. We found the input pin numbers of the NI DAQ card to get the trigger signal and installed an

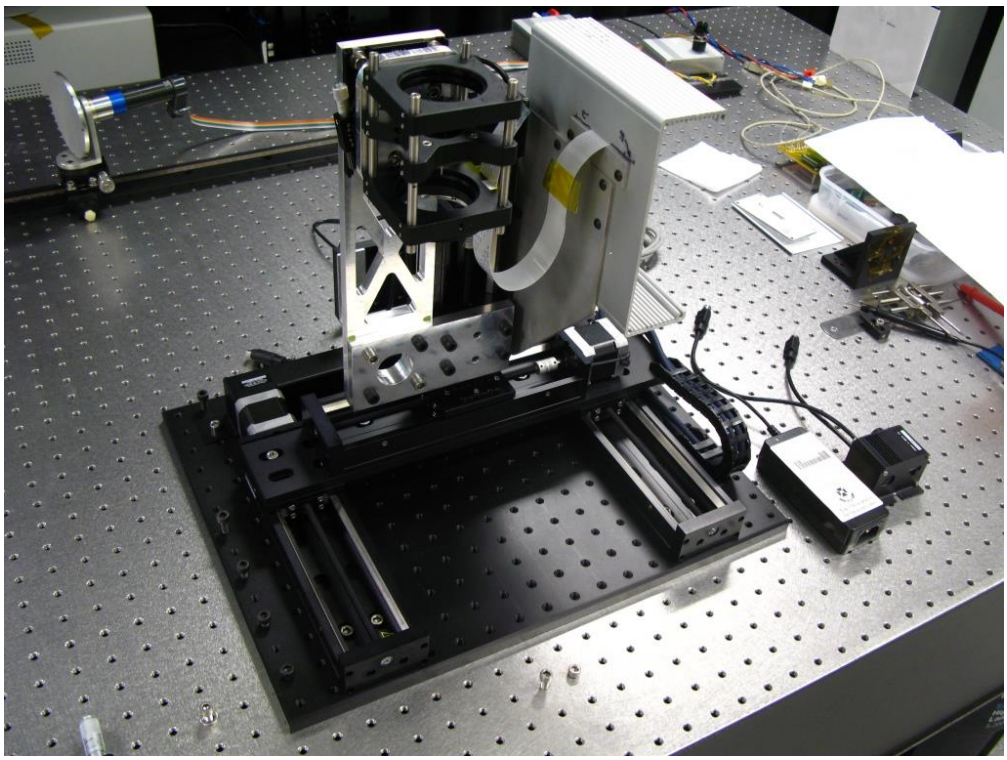

FIGURE 7.3: Translation stages and optical head on an optical table.

SMA port on the driver circuit and connected it to the trigger output of the signal generator. This enabled us to modulate the laser currents.

To control the VCSEL array drivers, software was developed. Using this software, the current, voltage, and gain of the each channel could be controlled individually. We also tested the software and diagnosed the problems and reported them. In this system, the diode junction voltages of the VCSELs are received and amplified as the LFI signals.

We installed the laser in a cage structure which included a large monolithic lens (to focus the beam) and the optical laser head. We then installed the cage and driver on a x–y–z translation precise motorized system. We used the translation system to move the optical head laterally (to carry out the scans) and vertically (to focus the beam). For this purpose we used three Zaber stages. We installed the stages on an optical table and attached the cage structure to a bracket on the vertical axis. We connected the translation stages in series and created LabVIEW software to control the movement of the stages, as well as to acquire the signal from the VCSELs terminal voltages concurrently. Figure 7.3 shows the translation stages and the optical head.

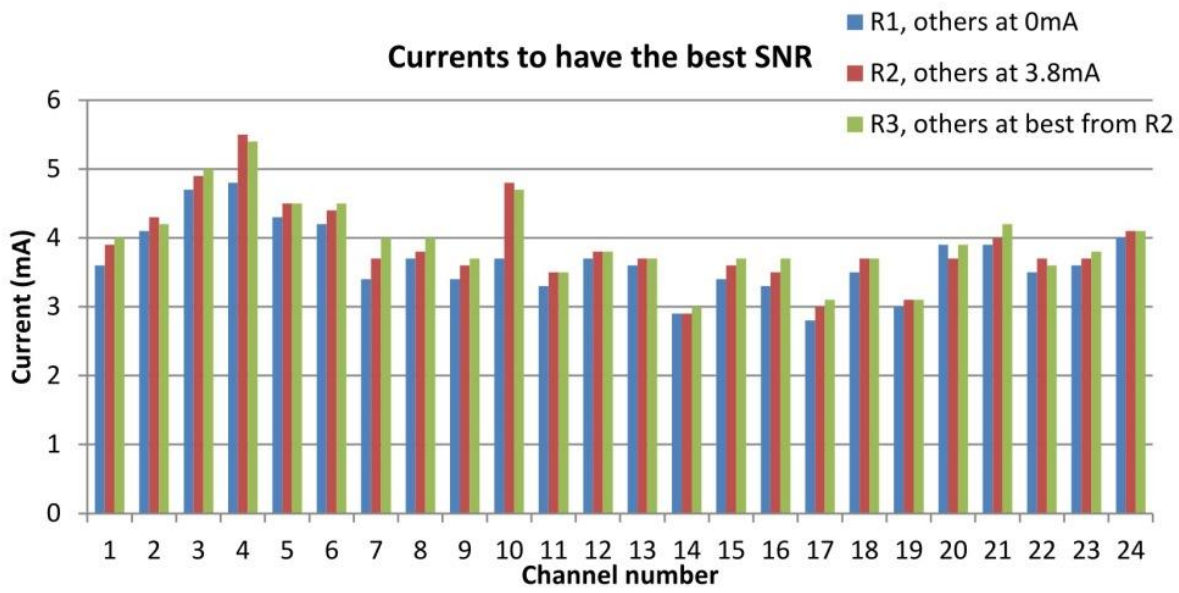

FIGURE 7.4: Three rounds (R1 to R3) of measurements to find the optimum operational currents (which are the currents measured at R3 or green bars).

7.5 Finding Optimum Operational Currents for VCSELs

One of the challenges of the system was that the VCSELs in the array were not identical. This means that they had different threshold currents, thermal behaviors, and beam profiles. Therefore, we had to find the optimum operational currents for each one of the lasers in order to obtain the best SNR from them. For that purpose, first we turn off all the other channels and found the currents at which we had the highest SNRs for each one of the channels, then we ran all the channels at 3.8 mA (the average of the optimum currents from the previous round) and again found the optimum currents for each one of the VCSELs. At the third round, we ran all the other channels at their optimum currents (from last round) and found the new optimum currents for each one of the channels again. This way, after three rounds of measurements we found the optimum operational currents for each one of the laser diodes in the array. Results of the three round of measurements and the optimum currents can be seen in fig. 7.4.

7.6 Parallel Imaging

We scanned a diverging–converging planar flow channel, using the 24 channel VCSEL array parallel imaging system. The flow channel is shown in fig. 7.5 (a). A diluted mixture of water and homogenized milk was pushed through the flow channel and scatterers

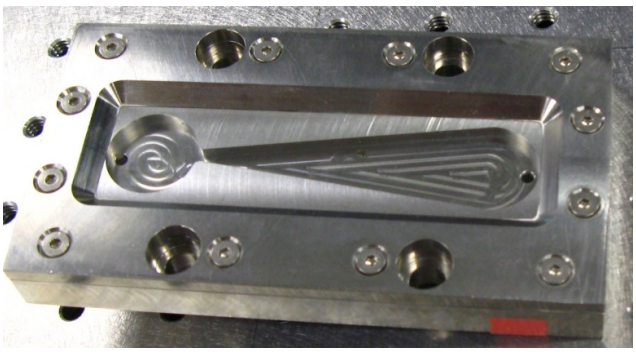

(a)

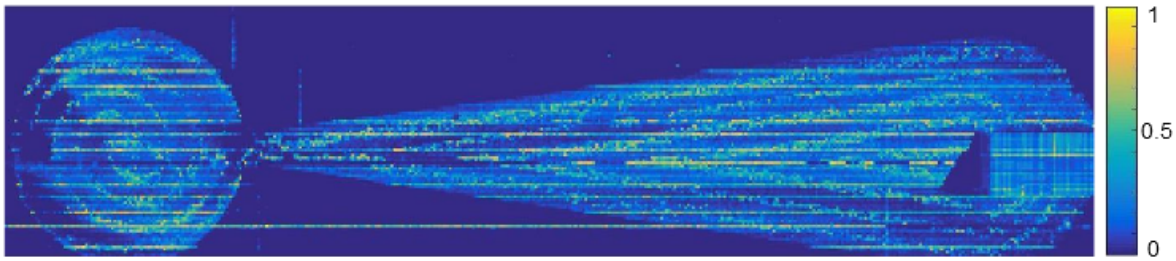

(b)

FIGURE 7.5: (a) Flow channel and (b) Doppler flowmetry parallel imaging result of the flow channel containing diluted milk.

were the fat particles presented in milk. The density of the fat particles can be controlled by the diluting proportion of the mixture. This flow channel was a simple target to test the system's ability to detect flow as a lab-controlled model for blood perfusion. The scan result can be seen in fig. 7.5 (b). Scan of the flow channel was carried out as four horizontal sweeps of the array. This means that we moved the array horizontally for four times along the flow channel to create the image. Horizontal step size was taken to be the same length as the pitches of the VCSELs in the array, which was 220 µm. After finishing each one of the sweeps, array was moved to its original place and then it was moved 5280 µm (24 $\times$ 220 µm) vertically to start the next sweep. Considering four horizontal sweeps, the width of the scan area was about 20.9 mm (95 $\times$ 220 µm). To cover the whole length of the flow channel, we included about 451 steps in the horizontal scan. This means that the length of the imaging area was 99 mm (450 $\times$ 220 µm). At each step time domain sequences of the voltage signal from the terminals of the VCSELs were saved into a PC using a Data Acquisition Card. We applied the fast Fourier transform to convert the time domain signals into frequency domain spectra and a set of Doppler signals were calculated by means of this frequency spectra. Figure 7.5 (b) is the result of signal processing.

At the time when I approached the end of my PhD, the parallel imaging system was still under construction and there were some issues with the optical system which needed to be addressed. The rest of the chapter, presents paper G which is the discovered results of the enhancement in the SNRs of the channels in a concurrent operation.

7.7 Paper G

Tucker, John R and **Mowla, Alireza** and Herbert, Jeremy and Fuentes, Miguel A and Freakley, Craig S and Bertling, Karl and Lim, Yah Leng and Matharu, Ranveer S and Perchoux, Julien and Taimre, Thomas and Wilson, Stephen J. and Rakić, Aleksandar D, "Self-mixing sensing system based on uncooled vertical-cavity surface-emitting laser array: linking multichannel operation and enhanced performance," Opt. Lett. **39**, 394–397 (2014).

Abstract: We compare the performance of a self-mixing (SM) sensing system based on an uncooled monolithic array of 24×1 Vertical-Cavity Surface-Emitting Lasers (VCSELs) in two modes of operation: single active channel and the concurrent multichannel operation. We find that the signal-to-noise ratio (SNR) of individual self-mixing sensors in a VCSEL array is markedly improved by multichannel operation, as a consequence of the increased operational temperature of the sensors. The performance improvement can be further increased by manufacturing VCSEL arrays with smaller pitch. This has the potential to produce an imaging system with high spatial and temporal resolutions that can be operated without temperature stabilization.

Body: Many systems utilise a monolithic array of semiconductor lasers to increase the capability and functionality of single channel systems [81,83,194,195]. Such systems are able to dramatically increase the amount of data that can be acquired within a certain time frame or the amount of time it takes to obtain a certain amount of data. This is particularly important in the context of biomedical and industrial applications that have unstable or dynamically changing flow velocities.

In recent times, there has also been increasing interest in acquiring images with a monolithic array of lasers using the self-mixing (SM) effect [81,83]. This sensing technique is based on the interference of light reflected from an external target with the light inside the laser cavity, which leads to measurable changes in the output power and the laser junction voltage. This is an attractive setup as the laser is used as both the source and detector, which greatly reduces the complexity of the optical alignment and makes the system more compact.

Initially, it may seem that simultaneous multichannel operation of SM sensors may lead to problems common in other systems based on a monolithic array of lasers such as optical, electrical and thermal crosstalk (XT). A fraction of light emitted from a vertical-cavity surface-emitting laser (VCSEL) in a dense monolithic array will, upon reflection from

the external target, inevitably fall on the neighbouring elements in the array [196]. In a SM system based on such geometries optical XT may occur through the injection locking between different channels (VCSELs) of the array [197, 198]. However, this is extremely unlikely to occur in most applications as injection locking requires a number of conditions to be met including mutual coherence and mode matching. This may be further avoided by a small change in the operating temperature or injection current of the laser [199]. Electrical XT may also arise through electrical connections to the laser array but other systems have been developed where this form of XT is insignificant at frequencies below 1 GHz [194, 200, 201]. Electrical XT may also be caused by the sharing of carriers via resistive paths in the laser array itself although this can be circumvented with appropriate semiconductor isolation structures [202].

Based on the results from other laser array based systems [195], it may also be expected that the heat generated by multiple lasers may decrease the performance of individual SM sensors. Surprisingly, we find that the signal-to-noise ratio (SNR) of a monolithically integrated SM VCSEL sensor arrays is actually enhanced rather than reduced with multichannel operation. This is a consequence of the following phenomenon: maximum SNR achievable (over a range of operating injection currents) is increasing with the laser temperature, a result akin to that observed by Matharu et al. in a single channel system [122]. This increase is due to changes in a number of different temperature dependent parameters such as gain, voltage, and series resistance. However, there is currently no comprehensive theoretical model to determine which parameters are limiting or dominating this increase in the SNR with temperature. In this letter, we focus on describing an experiment that proves the increase in maximum SNR with multichannel operation in SM VCSEL array based sensors and discussing how the performance may be further enhanced through the array design.

The effect of multichannel operation in SM sensors was investigated in an uncooled 24$\times$1 VCSEL array custom manufactured by Litrax Technology Co., Ltd with the system shown in Fig. 1. The VCSEL array was mounted in a surface mount ceramic package and individual VCSELs were wire-bonded to pins of the package. The VCSELs are based on proton implanted technology and have a pitch of 220 µm. A FLIR i7 thermal imaging camera was used to examine the temperature profile of the array for different operational settings.

A single macro lens (f=105 mm) was employed to focus all 24 laser beams onto a rotating disk. The target was placed 35 cm from the laser array, which resulted in a beam spacing of 220 µm and a magnification factor of 1. The laser array was oriented vertically.

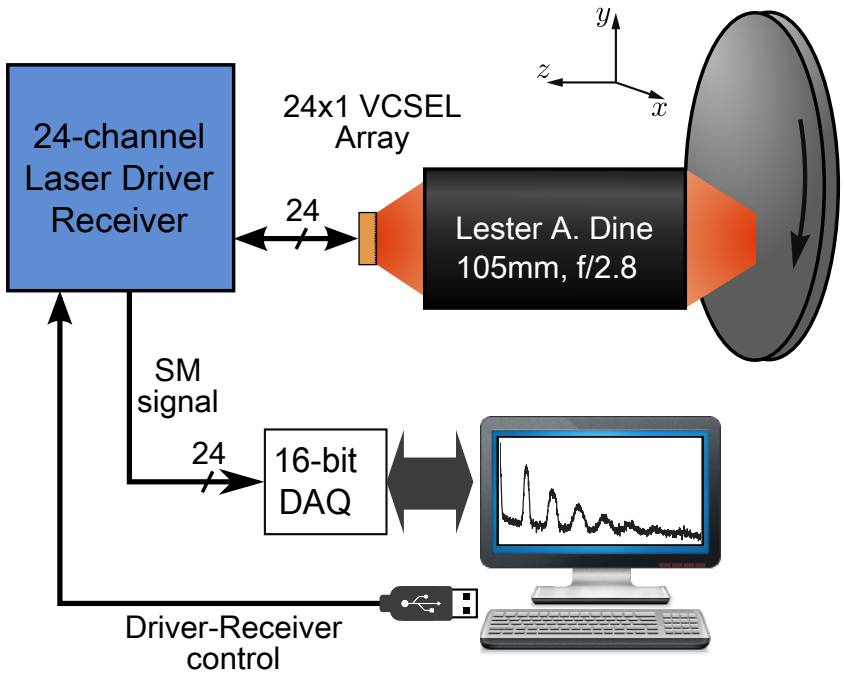

FIGURE 7.6: Experimental setup for measuring velocity on a rotating disk. The disk is tilted around the vertical axis by 5° to produce a small velocity component in the direction of the laser beam.

The aluminium disk, 10 cm in diameter, was sandblasted to provide a rotating diffusive target. The disk is tilted around the vertical axis by 5° to produce a small velocity component in the direction of the laser beam. The disk was driven by a DC servo motor with a 43:1 gear reduction controlled by an Elmo Whistle motor controller. The stability of the disk's angular velocity for the duration of the experiments was better than 1%, as established by monitoring the frequency of the motor's rotary encoder. A custom built 24-channel laser driver—receiver was used to individually bias each laser with a constant injection current. The SM signals were obtained through monitoring variation in the voltage across the laser terminals for each of the individual VCSEL terminals.

Each channel had a sampling rate of 62.5 kHz. The power spectral density of the time domain signal was calculated in the LabVIEW programming environment to obtain the SM signal spectrum and 32 consecutive spectra were averaged. The Doppler frequency was extracted by fitting the power spectral density spectrum to the following function [79],

$$Fit(f) = a + \frac{b}{f^c} + d\,\exp\left(-\left(\frac{f - f_D}{g}\right)^2\right), \tag{7.2}$$

where parameter a models flat (white) noise, b and c model $1/f$ noise, and, g and f_D

model a Gaussian distribution of Doppler components. The SNR was obtained by taking the ratio between the peak value of the fundamental spectral feature of the Doppler signal and a.

In this work, we are interested in uncooled operation of the laser array as Peltier devices consume high amounts of power and make a sensing system less compact and portable. For uncooled operation, the temperature of a single laser device may be increased by increasing the injection current or the amount of power dissipated as heat [203]. In array based operation, the heat generated by a single laser spreads to other lasers in the array. The resulting temperature rise from a neighbouring laser is inversely proportional to the pitch [204], which leads to the central lasers showing the highest rise in temperature when all lasers are operating simultaneously. To examine the effect of multichannel operation on the performance of a SM sensor we first measured the SNR of one of the central lasers (Channel 12) for a wide range of bias currents from threshold to 10 mA. We then remeasured the SNR for the same bias currents while turning on other lasers in the array. To maximise the temperature rise we simultaneously turned on the remaining 23 lasers in the array. These lasers, which we will subsequently referred to as the neighbouring lasers, were biased at the same injection current while the bias current of the VCSEL under investigation was changed. Figure 2 shows the SNR of the central (sensing) VCSEL over a range of bias currents.

Each curve corresponds to a different operating current in all neighbouring VCSELs. The well-known increase and subsequent decrease of SNR with bias current can be observed for all operating conditions [205, 206]. For single channel operation (neighbouring VCSELs not operating), the SNR increases rapidly above threshold before reaching a maximum. The SNR then gradually decreases as the injection current is increased beyond the current for the maximum SNR.

When the currents in the neighbouring lasers were increased to 2 mA, which is below the threshold current of each laser, the SNR in the sensing VCSEL increased significantly. This indicates that the increase in SNR is not due to external optical XT as the lasers have no observable signal level below the threshold current. Subsequent measurements on a probing station showed that the electrical isolation between adjacent elements was of the order of 5 MΩ. The injection current for the optimum SNR also slightly increases when the neighbouring lasers are turned on, which follows the increase in the threshold current with temperature as observed in a single channel system [122, 207]. This suggests that the increase in SNR is due solely to the temperature rise in the sensing laser. Further increase in operating current of the neighbouring VCSELs leads to a monotonic increase in maximum achievable SNR.

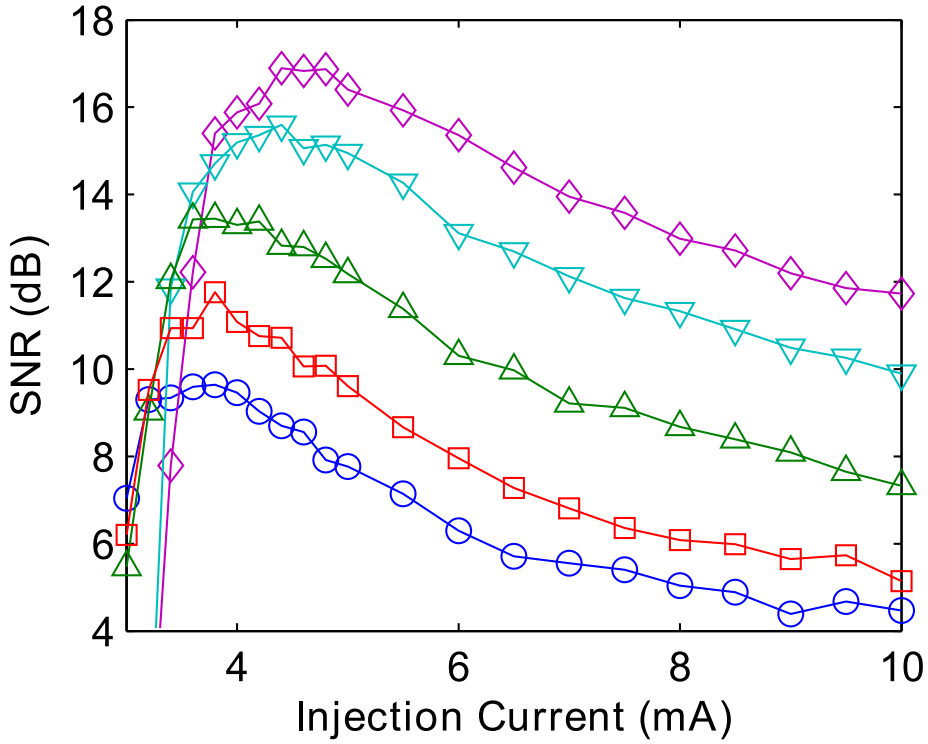

FIGURE 7.7: SNR of central laser (Channel 12) versus injection current with different levels of current in neighbouring lasers. The current in the neighbouring lasers are all biased at the same current while the current of the central laser is varied.(circles - Single Channel, squares - Multichannel 2 mA, up triangles - Multichannel 5 mA, down triangles - Multichannel 8 mA, diamonds - Multichannel 10 mA).

To investigate this further, we measured the SNR of the central laser (Channel 12) while simultaneously operating six other lasers on the array. In each experiment, all seven lasers were equally spaced. Three different sets of equal spacing were investigated (660, 440 and 220 µm). The injection current in all of the neighbouring lasers was set to 10 mA. Therefore, in each experiment, the same electrical power was delivered to the laser chip. To examine this issue in more detail, we used a thermal IR camera to obtain the temperature profile of the array. Figure 3 shows a close-up photo of the array as well as the thermal images for the different separation distances used in the experiment.

Figure 4 shows the SNR of the central VCSEL as a function of injection current. Three curves correspond to three different separation configurations, with corresponding temperature distributions shown in Fig. 3. Clearly, the SNR increases as the separation distance between lasers decreases, which can be attributed to the higher temperature of the central (sensing) VCSEL due to the heating sources being concentrated nearer the sensing VCSEL.

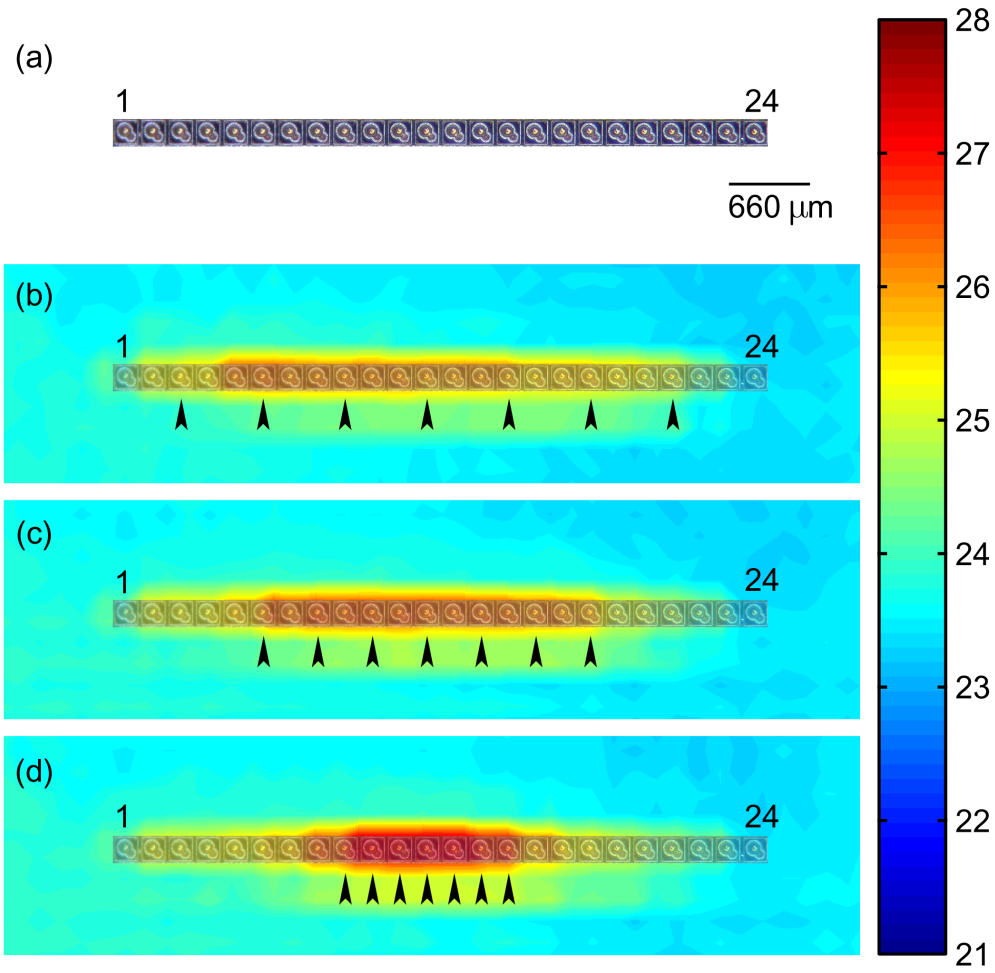

FIGURE 7.8: Close up photo of the array and thermal images for the different separation distances used for the experiments in Fig. 4. a) Photo, b) 660 µm spacing, c) 440 µm spacing, d) 220 µm spacing. Channel 1 is located at the left hand side of the images.

A consequence of this result is that the SNR may be further improved by manufacturing an array with elements spaced more closely together. This would not only increase the spatial resolution of an imaging system based on this array, but also allow for a smaller lens to be used due to the smaller array size, making the whole optical system more compact.The temperature rise in the array may also be increased by increasing the element diameter as suggested by Osinski et al [204]. However, larger diameter VCSELs may exhibit multiple transverse modes, which can affect the accuracy and performance of SM sensors [193].

While a change in operating current and temperature strongly affects the SNR of the system it also affects the emission wavelength of the lasers. We show here that this substantial change in lasing wavelength has predictable, and almost negligible effect,

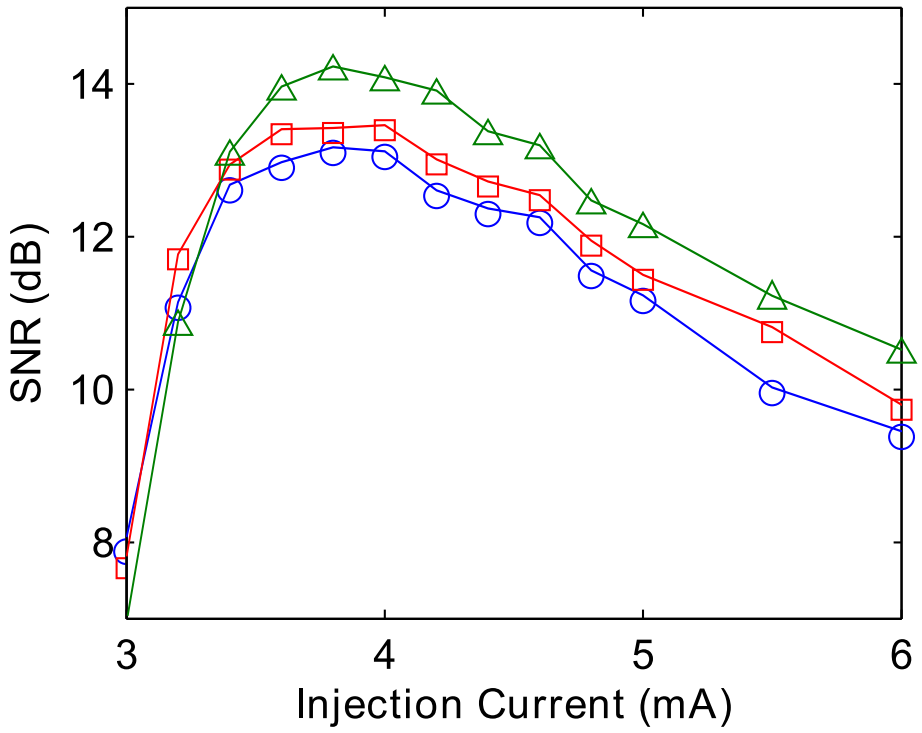

FIGURE 7.9: SNR of central laser (Channel 12) versus injection current with simultaneous operation of six neighbouring lasers biased at 10 mA. There is an equal separation distance between lasers with the separation distance varying for different experiments. (circles - 660 µm spacing, squares- 440 µm spacing, triangles - 220 µm spacing).

on the Doppler frequency and calculated target velocity. The dependence of the lasing wavelength on current and heatsink temperature was measured by placing the laser chip in a temperature-controlled mount. The VCSEL wavelength dependence on current and temperature measured on a stand-alone VCSEL of the same design as the VCSEL array used in this work. Measurements were executed for a range of temperatures between 10 and 60 $^{\circ}C$ and currents up to 10 mA. Polynomial fit to these experiments can be conveniently represented by the following function:

$$\lambda(T, I) = 844.1 + 0.063T + 0.066I + 0.00029TI + 0.0128I^2, \tag{7.3}$$

where T is the heatsink temperature in $^{\circ}C$, and I is the laser current in mA, and λ is wavelength in nm. The change in lasing wavelength with current is mainly caused by heating of the laser cavity [208].

At each temperature–current pair, a SM Doppler spectrum was acquired and the Doppler frequency was extracted. The maximum shift in Doppler frequency caused by

the combined current and temperature change was 16 Hz (from 2.784 kHz to 2.768 kHz) which corresponds to a fractional change of approximately 0.6 %. This systematic error may be removed by calculating the wavelength at any given point in the current–temperature space using (2).

Figure 3 shows that temperature variation under different operating regimes of our array is much smaller than the current—temperature range used in this experiment. Therefore, we can safely conclude that the effect of current and temperature change in an uncooled VCSEL array will not only be predictable and easily removable but shows negligible effect on the performance of such arrays. This means that there is no significant reduction in the accuracy of the velocity determination with multichannel operation of a SM array based sensor, which allows it to be used for a wide range of sensing applications.

In summary, we have compared the performance of single channel and multichannel operation of an uncooled single mode monolithic 24×1 VCSEL array in a SM sensing system. We found that the SNR of monolithically integrated SM sensor arrays is inherently enhanced through multichannel operation, as a result of the increased operational temperature of the sensor. This effect can be augmented by reducing the spacing between VCSELs on the array or increasing the diameter of each laser. Finally, the temperature rise due to multichannel operation had no significant effect on the measured Doppler frequency, which corresponds to no significant change in the accuracy of the measured velocity. These findings suggest that SM imaging systems based on VCSEL arrays have the potential to produce images with high spatial resolutions at high frame rates. These features make parallel SM sensing systems especially attractive for biomedical and industrial applications where there are unstable or dynamically changing flow velocities.

Chapter 8

Conclusions

Early skin cancer detection is achieved by sensing a kind of abnormality in the cancerous tissue which can be called a biomarker as well. This can be the visual shape of the cancerous tissue or its optical properties or a functional marker such as abnormal blood perfusion. For instance, the refractive index of cancerous tissue is different from normal tissues and blood perfusion is abnormal around these cells [5]. Based on the fact that infrared light can penetrate the skin tissue by a few millimeters at wavelengths such as 850 nm, the biomarkers of the affected tissue can be investigated using near-infrared semiconductor lasers.

In this project I studied the biology of different cancerous skin tissues and investigated the abnormalities of these tissues. In particular, I focused my studies on neovascularization or angiogenesis (development of blood vessel networks in the cancerous tissues to provide cancer cells with oxygen and nutrition and carry away the waste) and also on the changes in the optical properties (such as scattering and absorption coefficients) that may happen to cancerous tissues due to cancerous activities. After choosing biomarkers that can be used in a detection procedure, I chose LFI as a sensing technique to be used in this thesis. Because there was no access to biological tissue to be used in *in vivo* measurements, I developed technologies to make tissue phantoms. I made state of the art, multi-layer skin tissue phantoms including cancerous tissue models. I applied the LFI technique to construct images of these tissue phantoms. Furthermore, I developed laser feedback tomography systems to build three dimensional images of the same samples. In addition, I proposed and examined a novel dual-modality imaging technique that improved the capabilities of the imaging system dramatically. In parallel with experimental works, I developed a powerful object-oriented Monte Carlo simulation engine, which helped me in

conceptualizing ideas and predicting results, and also in discussing the experimental results more effectively. To conclude, a summary of the findings and suggestions for future works will be presented in the remainder of this chapter.

8.1 Summary of Findings

This dissertation's findings encompass theoretical, experimental, and simulation portions. On the theoretical side, laser Doppler flowmetry and confocal reflectance microscopy were proposed and used as two modalities that can be used in laser imaging skin cancer detection practices. In addition, a combination of the two aforementioned techniques was also proposed and performed which improved the effectiveness of the imaging systems. A comprehensive theoretical study of the effects of different system parameters on the morphology of the Doppler spectrum was conducted which can play an important role in designing laser Doppler velocimeters and flowmeters.

On the experimental side, the technology for making tissue phantoms was introduced to the group and agar and silicone based tissue phantoms were made and used in different imaging setups during the thesis. Moreover, LFI was proposed and implemented in imaging applications to make Doppler flowmetry and confocal reflectance images. It was also used to realize the dual-modality imaging technique to combine Doppler flowmetry and confocal reflectance imaging in an integrated system. Optical sectioning was carried out using LFI systems which includes a high numerical aperture focused beam providing images at different depths of cancerous tissue phantoms. As a result of being able to perform depth sectioning, a laser feedback tomography system was proposed and applied to image a cancerous skin tissue phantom. A large number of slices of the sample, imaged using this system, were concatenated to make tomographic images of the affected volume that has different optical properties compared to its surrounding volumes. Experimental work was also carried out on a parallel imaging system including a 24-channel VCSEL array as an alternative way to improve the speed of imaging. Preliminary results of the parallel read out system was presented and the technical considerations of the system were discussed.

Finally, I also performed numerical modeling by means of the Monte Carlo method. A fast and efficient Monte Carlo simulation engine was prepared using object-oriented MATLAB programming. I used Monte Carlo simulation during my thesis to model the experiments, optical systems, and sample structures, in a numerical way. The results of the numerical models were then used to validate experimental results. Simulations was

also used to present and discuss results where experiments were hard or impossible to conduct. For instance, in paper E the possible improvement in skin cancer detection using the proposed dual-modality imaging technique was numerically surveyed. As another example, in paper B the effects of the beam numerical aperture and distribution of particle velocities within the beam spot on Doppler spectrum were investigated using only Monte Carlo simulation. Therefore, we took advantage of the validated and reliable Monte Carlo engine to extend the scope of our hypotheses and analyses. Monte Carlo was also used as a tool to gain access to a range of characteristics of the optical system that gave us a deeper understanding of their role within the system, such as the reflection profile of the photons from rough surfaces (discussed in paper B) and also sensing volume of the beam for an LFI system.

8.2 Future Work

What has been done in this thesis is quite extensive. Despite this, in most of the covered areas, there is still a huge capacity for further work, as proposed ideas are novel and still not mature. The use of optical beam to interrogate tissue targets, which is the foundation of this work, is also the basic for numerous other optical techniques. These optical methods are competing to be accepted as tools of choice in *in vivo* imagining applications. Therefore, deeper knowledge in this area paves the way toward such efficient tools. One the other hand, deeper understanding of biological mechanisms involved in multistep development of human tumors, helps to give insight into new modalities and biomarkers which can be utilized in these imaging systems.

Continuing the research that has been carried out in the area of tissue phantoms is also strongly recommended. Tissue phantoms are used extensively in different research areas and having the technology to make complicated and state-of-the-art tissue phantoms, is not just useful in optical imaging methods, but also can be of great importance in other medical diagnostic and therapeutic research areas.

The transition from tissue phantoms to biological tissues in clinical environments is the ultimate goal for the laser feedback tomography technique proposed for skin cancer detection applications, discussed in section 6.2, and consequently the ultimate goal of this work. Although this transition is quite challenging, we believe it is feasible. The first step can be imagined as conducting experiments on biological healthy skin tissues. Ethics for these experiments should be provided and volunteers should be hired. New technologies as fast scanning mirrors and high speed electronics should be provided to

speed up the imaging process as much as possible. Therefore, motion and other artefact noises and fatigue in the volunteer can be avoided. Skin is an inhomogeneous tissue (compared to homogeneous tissue phantoms) and new methods should be acquired to take the inhomogeneity of skin into account. Skin sample should be fixed to avoid the involuntary movements and diffuse reflectance from the surface of the skin should be dealt with, by using immersion oils for instance. Second step can be imagined as moving the optical system to a controlled clinical room where a real patient is. Measurements are *in vivo*, therefore proper ethical clearance should be provided and volunteers with specific type of lesion (as required) should be looked for, informed well, and asked to be involved, while procedures and hazards should also be explained well. Moving optical system from a photonics lab where all the sources of noise are well-controlled to a clinical room is also challenging. For instance, using an optical table in the lab suppresses most of the vibrational noises, when it is impossible to move an optical table to a clinical room. All the necessary equipment to conduct the experiment should be packed neatly to make the apparatus as small as possible. These are just to name a few challenges that this transition may impose.

Employing LFI to image new modalities is another promising procedure that can follow this work. There are a large number of modalities that have been applied in other optical imaging techniques but have not still been applied in LFI systems. However, I believe LFI has the capability of using some of these new modalities. For instance, elastography which is mapping the mechanical properties or elasticity of soft tissues was proposed as a medical imaging modality to be used in oncology applications [209]. Techniques such as supersonic shear imaging [210], magnetic resonance elastography [211], and optical coherence elastography [212] were then proposed and implemented as elastography embodiments. Considering the fact that LFI can be used to image the propagation of mechanical waves [213], we believe this technique can be used for elastography as well.

Finally, further work in the area of Monte Carlo simulation is also strongly recommended. The basic Monte Carlo software which was developed so far has the capability of being extended in different directions. This is a powerful tool to analyze the photon matter interactions not only in the case of LFI but in all applications requiring the knowledge of photon transport through a complex optical system. For instance, including polarization state in the characteristics of photons and alterations that may happen to the polarization state of the photons due to the scattering events, is a promising study that can be performed through Monte Carlo simulations. This is especially of interest for polarization sensitive techniques. Considering the fact that LFI is also a polarization sensitive method, this study can also help in conducting polarization selective LFI imaging.

Bibliography

[1] C. M. Olsen, P. F. Williams, and D. C. Whiteman, "Turning the tide? Changes in treatment rates for keratinocyte cancers in Australia 2000 through 2011," J. Am. Acad. Dermatol. (2014).

[2] D. R. Bickers, H. W. Lim, and D. Margolis, "The burden of skin diseases: 2004 a joint project of the american academy of dermatology association and the society for investigative dermatology," J. Am. Acad. Dermatol. **55**, 490–500 (2006).

[3] L. J. Loescher, M. Janda, H. P. Soyer, K. Shea, and C. Curiel-Lewandrowski, "Advances in skin cancer early detection and diagnosis," in "Seminars in oncology nursing," , vol. 29 (Elsevier, 2013), vol. 29, pp. 170–181.

[4] G. Argenziano, S. Puig, I. Zalaudek, F. Sera, R. Corona, M. Alsina, F. Barbato, C. Carrera, G. Ferrara, A. Guilabert, D. Massi, J. Moreno-Romero, C. Munoz-Santos, G. Petrillo, S. Segura, H. Soyer, R. Zanchini, and J. Malvehy, "Dermoscopy improves accuracy of primary care physicians to triage lesions suggestive of skin cancer," J. Clinical Oncology **24**, 1877–1882 (2006).

[5] P. Calzavara-Pinton, C. Longo, M. Venturini, R. Sala, and G. Pellacani, "Reflectance confocal microscopy for in vivo skin imaging," Photochemistry and photobiology **84**, 1421–1430 (2008).

[6] N. E. Feit, S. W. Dusza, and A. A. Marghoob, "Melanomas detected with the aid of total cutaneous photography," British J. Dermatol. **150**, 706–714 (2004).

[7] G. Monheit, A. B. Cognetta, L. Ferris, H. Rabinovitz, K. Gross, M. Martini, J. M. Grichnik, M. Mihm, V. G. Prieto, P. Googe, R. King, A. Toledano, N. Kabelev, M. Wojton, and D. Gutkowicz-Krusin, "The performance of MelaFind: a prospective multicenter study," Archives of Dermatology **147**, 188–194 (2011).

[8] S. Donati, "Developing self-mixing interferometry for instrumentation and measurements," Laser Photonics Rev. **6**, 393–417 (2012).

[9] S. Donati and M. Norgia, “Self-mixing interferometry for biomedical signals sensing,” IEEE J. Select. Top. in Quant. Electron. **22** (2014).

[10] T. Taimre, M. Nikolić, K. Bertling, Y. L. Lim, T. Bosch, and A. D. Rakić, “Laser feedback interferometry: A tutorial on the self-mixing effect for coherent sensing,” Advances in Optics and Photonics **7**, 570–631 (2015).

[11] E. Salomatina, B. Jiang, J. Novak, and A. N. Yaroslavsky, “Optical properties of normal and cancerous human skin in the visible and near-infrared spectral range,” Journal of Biomedical Optics **11**, 064026–064026 (2006).

[12] M. Stücker, I. Horstmann, C. Nüchel, A. Röchling, K. Hoffmann, and P. Altmeyer, “Blood flow compared in benign melanocytic naevi, malignant melanomas and basal cell carcinomas.” Clinical and experimental dermatology **24**, 107–111 (1999).

[13] M. Stücker, M. Esser, M. Hoffmann, U. Memmel, A. H. Ller, C. Von Bormann, K. Hoffmann, and P. Altmeyer, “High-resolution laser doppler perfusion imaging aids in differentiating between benign and malignant melanocytic skin tumours,” Acta Derm Venereol **82**, 25–29 (2002).

[14] D. Hanahan and R. A. Weinberg, “Hallmarks of cancer: the next generation,” cell **144**, 646–674 (2011).

[15] A. Seifalian, K. Chaloupka, and S. Parbhoo, “Laser doppler perfusion imaging–a new technique for measuring breast skin blood flow,” International Journal of Microcirculation **15**, 125–130 (1995).

[16] K. Wårdell, A. Jakobsson, and G. E. Nilsson, “Laser doppler perfusion imaging by dynamic light scattering,” Biomedical Engineering, IEEE Transactions on **40**, 309–316 (1993).

[17] S. J. Miller, “Biology of basal cell carcinoma (part i),” Journal of the American Academy of Dermatology **24**, 1–13 (1991).

[18] L. Wang, S. L. Jacques, and L. Zheng, “MCML–Monte Carlo modeling of light transport in multi-layered tissues,” Comp. Meth. Prog. Biomedicine **47**, 131–146 (1995).

[19] G. Argenziano and H. P. Soyer, “Dermoscopy of pigmented skin lesions–a valuable tool for early,” The lancet oncology **2**, 443–449 (2001).

[20] G. Argenziano, H. P. Soyer, S. Chimenti, R. Talamini, R. Corona, F. Sera, M. Binder, L. Cerroni, G. De Rosa, G. Ferrara *et al.*, "Dermoscopy of pigmented skin lesions: results of a consensus meeting via the internet," Journal of the American Academy of Dermatology **48**, 679–693 (2003).

[21] V. Dal Pozzo, C. Benelli, and E. Roscetti, "The seven features for melanoma: a new dermoscopic algorithm for the diagnosis of malignant melanoma." European journal of dermatology: EJD **9**, 303–308 (1999).

[22] J. Kim and K. Nelson, "Dermoscopic features of common nevi: a review," G Ital Dermatol Venereol **147**, 141–8 (2012).

[23] S. Puig, N. Cecilia, and J. Malvehy, "Dermoscopic criteria and basal cell carcinoma," G Ital Dermatol Venereol **147**, 135–40 (2012).

[24] R. Hofmann-Wellenhof, A. Blum, I. H. Wolf, D. Piccolo, H. Kerl, C. Garbe, and H. P. Soyer, "Dermoscopic classification of atypical melanocytic nevi (clark nevi)," Archives of dermatology **137**, 1575–1580 (2001).

[25] R. J. Friedman, D. Rigel, M. K. Silverman, A. W. Kopf, and K. A. Vossaert, "Malignant melanoma in the 1990s: The continued importance of early detection and the role of physician examination and self-examination of the skin," CA: a cancer journal for clinicians **41**, 201–226 (1991).

[26] H. Pehamberger, A. Steiner, and K. Wolff, "In vivo epiluminescence microscopy of pigmented skin lesions. i. pattern analysis of pigmented skin lesions," Journal of the American Academy of Dermatology **17**, 571–583 (1987).

[27] S. W. Menzies, K. Westerhoff, H. Rabinovitz, A. W. Kopf, W. H. McCarthy, and B. Katz, "Surface microscopy of pigmented basal cell carcinoma," Archives of Dermatology **136**, 1012–1016 (2000).

[28] M. Elbaum, A. W. Kopf, H. S. Rabinovitz, R. G. Langley, H. Kamino, M. C. Mihm, A. J. Sober, G. L. Peck, A. Bogdan, D. Gutkowicz-Krusin, M. Greenebaum, S. Keem, M. Oliviero, and S. Wang, "Automatic differentiation of melanoma from melanocytic nevi with multispectral digital dermoscopy: a feasibility study," Journal of the American Academy of Dermatology **44**, 207–218 (2001).

[29] L. Andreassi, R. Perotti, P. Rubegni, M. Burroni, G. Cevenini, M. Biagioli, P. Taddeucci, G. Dell'Eva, and P. Barbini, "Digital dermoscopy analysis for the differentiation of atypical nevi and early melanoma: a new quantitative semiology," Archives of Dermatology **135**, 1459–1465 (1999).

[30] H. K. Kim, N. Tucker, F. Debernardis, and A. H. Hielscher, "Melanoma detection and characterization with a 6-layered multispectral model," in "Optics and the Brain," (Optical Society of America, 2016), pp. JTu3A–26.

[31] R. Hofmann-Wellenhof, G. Pellacani, J. Malvehy, and H. P. Soyer, *Reflectance confocal microscopy for skin diseases* (Berlin, Springer Science & Business Media, 2012).

[32] C. Longo, F. Farnetani, S. Ciardo, A. Cesinaro, E. Moscarella, G. Ponti, I. Zalaudek, G. Argenziano, and G. Pellacani, "Is confocal microscopy a valuable tool in diagnosing nodular lesions? A study of 140 cases," British Journal of Dermatology **169**, 58–67 (2013).

[33] A. Scope, U. Mahmood, D. Gareau, M. Kenkre, J. Lieb, K. Nehal, and M. Rajadhyaksha, "In vivo reflectance confocal microscopy of shave biopsy wounds: feasibility of intraoperative mapping of cancer margins," British Journal of Dermatology **163**, 1218–1228 (2010).

[34] A. Rishpon, N. Kim, A. Scope, L. Porges, M. C. Oliviero, R. P. Braun, A. A. Marghoob, C. A. Fox, and H. S. Rabinovitz, "Reflectance confocal microscopy criteria for squamous cell carcinomas and actinic keratoses," Archives of Dermatology **145**, 766–772 (2009).

[35] S. Segura, S. Puig, C. Carrera, J. Palou, and J. Malvehy, "Development of a two-step method for the diagnosis of melanoma by reflectance confocal microscopy," Journal of the American Academy of Dermatology **61**, 216–229 (2009).

[36] R. H. Webb, "Confocal optical microscopy," Reports on Progress in Physics **59**, 427 (1996).

[37] W. Drexler, M. Liu, A. Kumar, T. Kamali, A. Unterhuber, and R. A. Leitgeb, "Optical coherence tomography today: speed, contrast, and multimodality," Journal of biomedical optics **19**, 071412–071412 (2014).

[38] M. Minsky, "Memoir on inventing the confocal scanning microscope," Scanning **10**, 128–138 (1988).

[39] J. White, W. Amos, and M. Fordham, “An evaluation of confocal versus conventional imaging of biological structures by fluorescence light microscopy.” The Journal of Cell Biology **105**, 41–48 (1987).

[40] M. Rajadhyaksha, M. Grossman, D. Esterowitz, R. H. Webb, and R. R. Anderson, “In vivo confocal scanning laser microscopy of human skin: melanin provides strong contrast,” Journal of Investigative Dermatology **104**, 946–952 (1995).

[41] L. E. Meyer, N. Otberg, W. Sterry, and J. Lademann, “In vivo confocal scanning laser microscopy: comparison of the reflectance and fluorescence mode by imaging human skin,” Journal of Biomedical Optics **11**, 044012–044012 (2006).

[42] S. Astner, S. Dietterle, N. Otberg, H.-J. Röwert-Huber, E. Stockfleth, and J. Lademann, “Clinical applicability of in vivo fluorescence confocal microscopy for noninvasive diagnosis and therapeutic monitoring of nonmelanoma skin cancer,” Journal of biomedical optics **13**, 014003–014003 (2008).

[43] D. Huang, E. A. Swanson, C. P. Lin, J. S. Schuman, W. G. Stinson, W. Chang, M. R. Hee, T. Flotte, K. Gregory, and C. A. Puliafito, “Optical coherence tomography,” Science (New York, NY) **254**, 1178 (1991).

[44] J. M. Schmitt, “Optical coherence tomography (OCT): a review,” IEEE Journal of Selected Topics in Quantum Electronics **5**, 1205–1215 (1999).

[45] A. F. Fercher, W. Drexler, C. K. Hitzenberger, and T. Lasser, “Optical coherence tomography-principles and applications,” Reports on progress in physics **66**, 239 (2003).

[46] J. Strasswimmer, M. C. Pierce, B. H. Park, V. Neel, and J. F. de Boer, “Polarization-sensitive optical coherence tomography of invasive basal cell carcinoma,” Journal of Biomedical Optics **9**, 292–298 (2004).

[47] J. M. Olmedo, K. E. Warschaw, J. M. Schmitt, and D. L. Swanson, “Optical coherence tomography for the characterization of basal cell carcinoma in vivo: A pilot study,” Journal of the American Academy of Dermatology **55**, 408–412 (2006).

[48] T. Gambichler, A. Orlikov, R. Vasa, G. Moussa, K. Hoffmann, M. Stücker, P. Altmeyer, and F. G. Bechara, “In vivo optical coherence tomography of basal cell carcinoma,” Journal of Dermatological Science **45**, 167–173 (2007).

[49] M. Mogensen, T. Joergensen, B. M. Nürnberg, H. A. Morsy, J. B. Thomsen, L. Thrane, and G. B. Jemec, "Assessment of optical coherence tomography imaging in the diagnosis of non-melanoma skin cancer and benign lesions versus normal skin: Observer-blinded evaluation by dermatologists and pathologists," Dermatologic Surgery **35**, 965–972 (2009).

[50] Z. Chen, T. E. Milner, S. Srinivas, X. Wang, A. Malekafzali, M. J. van Gemert, and J. S. Nelson, "Noninvasive imaging of in vivo blood flow velocity using optical Doppler tomography," Optics letters **22**, 1119–1121 (1997).

[51] H.-E. Albrecht, M. Borys, N. Damaschke, and C. Tropea, *Laser Doppler and phase Doppler measurement techniques* (Springer Verlag, Berlin, 2003).

[52] M. D. Stern, D. L. Lappe, P. D. Bowen, J. E. Chimosky, G. Holloway, H. Keiser, and R. Bowman, "Continuous measurement of tissue blood flow by laser-doppler spectroscopy," American Journal of Physiology-Heart and Circulatory Physiology **232**, H441–H448 (1977).

[53] R. Bonner and R. Nossal, "Model for laser Doppler measurements of blood flow in tissue," Applied optics **20**, 2097–2107 (1981).

[54] V. Rajan, B. Varghese, T. G. van Leeuwen, and W. Steenbergen, "Review of methodological developments in laser Doppler flowmetry," Lasers in Medical Science **24**, 269–283 (2009).

[55] P. Vaupel, F. Kallinowski, and P. Okunieff, "Blood flow, oxygen and nutrient supply, and metabolic microenvironment of human tumors: A review," Cancer Research **49**, 6449–6465 (1989).

[56] R. K. Jain, "Taming vessels to treat cancer," Scientific American **18**, 64–71 (2008).

[57] K. Pigott, S. Hill, D. Chaplin, and M. Saunders, "Microregional fluctuations in perfusion within human tumours detected using laser Doppler flowmetry," Radiotherapy and Oncology **40**, 45–50 (1996).

[58] I. Wang, S. Andersson-engels, G. Nilsson, K. Wardell, and K. Svanberg, "Superficial blood flow following photodynamic therapy of malignant non–melanoma skin tumours measured by laser doppler perfusion imaging," British Journal of Dermatology **136**, 184–189 (1997).

[59] J. M. Hammersley and D. C. Handscomb, *Monte Carlo Methods* (Wiley, 1964).

[60] D. P. Kroese, T. Taimre, and Z. I. Botev, *Handbook of Monte Carlo Methods* (Wiley, Hoboken, New Jersey, 2011).

[61] A. Tycho, T. M. Jørgensen, H. T. Yura, and P. E. Andersen, "Derivation of a Monte Carlo method for modeling heterodyne detection in optical coherence tomography systems," Applied Optics **41**, 6676–6691 (2002).

[62] F. M. Dickey, *Laser beam shaping: Theory and techniques* (CRC press, 2014).

[63] M. J. Kim, J. C. Dainty, A. T. Friberg, and A. J. Sant, "Experimental study of enhanced backscattering from one- and two-dimensional random rough surfaces," J. Opt. Soc. Am. A **7**, 569–577 (1990).

[64] A. A. Maradudin and E. R. Méndez, "Enhanced backscattering of light from weakly rough, random metal surfaces," Appl. Opt. **32**, 3335–3343 (1993).

[65] L. G. Henyey and J. L. Greenstein, "Diffuse radiation in the galaxy," The Astrophysical Journal **93**, 70–83 (1941).

[66] M. Hammer, A. N. Yaroslavsky, and D. Schweitzer, "A scattering phase function for blood with physiological haematocrit," Physics in Medicine and Biology **46**, N65 (2001).

[67] K. I. Iga and H. E. Li, *Vertical-cavity surface-emitting laser devices* (Berlin, Springer, 2003).

[68] K. J. Ebeling, *Integrated optoelectronics: waveguide optics, photonics, semiconductors* (Springer-Verlag, Berlin, 1993).

[69] L. A. Coldren, S. W. Corzine, and M. L. Mashanovitch, *Diode lasers and photonic integrated circuits* (John Wiley & Sons, Hoboken, New Jersey, 2012).

[70] T. Bosch, N. Servagent, and S. Donati, "Optical feedback interferometry for sensing application," Opt. Eng. **40**, 20–27 (2001).

[71] G. Giuliani, M. Norgia, S. Donati, and T. Bosch, "Laser diode self-mixing technique for sensing applications," Journal of Optics. A, Pure and Applied Optics **4**, S283–S294 (2002).

[72] L. Scalise, Y. Yu, G. Giuliani, G. Plantier, and T. Bosch, "Self-mixing laser diode velocimetry: Application to vibration and velocity measurement," IEEE Trans. Instrum. Meas. **53**, 223–232 (2004).

[73] Y. L. Lim, P. Dean, M. Nikolić, R. Kliese, S. P. Khanna, M. Lachab, A. Valavanis, D. Indjin, Z. Ikonić, P. Harrison, E. H. Linfield, A. G. Davies, S. J. Wilson, and A. D. Rakić, "Demonstration of a self-mixing displacement sensor based on terahertz quantum cascade lasers," Appl. Phys. Lett. **99**, 081108 (2011).

[74] R. Kliese, T. Taimre, A. A. A. Bakar, Y. L. Lim, K. Bertling, M. Nikolić, J. Perchoux, T. Bosch, and A. D. Rakić, "Solving self-mixing equations for arbitrary feedback levels: a concise algorithm," Applied Optics **53**, 3723–3736 (2014).

[75] G. A. Acket, D. Lenstra, A. J. Den Boef, and B. H. Verbeek, "The influence of feedback intensity on longitudinal mode properties and optical noise in index-guided semiconductor lasers," Quantum Electronics, IEEE Journal of **20**, 1163–1169 (1984).

[76] P. Spencer, P. Rees, and I. Pierce, "Theoretical analysis," in "Unlocking Dynamical Diversity: Optical Feedback Effects on Semiconductor Lasers," , D. M. Kane and K. A. Shore, eds. (John Wiley & Sons, Chichester, 2005), chap. 2, pp. 23–54.

[77] R. Juškaitis, N. Rea, and T. Wilson, "Semiconductor laser confocal microscopy," Applied Optics **33**, 578–584 (1994).

[78] C. Zakian, M. Dickinson, and T. King, "Particle sizing and flow measurement using self-mixing interferometry with a laser diode," J. Opt. A: Pure Appl. Opt. **7**, S445 (2005).

[79] M. Nikolić, D. P. Jovanović, Y. L. Lim, K. Bertling, T. Taimre, and A. D. Rakić, "Approach to frequency estimation in self-mixing interferometry: multiple signal classification," Appl. Opt. **52**, 3345–3350 (2013).

[80] M. Norgia, A. Pesatori, and L. Rovati, "Self-mixing laser Doppler spectra of extracorporeal blood flow: A theoretical and experimental study," IEEE Sens. J. **12**, 552–557 (2012).

[81] Y. L. Lim, R. Kliese, K. Bertling, K. Tanimizu, P. Jacobs, and A. D. Rakic, "Self-mixing flow sensor using a monolithic VCSEL array with parallel readout," Optics express **18**, 11720–11727 (2010).

[82] S. Shinohara, A. Mochizuki, H. Yoshida, and M. Sumi, "Laser Doppler velocimeter using the self-mixing effect of a semiconductor laser diode," Appl. Opt. **25**, 1417–1419 (1986).

[83] Y. L. Lim, M. Nikolić, K. Bertling, R. Kliese, and A. D. Rakić, "Self-mixing imaging sensor using a monolithic VCSEL array with parallel readout," Opt. Express **17**, 5517–5525 (2009).

[84] A. D. Rakić, T. Taimre, K. Bertling, Y. L. Lim, P. Dean, D. Indjin, Z. Ikonić, P. Harrison, A. Valavanis, S. P. Khanna, M. Lachab, S. J. Wilson, E. H. Linfield, and A. G. Davies, "Swept-frequency feedback interferometry using terahertz frequency QCLs: A method for imaging and materials analysis," Opt. Express **21**, 22194–22205 (2013).

[85] B. W. Pogue and M. S. Patterson, "Review of tissue simulating phantoms for optical spectroscopy, imaging and dosimetry," Journal of Biomedical Optics **11**, 041102–041102 (2006).

[86] S. J. Madsen, M. S. Patterson, and B. C. Wilson, "The use of India ink as an optical absorber in tissue-simulating phantoms," Physics in Medicine and Biology **37**, 985 (1992).

[87] T. L. Troy and S. N. Thennadil, "Optical properties of human skin in the near infrared wavelength range of 1000 to 2200 nm," Journal of Biomedical Optics **6**, 167–176 (2001).

[88] A. Bashkatov, E. Genina, V. Kochubey, and V. Tuchin, "Optical properties of human skin, subcutaneous and mucous tissues in the wavelength range from 400 to 2000 nm," Journal of Physics D: Applied Physics **38**, 2543 (2005).

[89] S. T. Flock, S. L. Jacques, B. C. Wilson, W. M. Star, and M. J. van Gemert, "Optical properties of intralipid: A phantom medium for light propagation studies," Lasers in Surgery and Medicine **12**, 510–519 (1992).

[90] Y. Yeh and H. Z. Cummins, "Localized fluid flow measurements with an he-ne laser spectrometer," Appl. Phys. Lett. **4**, 176–178 (1964).

[91] J. W. Foreman, E. W. George, and R. D. Lewis, "Measurement of localized flow velocities in gases with a laser doppler flowmeter," Appl. Phys. Lett. **7**, 77–78 (1965).

[92] J. W. Foreman, E. W. George, J. L. Jetton, R. D. Lewis, J. R. Thornton, and H. J. Watson, "8C2-fluid flow measurements with a laser Doppler velocimeter," IEEE J. Quant. Electron. **2**, 260–266 (1966).

[93] A. Shepherd and G. Riedel, “Continuous measurement of intestinal mucosal blood flow by laser-Doppler velocimetry,” American Journal of Physiology-Gastrointestinal and Liver Physiology **242**, G668–G672 (1982).

[94] R. Adrian and C. Yao, “Power spectra of fluid velocities measured by laser Doppler velocimetry,” Experiments in Fluids **5**, 17–28 (1986).

[95] J. M. Soto-Crespo and M. Nieto-Vesperinas, “Electromagnetic scattering from very rough random surfaces and deep reflection gratings,” J. Opt. Soc. Am. A **6**, 367–384 (1989).

[96] V. V. Tuchin, *Handbook of optical biomedical diagnostics* (SPIE Press, 2002).

[97] F. De Mul, M. Koelink, A. Weijers, J. Greve, J. Aarnoudse, R. Graaff, and A. Dassel, “Self-mixing laser-Doppler velocimetry of liquid flow and of blood perfusion in tissue,” Applied Optics **31**, 5844–5851 (1992).

[98] C. Zakian and M. Dickinson, “Laser Doppler imaging through tissues phantoms by using self-mixing interferometry with a laser diode,” Opt. Lett. **32**, 2798–2800 (2007).

[99] R. Kliese and A. D. Rakić, “Spectral broadening caused by dynamic speckle in self-mixing velocimetry sensors,” Opt. Express **20**, 18757–18771 (2012).

[100] J. W. Goodman, “Statistical properties of laser speckle patterns,” in “Laser Speckle and Related Phenomena,” , J. C. Dainty, ed. (Springer-Verlag, 1975), chap. 2, pp. 8–75.

[101] S. Donati, *Electro-optical instrumentation: sensing and measuring with lasers* (Prentice Hall, 2004).

[102] R. Atashkhooei, S. Royo, and F. J. Azcona, “Dealing with speckle effects in self-mixing interferometry measurements,” IEEE Sensors J. **13**, 1641–1647 (2013).

[103] P. A. Porta, D. P. Curtin, and J. G. McInerney, “Laser Doppler velocimetry by optical self-mixing in vertical-cavity surface-emitting lasers,” IEEE Photon. Technol. Lett. **14**, 1719–1721 (2002).

[104] M. Nikolić, Y. L. Lim, R. Kliese, T. Bosch, and A. D. Rakić, “Harmonic levels in self-mixing interferometry,” in “Proceedings of COMMAD 2010,” (2010).

[105] L. Lu, J. Yang, J. Dai, K. Zhang, L. Zhai, and B. Yu, "Effect of polarization properties on Doppler velocimetry with vertical-cavity surface-emitting lasers," Optik **123**, 329–332 (2012).

[106] B. Saleh and T. MC, "Fundamentals of photonics," John Wiley and Sons (2007).

[107] A. Lomas, J. Leonardi-Bee, and F. Bath-Hextall, "A systematic review of worldwide incidence of nonmelanoma skin cancer," British Journal of Dermatology **166**, 1069–1080 (2012).

[108] D. E. Godar, "Worldwide increasing incidences of cutaneous malignant melanoma," Journal of skin cancer **2011** (2011).

[109] P. Vaupel, "Tumor microenvironmental physiology and its implications for radiation oncology," in "Seminars in Radiation Oncology," , vol. 14 (Elsevier, 2004), vol. 14, pp. 198–206.

[110] I. Fredriksson, M. Larsson, and T. Strömberg, "Optical microcirculatory skin model: assessed by Monte Carlo simulations paired with in vivo laser Doppler flowmetry," Journal of Biomedical Optics **13**, 014015–014015 (2008).

[111] A. Gerger, R. Hofmann-Wellenhof, U. Langsenlehner, E. Richtig, S. Koller, W. Weger, V. Ahlgrimm-Siess, M. Horn, H. Samonigg, and J. Smolle, "In vivo confocal laser scanning microscopy of melanocytic skin tumours: diagnostic applicability using unselected tumour images," Br. J. Dermatol. **158**, 329–333 (2008).

[112] T. Wilson, "Confocal microscopy," Academic Press: London **426**, 1–64 (1990).

[113] M. Stern, "In vivo evaluation of microcirculation by coherent light scattering," Nature **254**, 56–58 (1975).

[114] P. B. Jones, H. K. Shin, D. A. Boas, B. T. Hyman, M. A. Moskowitz, C. Ayata, and A. K. Dunn, "Simultaneous multispectral reflectance imaging and laser speckle flowmetry of cerebral blood flow and oxygen metabolism in focal cerebral ischemia," J. Biomed. Opt. **13**, 044007–044007 (2008).

[115] S. Shanthi and M. Singh, "Laser reflectance imaging of human organs and comparison with perfusion images," Med. Biol. Eng. Comput. **35**, 253–258 (1997).

[116] S. Donati, D. Rossi, and M. Norgia, "Single channel self-mixing interferometer measures simultaneously displacement and tilt and yaw angles of a reflective target," IEEE J. Quant. Electron. **51**, 1–8 (2015).

[117] A. Bearden, M. P. O'Neill, L. C. Osborne, and T. L. Wong, "Imaging and vibrational analysis with laser-feedback interferometry," Optics Letters **18**, 238–240 (1993).

[118] C.-H. Lu, J. Wang, and K.-L. Deng, "Imaging and profiling surface microstructures with noninterferometric confocal laser feedback," Applied Physics Letters **66**, 2022–2024 (1995).

[119] Y. L. Lim, K. Bertling, P. Rio, J. Tucker, and A. Rakic, "Displacement and distance measurement using the change in junction voltage across a laser diode due to the self-mixing effect," in "Microelectronics, MEMS, and Nanotechnology," (International Society for Optics and Photonics, 2005), pp. 60381O–60381O.

[120] A. Mowla, M. Nikolić, T. Taimre, J. R. Tucker, Y. L. Lim, K. Bertling, and A. D. Rakić, "Effect of the optical system on the Doppler spectrum in laser-feedback interferometry," Applied Optics **54**, 18–26 (2015).

[121] L. Campagnolo, M. Nikolić, J. Perchoux, Y. L. Lim, K. Bertling, K. Loubière, L. Prat, A. D. Rakić, and T. Bosch, "Flow profile measurement in microchannel using the optical feedback interferometry sensing technique," Microfluid. Nanofluid. **14**, 113–119 (2013).

[122] R. S. Matharu, J. Perchoux, R. Kliese, Y. L. Lim, and A. D. Rakić, "Maintaining maximum signal-to-noise ratio in uncooled vertical-cavity surface-emitting laser-based self-mixing sensors," Optics Letters **36**, 3690–3692 (2011).

[123] R. Bonner, R. Nossal, S. Havlin, and G. Weiss, "Model for photon migration in turbid biological media," J. Opt. Soc. Am. A **4**, 423–432 (1987).

[124] M. Norgia, A. Pesatori, and S. Donati, "Compact laser-diode instrument for flow measurement," IEEE Trans. Instrum. Meas. **65**, 1478–1483 (2016).

[125] K. Bertling, T. Taimre, G. Agnew, Y. L. Lim, P. Dean, D. Indjin, S. Höfling, R. Weih, M. Kamp, M. von Edlinger *et al.*, "Simple electrical modulation scheme for laser feedback imaging," IEEE Sensors Journal **16**, 1937–1942 (2016).

[126] M. Wienold, T. Hagelschuer, N. Rothbart, L. Schrottke, K. Biermann, H. Grahn, and H.-W. Hübers, "Real-time terahertz imaging through self-mixing in a quantum-cascade laser," Appl. Phys. Lett. **109**, 011102 (2016).

[127] T. Diepgen and V. Mahler, "The epidemiology of skin cancer," British Journal of Dermatology **146**, 1–6 (2002).

[128] H. P. Soyer, D. Rigel, and E. M. Wurm, *Dermatology* (London: Elsevier, 2012), chap. Actinic Keratosis, Basal Cell Carcinoma and Squamous Cell Carcinoma, pp. 1773–1794, 3rd ed.

[129] A. Baldi, P. Pasquali, and E. P. Spugnini, *Skin Cancer: A Practical Approach* (Humana Press, Springer, 2014).

[130] H. W. Walling, S. W. Fosko, P. A. Geraminejad, D. C. Whitaker, and C. J. Arpey, "Aggressive basal cell carcinoma: presentation, pathogenesis, and management," Cancer and Metastasis Reviews **23**, 389–402 (2004).

[131] R. R. Anderson and J. A. Parrish, "The optics of human skin," Journal of Investigative Dermatology **77**, 13–19 (1981).

[132] G. Zonios, L. T. Perelman, V. Backman, R. Manoharan, M. Fitzmaurice, J. Van Dam, and M. S. Feld, "Diffuse reflectance spectroscopy of human adenomatous colon polyps in vivo," Applied Optics **38**, 6628–6637 (1999).

[133] G. Zonios, J. Bykowski, and N. Kollias, "Skin melanin, hemoglobin, and light scattering properties can be quantitatively assessed in vivo using diffuse reflectance spectroscopy," Journal of Investigative Dermatology **117**, 1452–1457 (2001).

[134] J. Saravanamuthu, A. Seifalian, W. Reid, and A. Maclean, "A new technique to map vulva microcirculation using laser doppler perfusion imager," International Journal of Gynecological Cancer **13**, 812–818 (2003).

[135] A. N. Yaroslavsky, J. Barbosa, V. Neel, C. DiMarzio, and R. R. Anderson, "Combining multispectral polarized light imaging and confocal microscopy for localization of nonmelanoma skin cancer," Journal of Biomedical Optics **10**, 014011–0140116 (2005).

[136] J. Perchoux, A. Quotb, R. Atashkhooei, F. J. Azcona, E. E. Ramírez-Miquet, O. Bernal, A. Jha, A. Luna-Arriaga, C. Yanez, J. Caum *et al.*, "Current developments on optical feedback interferometry as an all-optical sensor for biomedical applications," Sensors **16**, 694 (2016).

[137] A. Mowla, M. Nikolic, Y. L. Lim, K. Bertling, A. D. Rakic, and T. Taimre, "Effect of the optical numerical aperture on the doppler spectrum in laser Doppler velocimetry," in "Optoelectronic and Microelectronic Materials & Devices (COMMAD), 2014 Conference on," (IEEE, 2014), pp. 72–74.

[138] J. White, “Reflecting on confocal microscopy: A personal perspective,” Confocal Microscopy: Methods and Protocols pp. 1–7 (2014).

[139] M. Wang and G. Lai, “Self-mixing microscopic interferometer for the measurement of microprofile,” Optics Communications **238**, 237–244 (2004).

[140] Y. Tan, W. Wang, C. Xu, and S. Zhang, “Laser confocal feedback tomography and nano-step height measurement,” Scientific reports **3** (2013).

[141] A. Mowla, T. Taimre, Y. L. Lim, K. Bertling, S. J. Wilson, T. W. Prow, H. P. Soyer, and A. D. Rakić, “Diffuse reflectance imaging for non-melanoma skin cancer detection using laser feedback interferometry,” in “SPIE Photonics Europe,” (International Society for Optics and Photonics, 2016), pp. 98870T–98870T.

[142] R. Michalzik, *VCSELs: Fundamentals, technology and applications of vertical-cavity surface-emitting lasers*, vol. 166 (Springer, 2012).

[143] E. Figueiras, R. Oliveira, C. F. Lourenço, R. Campos, A. Humeau-Heurtier, R. M. Barbosa, J. Laranjinha, L. F. R. Ferreira, and F. F. de Mul, “Self-mixing microprobe for monitoring microvascular perfusion in rat brain,” Medical & biological engineering & computing **51**, 103–112 (2013).

[144] V. Tuchin, *Tissue Optics* (SPIE, 2007), second edition ed.

[145] D. P. Kroese, T. Taimre, and Z. I. Botev, *Handbook of monte carlo methods*, vol. 706 (John Wiley & Sons, 2013).

[146] G. M. Hale and M. R. Querry, “Optical constants of water in the 200-nm to 200-μm wavelength region,” Applied Optics **12**, 555–563 (1973).

[147] X. Feng, R. Patel, and A. N. Yaroslavsky, “Wavelength optimized cross-polarized wide-field imaging for noninvasive and rapid evaluation of dermal structures,” Journal of Biophotonics **8** (2015).

[148] S. L. Jacques, “Skin optics,” Oregon Medical Laser Center News **1998**, 1–9 (1998).

[149] A. Mowla, T. Taimre, Y. L. Lim, K. Bertling, S. J. Wilson, T. W. Prow, and A. D. Rakić, “A compact laser imaging system for concurrent reflectance confocal microscopy and laser Doppler flowmetry,” IEEE Photonics Journal (2016).

[150] R. Cubeddu, A. Pifferi, P. Taroni, A. Torricelli, and G. Valentini, “A solid tissue phantom for photon migration studies,” Physics in medicine and biology **42**, 1971 (1997).

[151] R. Marchesini, M. Brambilla, C. Clemente, M. Maniezzo, A. E. Sichirollo, A. Testori, D. R. Venturoli, and N. Cascinelli, "In vivo spectrophotometric evaluation of neoplastic and non-neoplastic skin pigmented lesions–i. reflectance measurements," Photochemistry and Photobiology **53**, 77–84 (1991).

[152] S. Tomatis, C. Bartoli, A. Bono, N. Cascinelli, C. Clemente, and R. Marchesini, "Spectrophotometric imaging of cutaneous pigmented lesions: discriminant analysis, optical properties and histological characteristics," Journal of Photochemistry and Photobiology B: Biology **42**, 32–39 (1998).

[153] G. Zonios and A. Dimou, "Modeling diffuse reflectance from semi-infinite turbid media: Application to the study of skin optical properties," Optics Express **14**, 8661–8674 (2006).

[154] G. Zonios, A. Dimou, I. Bassukas, D. Galaris, A. Tsolakidis, and E. Kaxiras, "Melanin absorption spectroscopy: New method for noninvasive skin investigation and melanoma detection," Journal of Biomedical Optics **13**, 014017–014017 (2008).

[155] G. Zonios, A. Dimou, M. Carrara, and R. Marchesini, "In vivo optical properties of melanocytic skin lesions: Common nevi, dysplastic nevi and malignant melanoma," Photochemistry and photobiology **86**, 236–240 (2010).

[156] A. Garcia-Uribe, E. B. Smith, J. Zou, M. Duvic, V. Prieto, and L. V. Wang, "In-vivo characterization of optical properties of pigmented skin lesions including melanoma using oblique incidence diffuse reflectance spectrometry," Journal of Biomedical Optics **16**, 020501–020501 (2011).

[157] A. Garcia-Uribe, J. Zou, M. Duvic, J. H. Cho-Vega, V. G. Prieto, and L. V. Wang, "In vivo diagnosis of melanoma and nonmelanoma skin cancer using oblique incidence diffuse reflectance spectrometry," Cancer Research **72**, 2738–2745 (2012).

[158] P. Jorgensen, N. P. Edgington, B. L. Schneider, I. Rupeš, M. Tyers, and B. Futcher, "The size of the nucleus increases as yeast cells grow," Molecular Biology of the Cell **18**, 3523–3532 (2007).

[159] D. Slater, S. Rice, R. Stewart, S. Melling, E. Hewer, and J. Smith, "Proposed sheffield quantitative criteria in cervical cytology to assist the grading of squamous cell dyskaryosis, as the british society for clinical cytology definitions require amendment," Cytopathology **16**, 179–192 (2005).

[160] A. J. Sober and J. M. Burstein, "Precursors to skin cancer," Cancer **75**, 645–650 (1995).

[161] R. Schwartz, T. Bridges, A. Butani, and A. Ehrlich, "Actinic keratosis: an occupational and environmental disorder," Journal of the European Academy of Dermatology and Venereology **22**, 606–615 (2008).

[162] J. Lacour, "Carcinogenesis of basal cell carcinomas: Genetics and molecular mechanisms," British Journal of Dermatology **146**, 17–19 (2002).

[163] D. P. Slaughter, H. W. Southwick, and W. Smejkal, "Field cancerization in oral stratified squamous epithelium. Clinical implications of multicentric origin," Cancer **6**, 963–968 (1953).

[164] S. Kanjilal, S. S. Strom, G. L. Clayman, R. S. Weber, A. K. El-Naggar, V. Kapur, K. K. Cummings, L. A. Hill, M. R. Spitz, M. L. Kripke *et al.*, "p53 mutations in nonmelanoma skin cancer of the head and neck: Molecular evidence for field cancerization," Cancer Research **55**, 3604–3609 (1995).

[165] P. Incel, M. Gurel, and A. Erdemir, "Vascular patterns of nonpigmented tumoral skin lesions: confocal perspectives," Skin Research and Technology **21**, 333–339 (2015).

[166] A. N. Yaroslavsky, V. Neel, and R. R. Anderson, "Demarcation of nonmelanoma skin cancer margins in thick excisions using multispectral polarized light imaging," Journal of Investigative Dermatology **121**, 259–266 (2003).

[167] R. Marks and C. Edwards, "The measurement of photodamage," British Journal of Dermatology **127**, 7–13 (1992).

[168] R. Weissleder, "A clearer vision for in vivo imaging," Nature Biotechnology **19**, 316–317 (2001).

[169] T. J. Farrell, M. S. Patterson, and B. Wilson, "A diffusion theory model of spatially resolved, steady-state diffuse reflectance for the noninvasive determination of tissue optical properties invivo," Medical Physics **19**, 879–888 (1992).

[170] J. R. Mourant, A. H. Hielscher, A. A. Eick, T. M. Johnson, and J. P. Freyer, "Evidence of intrinsic differences in the light scattering properties of tumorigenic and nontumorigenic cells," Cancer Cytopathology **84**, 366–374 (1998).

[171] N. Dögnitz and G. Wagnières, "Determination of tissue optical properties by steady-state spatial frequency-domain reflectometry," Lasers in Medical Science **13**, 55–65 (1998).

[172] R. Doornbos, R. Lang, M. Aalders, F. Cross, and H. Sterenborg, "The determination of in vivo human tissue optical properties and absolute chromophore concentrations using spatially resolved steady-state diffuse reflectance spectroscopy," Physics in Medicine and Biology **44**, 967 (1999).

[173] R. M. Woodward, B. E. Cole, V. P. Wallace, R. J. Pye, D. D. Arnone, E. H. Linfield, and M. Pepper, "Terahertz pulse imaging in reflection geometry of human skin cancer and skin tissue," Physics in Medicine and Biology **47**, 3853 (2002).

[174] B. Guo, Y. Wang, C. Peng, H. Zhang, G. Luo, H. Le, C. Gmachl, D. Sivco, M. Peabody, and A. Y. Cho, "Laser-based mid-infrared reflectance imaging of biological tissues," Optics Express **12**, 208–219 (2004).

[175] R. Anderson and J. Parrish, "Optical properties of human skin," in "The Science of Photomedicine," (Springer, 1982), pp. 147–194.

[176] I. Nishidate, Y. Aizu, and H. Mishina, "Estimation of melanin and hemoglobin in skin tissue using multiple regression analysis aided by monte carlo simulation," Journal of Biomedical Optics **9**, 700–710 (2004).

[177] J. Frank, *Electron tomography* (Springer, Dordrecht, 2008).

[178] J. Hsieh, *Computed tomography: principles, design, artifacts, and recent advances* (SPIE Bellingham, Washington, USA, 2009).

[179] D. A. Boas, D. H. Brooks, E. L. Miller, C. A. DiMarzio, M. Kilmer, R. J. Gaudette, and Q. Zhang, "Imaging the body with diffuse optical tomography," IEEE Signal Processing Magazine **18**, 57–75 (2001).

[180] A. Gibson, J. Hebden, and S. R. Arridge, "Recent advances in diffuse optical imaging," Physics in medicine and biology **50**, R1 (2005).

[181] T. Durduran, R. Choe, W. Baker, and A. Yodh, "Diffuse optics for tissue monitoring and tomography," Reports on Progress in Physics **73**, 076701 (2010).

[182] Y. Zhao, Z. Chen, C. Saxer, S. Xiang, J. F. de Boer, and J. S. Nelson, "Phase-resolved optical coherence tomography and optical doppler tomography for imaging

blood flow in human skin with fast scanning speed and high velocity sensitivity," Optics Letters **25**, 114–116 (2000).

[183] E. Lacot, R. Day, and F. Stoeckel, "Laser optical feedback tomography," Optics letters **24**, 744–746 (1999).

[184] C. Xu, Y. Tan, S. Zhang, and S. Zhao, "The structure measurement of micro-electromechanical system devices by the optical feedback tomography technology," Applied Physics Letters **102**, 221902 (2013).

[185] T. Bosch, N. Servagent, R. Chellali, and M. Lescure, "Three-dimensional object construction using a self-mixing type scanning laser range finder," IEEE Transactions on Instrumentation and Measurement **47**, 1326–1329 (1998).

[186] E. Gagnon and J.-F. Rivest, "Laser range imaging using the self-mixing effect in a laser diode," IEEE Transactions on Instrumentation and measurement **48**, 693–699 (1999).

[187] J. Keeley, P. Dean, A. Valavanis, K. Bertling, Y. Lim, R. Alhathlool, T. Taimre, L. Li, D. Indjin, A. Rakić *et al.*, "Three-dimensional terahertz imaging using swept-frequency feedback interferometry with a quantum cascade laser," Optics letters **40**, 994–997 (2015).

[188] O. Hugon, I. Paun, C. Ricard, B. Van der Sanden, E. Lacot, O. Jacquin, and A. Witomski, "Cell imaging by coherent backscattering microscopy using frequency-shifted optical feedback in a microchip laser," Ultramicroscopy **108**, 523–528 (2008).

[189] O. Hugon, F. Joud, E. Lacot, O. Jacquin, and H. G. de Chatellus, "Coherent microscopy by laser optical feedback imaging (lofi) technique," Ultramicroscopy **111**, 1557–1563 (2011).

[190] D. Zink, A. H. Fischer, and J. A. Nickerson, "Nuclear structure in cancer cells," Nature Reviews Cancer **4**, 677–687 (2004).

[191] F. Ayers, A. Grant, D. Kuo, D. J. Cuccia, and A. J. Durkin, "Fabrication and characterization of silicone-based tissue phantoms with tunable optical properties in the visible and near infrared domain," in "Biomedical Optics (BiOS) 2008," (International Society for Optics and Photonics, 2008), pp. 687007–687007.

[192] J. R. Tucker, Y. L. Lim, A. V. Zvyagin, and A. D. Rakic, "A massively parallel imaging system based on the self-mixing effect in a vertical-cavity surface-emitting laser array," in "2006 Northern Optics," (IEEE, 2006), pp. 41–45.

[193] J. R. Tucker, J. L. Baque, Y. L. Lim, A. V. Zvyagin, and A. D. Rakić, "Parallel self-mixing imaging system based on an array of vertical-cavity surface-emitting lasers," Applied Optics **46**, 6237–6246 (2007).

[194] M. Maeda, C. Chang-Hasnain, A. Von Lehmen, H. Izadpanah, C. Lin, M. Iqbal, L. Florez, and J. Harbison, "Multigigabit/s operations of 16-wavelength vertical-cavity surface-emitting laser array," IEEE Photon. Tech. Lett. **3**, 863–865 (1991).

[195] T. C. Banwell, A. C. Von Lehmen, and R. R. Cordell, "Vcse laser transmitters for parallel data links," IEEE J. Quantum Electron. **29**, 635–644 (1993).

[196] F. Tsai, C. J. O'Brien, N. S. Petrovic, and A. D. Rakić, "Analysis of hexagonal array geometry for free-space optical interconnects with improved signal-to-noise ratio," Applied Optics **46**, 2434–2442 (2007).

[197] E. K. Lau, X. Zhao, H.-K. Sung, D. Parekh, C. Chang-Hasnain, and M. C. Wu, "Strong optical injection-locked semiconductor lasers demonstrating 100-GHz resonance frequencies and 80-GHz intrinsic bandwidths," Opt. Express **16**, 6609–6618 (2008).

[198] W. Yang, P. Guo, D. Parekh, and C. J. Chang-Hasnain, "Reflection-mode optical injection locking," Opt. Express **18**, 20887–20893 (2010).

[199] R. Lang, "Injection locking properties of a semiconductor laser," IEEE J. Quantum Electron. **QE-18**, 976 – 83 (1982).

[200] G. Heise, "Crosstalk investigation of laser-diode pairs," IEEE Photon. Tech. Lett. **2**, 97–99 (1990).

[201] S. Nakagawa, S.-Y. Hu, D. Louderback, and L. A. Coldren, "RF crosstalk in multiple-wavelength vertical-cavity surface-emitting laser arrays," IEEE Photon. Tech. Lett. **12**, 612–614 (2000).

[202] M. Châteauneuf, A. G. Kirk, D. V. Plant, T. Yamamoto, and J. D. Ahearn, "512-channel vertical-cavity surface-emitting laser based free-space optical link," Appl. Opt. **41**, 5552–5561 (2002).

[203] K. Sato and M. Murakami, “Experimental investigation of thermal crosstalk in a distributed feedback laser array,” IEEE Photon. Tech. Lett. **3**, 501–503 (1991).

[204] M. Osinski and W. Nakwaski, “Thermal analysis of closely-packed two-dimensional etched-well surface-emitting laser arrays,” IEEE J. Sel. Top. Quant. Electron. **1**, 681–696 (1995).

[205] P. Dean, Y. L. Lim, A. Valavanis, R. Kliese, M. Nikolić, S. P. Khanna, M. Lachab, D. Indjin, Z. Ikonić, P. Harrison, A. D. Rakić, E. H. Linfield, and A. G. Davies, “Terahertz imaging through self-mixing in a quantum cascade laser,” Opt. Lett. **36**, 2587–2589 (2011).

[206] K. Rochford and A. Rose, “Simultaneous laser-diode emission and detection for fiber-optic sensor applications,” Opt. Lett. **20**, 2105 – 2107 (1995).

[207] C. Chen, P. O. Leisher, A. A. Allerman, K. M. Geib, and K. D. Choquette, “Temperature analysis of threshold current in infrared vertical-cavity surface-emitting lasers,” IEEE J. Quantum Electron. **42**, 1078–1083 (2006).

[208] G. Hasnain, K. Tai, L. Yang, Y. Wang, R. Fischer, J. D. Wynn, B. Weir, N. Dutta, and A. Cho, “Performance of gain-guided surface emitting lasers with semiconductor distributed Bragg reflectors,” IEEE J. Quantum Electron. **27**, 1377–1385 (1991).

[209] J. Ophir, I. Cespedes, H. Ponnekanti, Y. Yazdi, and X. Li, “Elastography: A quantitative method for imaging the elasticity of biological tissues,” Ultrasonic Imaging **13**, 111–134 (1991).

[210] J. Bercoff, M. Tanter, and M. Fink, “Supersonic shear imaging: a new technique for soft tissue elasticity mapping,” IEEE transactions on ultrasonics, ferroelectrics, and frequency control **51**, 396–409 (2004).

[211] A. Manduca, T. E. Oliphant, M. Dresner, J. Mahowald, S. Kruse, E. Amromin, J. P. Felmlee, J. F. Greenleaf, and R. L. Ehman, “Magnetic resonance elastography: Non-invasive mapping of tissue elasticity,” Medical Image Analysis **5**, 237–254 (2001).

[212] J. M. Schmitt, “OCT elastography: imaging microscopic deformation and strain of tissue,” Optics Express **3**, 199–211 (1998).

[213] K. Bertling, J. Perchoux, T. Taimre, R. Malkin, D. Robert, A. D. Rakić, and T. Bosch, "Imaging of acoustic fields using optical feedback interferometry," Optics Express **22**, 30346–30356 (2014).